



Prototyping and Measurement of a metamaterial for noise reduction

Master's Thesis Nr. 0069

Scientific Thesis for Acquiring the
Master of Science Degree
at the Department of Mechanical Engineering
of the Technical University of Munich.

Thesis Advisor Laboratory for Production Development and Lightweight Design
Prof. Dr. Markus Zimmermann

Supervisors Laboratory for Production Development and Lightweight Design
Duo Xu, Dr. Anand Vazhapillil Sureshbabu

Submitted by Diana Grill
Moosachweg 11, 85764 Oberschleißheim
Matriculation number: 03638298
dianagrill@t-online.de

Submitted on 26.04.2020

Declaration

I assure that I have written this work autonomously and with the aid of no other than the sources and additives indicated.

Place

Date

Signature

Project Definition(1/2)

Initial Situation

The acoustic behavior of products is perceived directly by the customers and thus influences their product satisfaction and purchase decision. Besides rising customer expectations of acoustically optimized products, restrictive statutory requirements in terms of permissible noise emission contribute to a rising importance of the noise reduction as a fundamental aspect in the product development. There are various measures that can be taken to optimize the audible product characteristics. For example, sound generation at the source as well as sound transmission and radiation can be reduced by decreasing sound radiating surfaces, increasing the stiffness or lining surfaces with absorption material. However, some approaches to optimize the sound radiation of products are accompanied by an increase in mass. Due to the fact that some conventional solutions have difficulties to satisfactorily meet the described requirements, which are a good acoustic behavior and lightweight properties, acoustic metamaterials may provide a promising solution to this challenge.

Previously, the parameters that influence the acoustic properties of acoustic metamaterials have not been extensively researched. According to the current state of the art, there is no method for conception and manufacturing an acoustic metamaterial. This subject shall be taken up in the present work by identifying influencing variables on the sound reduction by a parameter variation.

Goals

In the present work the effectiveness of acoustic metamaterials in noise reduction is to be investigated. Concepts of different geometries are to be designed and are to be manufactured by means of an additive manufacturing process. According to the current state of the art, simulations of acoustic metamaterials can not provide comprehensive and exact results. Therefore, experimental studies with the impedance tube and sound level meter will be carried out to examine the potential of the prototypes in sound absorption. Based on the experimental results, proposals for improving the properties of the demonstrators regarding minimal weight, maximal attenuation or broadband attenuation of the prototypes are to be suggested.

Project Definition(2/2)

Contents of this Thesis

- Introduction
 - Motivation
 - Goals of the investigation
 - Organization of the investigation
- State of science
 - The history and development of acoustic metamaterials
 - The concept of acoustic metamaterials
 - Applications of acoustic metamaterials
 - Additive manufacturing technologies
 - Experimental measurement
- Concept development and prototyping of metamaterial structures
 - New concept of acoustic metamaterials
 - CAD modeling
 - Parameter variation of the metamaterial structures
 - Prototyping of acoustic metamaterials
- Experimental measurement of the panels
 - Description of the test set-up
 - Analysis of the measurement results
 - Optimization of the panels
- Experimental measurement of the acoustic enclosures
 - Description of the test set-up
 - Analysis of the measurement results
- Summary and outlook

An accurate elaboration, a comprehensible and complete documentation of all steps and applied methods are of particular importance.

The work remains a property of the Laboratory for Product Development and Lightweight Design.

Project Note

Master's Thesis

Nr. 0069

Supervisors

Duo Xu, Dr. Anand Vazhapilli Sureshbabu

Time period

26.07.2019 - 26.04.2020

My supervisor Mr. Duo Xu mentored me during the compilation of the work and gave continuous input. We exchanged and coordinated approaches and results weekly.

I consent to the laboratory and its staff members using content from my thesis for publications, project reports, lectures, seminars, dissertations and postdoctoral lecture qualifications

Signature of student

Signature of supervisors

At this point I would like to thank the Chair of Vibroacoustics of Vehicles and Machines of the Faculty of Mechanical Engineering led by Prof. Dr. Steffen Marburg of the Technical University of Munich for the provision of the acoustic impedance tube. In particular, I would like to thank the research associates Martin Eser, Felix Kronowetter, Marcus Maeder and Simone Preuss for their support in carrying out measurements.

Furthermore, I would like to thank the Institute for Micro Technology and Medical Technology led by Prof. Dr. Tim Lüth of the Department of Mechanical Engineering at the Technical University of Munich for their support. I would like to thank Yilun Sun for his help in creating models with the Matlab toolbox SG-Library®.

Contents

1 Introduction	3
1.1 Motivation.....	3
1.2 Goals of this thesis	4
1.3 Structure of this thesis	4
2 State of Science	6
2.1 The history and development of acoustic metamaterials	6
2.2 The concept of acoustic metamaterials.....	8
2.2.1 Prototypes of metamaterials with interference-based stop bands	9
2.2.2 Prototypes of metamaterials with resonance-based stop bands	11
2.2.3 Prototypes of metamaterials combining interference-based and resonance-based stop bands.....	12
2.3 Categories of acoustic metamaterials	12
2.4 Additive manufacturing technologies.....	14
2.4.1 Working steps of additive manufacturing	15
2.4.2 Categorization of additive manufacturing processes	16
2.4.3 Selection of the additive manufacturing technology	18
2.4.4 Stereolithography	19
2.5 Experimental measurement	21
2.5.1 Measured physical quantities	21
2.5.2 Set-up	23
3 Prototyping of metamaterial structures	32
3.1 Concept development of acoustic metamaterials	32
3.2 CAD modeling	33
3.2.1 CAD modeling of the panel	34
3.2.2 CAD modeling of acoustic enclosure	36
3.3 Parameter variation of metamaterial structures.....	36
3.3.1 Parameter variation of the panels	37
3.3.2 Parameter variation of the acoustic enclosures.....	42
3.4 Prototyping of acoustic metamaterials	42
3.4.1 3D printer Prusa SL1®	42
3.4.2 Practical aspects of the manufacturing process	48

4 Experimental measurement of the panels	51
4.1 Determination of the sound absorption coefficient of panel designs in the acoustic impedance tube according to DIN EN ISO 10534-2	51
4.1.1 Structure of the acoustic impedance tube	51
4.1.2 Working steps	52
4.2 Analysis of the measurement data	53
4.2.1 Base panel and reference measurements	53
4.2.2 Measurement data of all prototypes.....	55
4.2.3 Cavity geometry	55
4.2.4 Resonant structures.....	68
4.2.5 Material.....	76
4.3 Optimal design of the panels.....	78
4.4 Limits of the measurement technology.....	79
5 Design and measurement of acoustic enclosures.....	80
5.1 The design of the acoustic enclosures	80
5.2 Measurement setup for determining the sound pressure level L_p	80
5.3 Analysis of the measurement data	82
5.3.1 Limits of the measurement technology	85
6 Summary and outlook	86
6.1 Summary of results	86
6.2 Outlook.....	86
6.2.1 Statistical evaluation based on a representative sample size and composition ..	86
6.2.2 Analysis of the influence of the resonant structures on noise reduction	87
6.2.3 Analysis of the influence of the material properties on sound absorption	88
7 References	89
8 List of Figures	93
Appendix	A

1 Introduction

1.1 Motivation

The acoustic behavior of products is an important design criterion, as it is noticed directly by the customers. (Claeys, Deckers, Pluymers, & Desmet, 2016) Due to increasing customer requests for quiet products and the growing awareness of the health impact of noise as well as more restrictive regulations of the exposure of noise, a high demand on products with high sound-reducing properties emerges. (Gupfinger, Greisberger, Hasenhuettl, & Schweighofer, n.d.) (Claeys et al., 2016) In addition, the current trend in materials engineering and sciences is moving towards lightweight constructions. (Van Belle, Claeys, Deckers, Pluymers, & Desmet, 2016) Therefore, noise reduction without adversely affecting the weight of the products is of great importance in product development. (Bruenglinghaus, 2013)

Currently, audible product characteristics can be influenced by various approaches. These are for example, the reduction of the sound generation at the source or the hindrance of the sound transmission and radiation. Concrete measures are the reduction of sound radiating surfaces, the increase of the stiffness or the lining of surfaces with absorption material. (Haffke, n.d.) Considering the fact that the noise properties of a material are partially determined by its mass, some of these conventional solutions can no longer satisfactorily meet the requirements of low noise emission and weight. Since acoustic metamaterials combine lightweight properties with high noise attenuation performance in defined frequency ranges, this technology has come to the fore as a possible solution to meet current requirements. (Van Belle et al., 2016)

Despite the intense research and the substantial global financial investments, the practical deployment of metamaterials has not yet been put into practice. Reasons for this are that the research on metamaterials began just a few decades ago and many related challenges like the still insufficiently researched use of metamaterials in various fields of application as well as the development of high-throughput, cost-effective fabrication and design processes are not yet solved. (Tretyakov, Urbas, & Zheludev, 2017) The industrial integration of metamaterial assumes that one finds solutions for challenges like the design, production and integration of the metamaterial technology in products and processes by a holistic approach of the entire value chain. Cost-efficient manufacturing processes and design tools for metamaterials must be developed and assessed. Furthermore, the interaction effects in industrial environments on the performance of metamaterial components must be investigated and the metamaterial performance on dedicated industrial use cases must be demonstrated. (Van Belle et al., 2016) This means that different manufacturing processes with their respective advantages and disadvantages must be analyzed. All steps from product idea to product completion must be economically and technically investigated and described to define processes for successful modeling and industrial manufacturing. The most important aspect of the practical use of acoustic metamaterials is the comprehensive understanding of the functionality of the meta-material. The extent to which decisive geometric parameters determine the effectiveness of metamaterials must be researched in order to design products with defined properties.

1.2 Goals of this thesis

The focus of the present work is on the investigation of the influencing parameters of acoustic metamaterials on noise reduction and the design of an acoustic metamaterial. Different types of panels are to be designed and manufactured by means of additive manufacturing. By measuring the respective sound absorptions with an acoustic impedance tube, the influence of different parameters on the sound-reducing effect of acoustic metamaterials is to be determined. Based on the results of the experimental investigation proposals for improving the properties of the panels are to be derived, whereby the focus is on minimum weight, maximum attenuation and broadband attenuation. On the basis of these measurement and optimization results conceptions of acoustic enclosures to cover a noise source are to be developed and are to be measured with a sound level meter. In the present work, only experimental investigations of the prototypes will be performed, since according to the current state of the art, simulations of acoustic metamaterials do not provide comprehensive and accurate results. The purpose of this thesis is to experimentally determine the degree of influence of various design parameters on the noise reduction of resonant based acoustic metamaterials.

1.3 Structure of this thesis

The paper is structured as follows:

Chap. 2 presents the history and applications of acoustic metamaterials. Furthermore, the state of science of the concept of acoustic metamaterials is introduced through literature research. Moreover, an overview of different additive manufacturing technologies and measurement techniques of acoustic metamaterials are explained.

Chap. 3 describes the concept development, CAD modeling and prototyping of different variations of acoustic metamaterials. The CAD modeling of the prototypes and their production by means of additive manufacturing is discussed.

Chap. 4 outlines the measurement set-up for determining the sound reduction by the panels. This chapter also presents the analysis of the measurement data and the derived optimization proposals.

Chap. 5 details the procedure of experimental measurement of the acoustic enclosures as well as the test set-up. The analysis of the collected measurement data including findings about influences of variated parameters on the noise reduction are given.

Chap. 6 presents a summary of the main conclusions and proposals for further investigations.

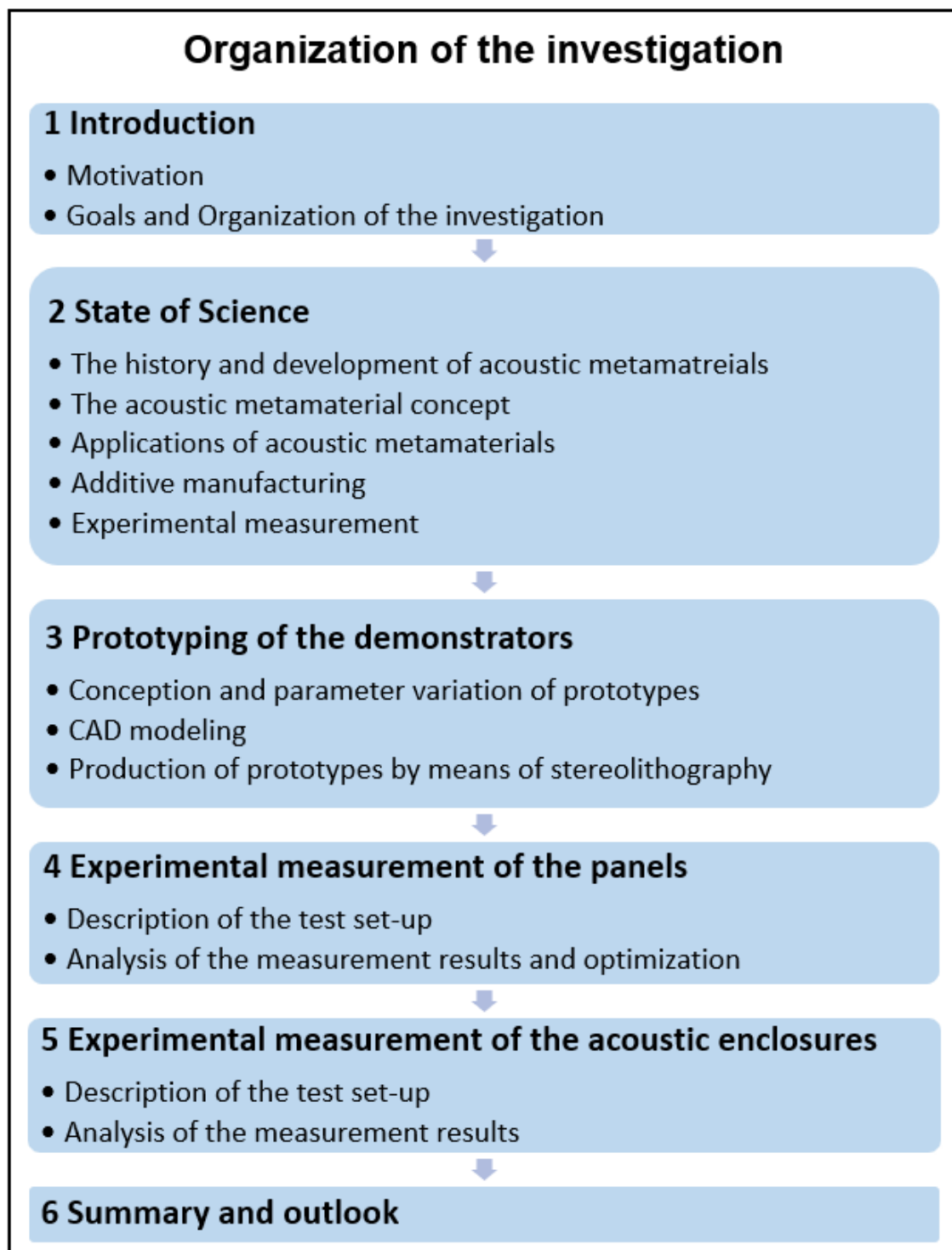


Figure 1.1: Organization of the thesis

2 State of Science

In this chapter, the history of acoustic metamaterials is presented, whereby the focus is on the concepts of acoustic metamaterials. Furthermore, the state of science in the acoustic metamaterial research and applications are pointed out. One also introduces additive manufacturing, which is used in various scientific studies for the production of prototypes. Furthermore, measured physical quantities and set-ups for experimental investigations of acoustic metamaterials are presented.

2.1 The history and development of acoustic metamaterials

The word "metamaterial" is composed of "meta" and "material", whereby the Greek word "meta" stands for "beyond". They are a compound structure of materials divided in multiple unit cells of non-homogeneous material composition and topology, referred to as meta-atoms, that are on a scale much smaller than the wavelength and structured in specific, often periodic patterns. (Van Belle et al., 2016) (Zhang, 2010)

In the 1960s, Veselago developed the first metamaterial concept for electromagnetic waves, according to which a medium with simultaneous negative permittivity and negative permeability has a negative refractive index. This theory was demonstrated in 1996 and also in 1999 by Pendry et al. by creating a structure made of periodic metal rods and by designing an acoustic metamaterial consisting of resonant split rings. (Zhang, 2010) (S. Chen et al., 2018) In the 2000s, Smith et al. developed hybrid structures that included periodic metal rods and resonant split rings, and thus experimentally demonstrated the existence of a negative index. (S. Chen et al., 2018) Besides a negative refractive index one strives to realize a zero refractive index, optical chirality and anisotropy with electromagnetic metamaterials. (Van Belle et al., 2016) Investigations in the field of electromagnetism formed the basis for the research on various research areas such as optics, mechanics, thermotics and acoustics. (Van Belle et al., 2016) Electromagnetic and acoustic waves are fundamentally different from one another. While acoustic waves are longitudinal waves, electric and magnetic waves are transverse waves. However, there are many analogies, which become particularly clear when regarding a two-dimensional acoustic or electromagnetic field with harmonic excitation (see Fig. 2.1). (Zhang, 2010) Like electromagnetic waves, vibrational waves can be influenced in their propagation by a periodic arrangement of scatterers. In 1979 Narayananamurti et al. proposed the first periodic structure to influence the propagation of oscillation waves in the high-frequency range. In the 1990s, Sigalas and Economou demonstrated the existence of band gaps in a structure consisting of spheres arranged periodically in a host structure and in a fluid. In 1995, Francisco Mesegue et al. showed the vibration reducing properties through experiments (see Fig. 2.2). They arranged steel tubes periodically in a square in air in two dimensions and proved that the sound reduction at certain frequencies is caused by the interference of sound waves, because the steel tubes act as scatterers and do not absorb any vibration energy due to their high stiffness. (Deymier, 2013)

In 2000, Liu et al. developed the first acoustic metamaterial. By constructing a unit cell that had sub-wavelength size at the resonant frequency, an acoustic metamaterial with negative effective dynamic density was created. The structure consisted of hard cores with a soft

Acoustics	Electromagnetism (TMz)	Analogy
$\frac{\partial P}{\partial x} = -i\omega\rho_x u_x$	$\frac{\partial E_z}{\partial x} = -i\omega\mu_y H_y$	
$\frac{\partial P}{\partial y} = -i\omega\rho_y u_y$	$\frac{\partial E_z}{\partial y} = i\omega\mu_x H_x$	
$\frac{\partial u_x}{\partial x} + \frac{\partial u_y}{\partial y} = -i\omega\beta P$	$\frac{\partial H_y}{\partial x} - \frac{\partial H_x}{\partial y} = -i\omega\epsilon_z E_z$	
Acoustic pressure P	Electric field E_z	$-E_z \leftrightarrow P$
Particle velocity u_x, u_y	Magnetic field H_x, H_y	$H_y \leftrightarrow -u_x, H_x \leftrightarrow u_y$
Dynamic density ρ_x, ρ_y	Permeability μ_x, μ_y	$\rho_x \leftrightarrow \mu_y, \rho_y \leftrightarrow \mu_x$
Dynamic compressibility β	Permittivity ϵ_z	$\epsilon_z \leftrightarrow \beta$

Figure 2.1: Analogy between acoustic and electromagnetic variables (Zhang, 2010)

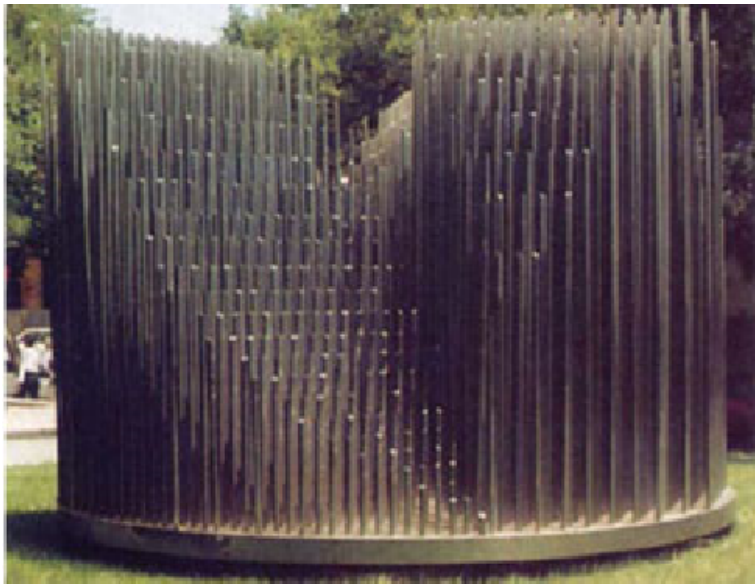


Figure 2.2: Structure to influence the propagation of acoustic waves by Francisco Mesegue (Deymier, 2013)

coating arranged in a cuboid shape and embedded in a hard matrix material. A wave hitting the structure was prevented from propagating and decayed and a low-frequency band gap was generated. (S. Chen et al., 2018) (Zhang, 2010) (?, ?) Moreover, an acoustic metamaterial with negative bulk modulus and simultaneously negative mass density consisting of two types of resonant structural material has been numerically proved. Fang et al. conceptualized

an acoustic metamaterial as a 1D arrangement of helmholtz resonators and experimentally demonstrated a dynamic effective negative modulus. (Zhang, 2010) In general, the research goal is to conceptualize acoustic metamaterials for applications that show great efficiency in low-frequency isolation, energy harvesting, perfect absorption, negative refraction and cloaking. (Dong et al., 2019)

2.2 The concept of acoustic metamaterials

Acoustic metamaterials are divided into three categories, that are based on different work principles. These are acoustic metamaterials with interference stop bands, with locally resonant stop bands and acoustic metamaterials combining both of these concepts. It should be noted, that irrespective of the concept, the isolation properties of noise are currently limited in some particular and tunable frequency ranges, so called stop bands.

- In interference-based stop bands, cells, that act on acoustic waves as scatterers for reflections, are periodically arranged in a structure. The scatterers can be arranged in one to three directions (see Fig. 2.3). If incoming waves hit these scatterers, they are transmitted or reflected. (Claeys, Vergote, Sas, & Desmet, 2013) Through destructive interference of waves in a specific band of frequencies, a band gap is formed with high reflection and low transmission and sound propagation is significantly reduced. (Claeys et al., 2013) (Gupta, 2014)

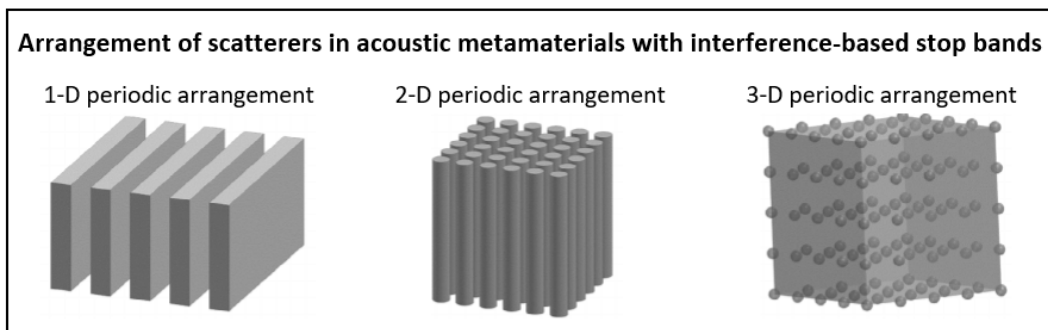
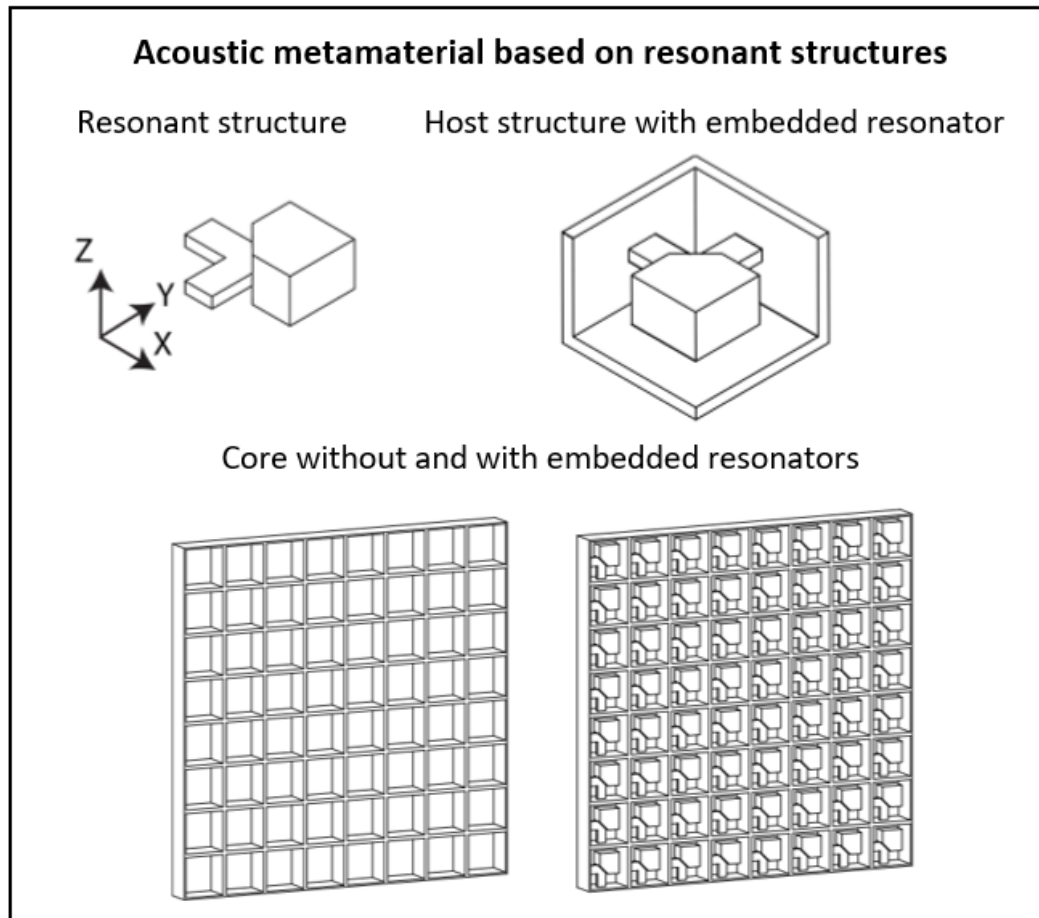


Figure 2.3: Arrangement of scatterers in acoustic metamaterials
(Gupta, 2014)

- In the case of resonance-based stop bands, metamaterials consist of a host structure that is subdivided into several often periodically arranged hollow unit cells. Resonators, that are smaller than the structural wavelengths to be influenced, are embedded in these unit cells. An example is given in Fig. 2.4. (Van Belle et al., 2016) The noise insulation results from specific resonance stop bands, that emerge when incoming waves and the waves re-radiated by resonant cells meet and superimpose and the energy of the propagating waves is stored and delayed. (Van Belle et al., 2016) (Craster & Guenneau, 2012) The combination of material and geometry determines the resonance frequency of the resonant cells and thereby also the stop band frequencies, whereas the spacing between resonant structures does not affect the stop band frequencies. (Van Belle et al., 2016)
- Acoustic metamaterials can also work according to a combination of the two concepts



*Figure 2.4: Acoustic metamaterial based on resonant structures
(Claeys et al., 2016) (Van Belle et al., 2016)*

mentioned above. These acoustic metamaterials consist of structural units that generate local resonances in certain frequency ranges and are arranged in a three-dimensional repeating structure. If an incident wave with angular frequency ω interacts with this medium so that a localized excitation with frequency ω_0 occurs, the linear response functions are proportional to $\frac{1}{\omega_0^2 - \omega^2}$. The wave is exponentially damped. An example is given in Fig. 2.5. (Liu et al., 2000)

Various scientists have done research on the effectiveness of acoustic metamaterials on sound insulation and in the wake of this have developed different prototypes of acoustic metamaterials. In the following, an overview of acoustic metamaterials that have been produced in the course of various scientific studies is given. The prototypes are structured according to the underlying concept of interference-based stop bands, the concept of resonance-based stop bands and the combination of interference-based and resonance-based stop bands.

2.2.1 Prototypes of metamaterials with interference-based stop bands

- To investigate the effectiveness of acoustic metamaterials Guild et al. designed a metamaterial structure which is based on interwoven perpendicular arrangements of cylinders. The acoustic absorber contains three sections which differ in thickness and filling

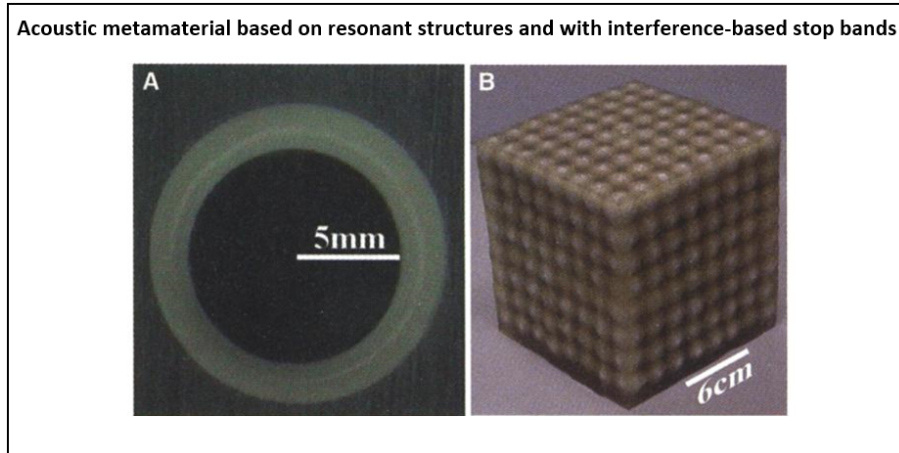


Figure 2.5: Acoustic metamaterial based on resonant structures and with interference-based stop bands

(Liu et al., 2000)

fraction (see Fig. 2.6a). One measured the magnitude and phase of reflection and transmission coefficients of each single section as well as of the multilayer sample using an acoustic impedance tube. (Guild, Rohde, Tothko, & Sieck, 2018)

- Ruiz et al., for instance, created plates of square form by means of additive manufacturing and slit the surfaces by laser cutting (see Fig. 2.6b). They determined the pressure fluctuations in a square tube by means of four microphones and thus the impedance of the specimens. (Ruiz, Claeys, Deckers, & Desmet, 2016)
- Moreover, Al-Zubi et al. constructed so called periodic cellular material structures, which are characterized by a sandwich structure (see Fig. 2.6c). They produced three different variants of prototypes in two sample sizes, whose absorption coefficients were determined using an impedance tube. The first prototype consists of an aluminium pyramidal core, the second variant has a prismatic aluminum structure and the last model is a body made of stainless steel with a triangular honeycomb. (Al-Zubi et al., 2013)

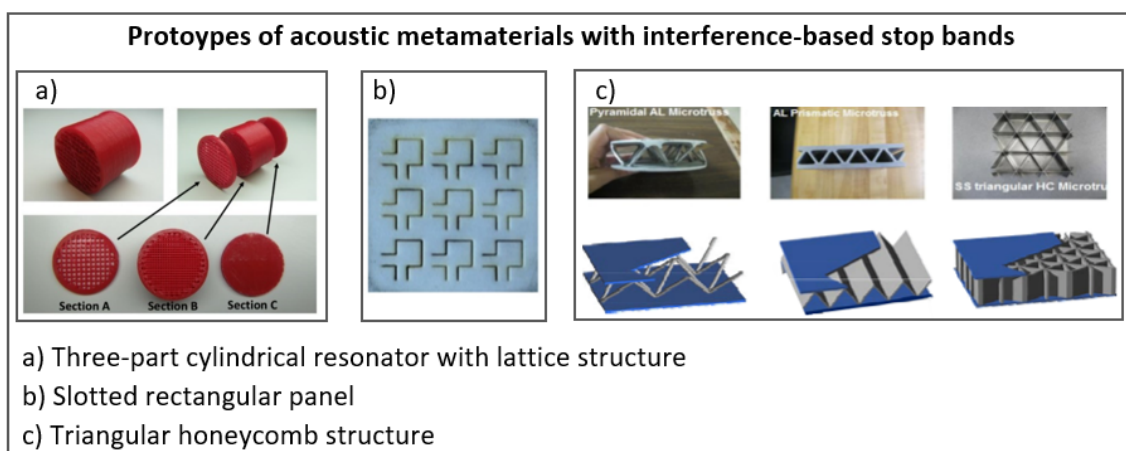


Figure 2.6: Demonstrators of acoustic metamaterials based on interference stop bands

(Guild et al., 2018) (Al-Zubi et al., 2013) (Ruiz et al., 2016)

2.2.2 Prototypes of metamaterials with resonance-based stop bands

- Chen et al., for example, designed hollow steel tubes, of which they pasted a single tube on a cylindrical sponge matrix in one variant and in a further version they arranged several tubes in parallel on the two surfaces of a cylindrical sponge matrix. Furthermore, they constructed a prototype, which is based on the two-layer model, but contains additional spherical structures besides tubes. (see Fig. 2.7a). These constructs are placed in an acoustic impedance tube to determine amplitudes and phase curves of transmission and reflection by processing the obtained data using the transfer function method. (H. Chen, Zeng, Ding, Luo, & Zhao, 2013)
- Amado-Mendes et al., in turn, built two metamaterial structures. The first design consists of a periodic arrangement of beam elements with a larger mass in the extremity, fixed to the vertical side walls of cavities of a base structure. The second design is essentially similar to the first version, but the resonators are formed as rectangular blocks (see Fig. 2.7b). In addition, both objects are made from two different materials. (Amado-Mendes, Godinho, Dias, Amaral, & Pinho, 2018)
- Moreover, Dong et al. fabricated a sample of slabs and put them in an experimental apparatus consisting of acoustic absorbing foams to avoid reflections, a loudspeaker and a microphone to investigate the subwavelength imaging (see Fig. 2.7c). (Dong et al., 2019)
- Besides these prototypes, Claeys et al. built an one open side acoustic enclosure, whose inner side surfaces are designed as lattice structures into which resonators are inserted (see Fig. 2.7d). It is placed over a small speaker to determine the acoustic insertion loss by comparing sound radiation with and without enclosure. (Claeys et al., 2018)

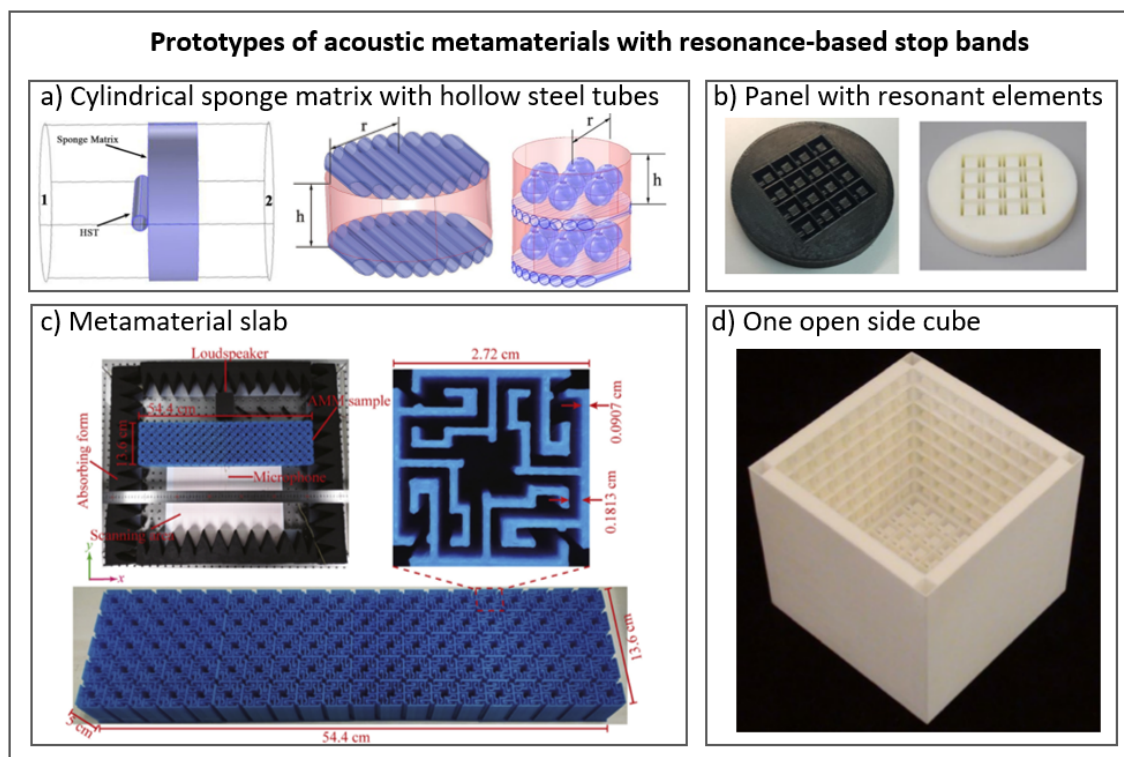


Figure 2.7: Demonstrators of acoustic metamaterials based on resonance stop bands
(H. Chen et al., 2013) (Dong et al., 2019) (Amado-Mendes et al., 2018) (Claeys et al., 2018)

2.2.3 Prototypes of metamaterials combining interference-based and resonance-based stop bands

- Liu et al. designed an acoustic metamaterial as presented in Fig. 2.8, that combines the concepts of interference and resonance-based band gaps. It consists of composites, each with a solid core material and a coating of elastic soft material. The bodies are arranged in a three-dimensional cubic crystal. The size and geometry of the elements are varied to tune the effective frequency ranges and the sound transmission of the demonstrator is measured. (Liu et al., 2000)

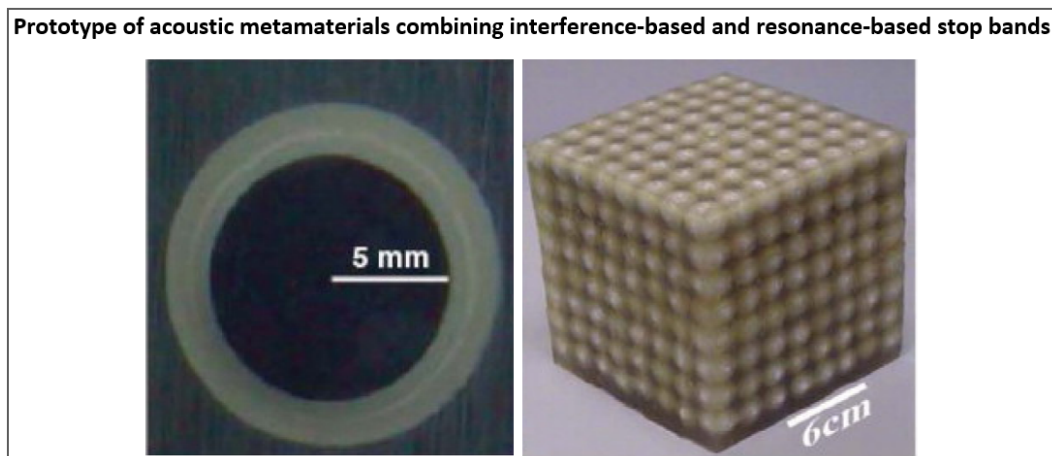


Figure 2.8: Demonstrator of acoustic metamaterials combining interference and resonance stop bands

(Liu et al., 2000)

2.3 Categories of acoustic metamaterials

Although acoustic metamaterials are currently still investigated within the framework of scientific research, possible future applications of the technology have already been proposed.

- **Traffic**

In order to reduce traffic noise, a sound insulation made of acoustic metamaterials is proposed. This consists of an arrangement of plastic tubes mounted on metal plates that can move in relation to each other (see Fig. 2.9a). The plates of the structure can unfold at variable angles when they are compressed or stretched, thus changing the distances between the tubes evenly. As a result, the sound insulation can be adapted to the frequency range to be blocked and the volume in individual frequency ranges can be reduced by up to 90 %. Tests as well as an already used prototype proved the effectiveness of this flexible sound barrier in the frequency range between 500 Hz and 1500 Hz, where most frequencies are perceived as disturbing traffic noise. (Loefken, 2017b)

- **Automobile industry**

In addition, the use of acoustic metamaterials in vehicles, for example for the insulation of noise generated by the powertrain, is investigated. A metamaterial is fixed to the

inner side of the firewall as presented in Fig. 2.9c and a good damping of the acoustic transmission is achieved. (Chang, Jung, Kim, Choi, & Wang, 2018)

- **Aviation industry**

Langfeldt's research addresses the use of membrane-like acoustic metamaterials in an aircraft noise control design. The goal is to reduce low-frequency cabin noise caused by counter-rotating open rotor (CROR) engines. Therefore, a metamaterial construction is attached to an acoustic fuselage demonstrator. The metamaterial is made of a thin, prestressed membrane layer to which several small, rigid masses are attached. The final prototype consists of a cover sheet and these metamaterial layers, which are inserted between a protective foil and the fuselage (see Fig. 2.9d). The fuselage structure is excited by pink noise through a movable speaker array system with 132 individually controllable loudspeakers. These simulate the flight noise of a CROR engine. The resulting sound pressure on the fuselage is measured with a microphone array at 240 points. With the prototype an improvement of the noise suppression of up to 3 dB at 100 Hz is achieved. (Langfeldt, 2018)

- **Consumer industry**

According to one approach, a metamaterial made of plastic is formed in such a way that it sends incoming sounds back to the location of the sound source. As a result, the transmitted sound waves are disturbed and not radiated through the structure. In measurements 94% of the sound emitted by a speaker was reduced and was not audible. One possible application is to make drones and ventilators quieter. The open metamaterial structure can be placed underneath the noisy drone or air conditioning ventilator and cancels sound without affecting the stability of the drone or the circulation of hot or cold air. A prototype is presented in Fig. 2.9b. (McAlpine, 2019)

- **Building industry**

- One has done research on an application, which is to camouflage objects acoustically. "Cloaks of invisibility" made of metamaterials bend incident sound waves so that an object enveloped by them apparently disappears. The sound waves are redirected around the objects to be covered. For instance, these structures may be used in concert halls or theaters to improve the acoustics by controlled distraction of sound waves (see Fig. 2.9e). (Spektrum, 2011)
- Fig. 2.9f shows a prototype of an acoustic metamaterial used to control sound so that a desired noise is generated. The possibility of almost arbitrary redirecting waves to various directions and the great variety of materials and possible dimensions of the products open up sound design of buildings as a further field of application for acoustic metamaterials. (Loefken, 2017a)

- **Medical technology**

Acoustic metamaterials can affect the propagation of waves with greater variability than other previously used materials. This potential can be harnessed in medicine to influence wave propagation, such as ultrasonic waves, as desired. It thus supports the control of highly focused ultrasound waves that targeted destroy tumor tissue in the body (see Fig. 2.9f). (Loefken, 2017a)

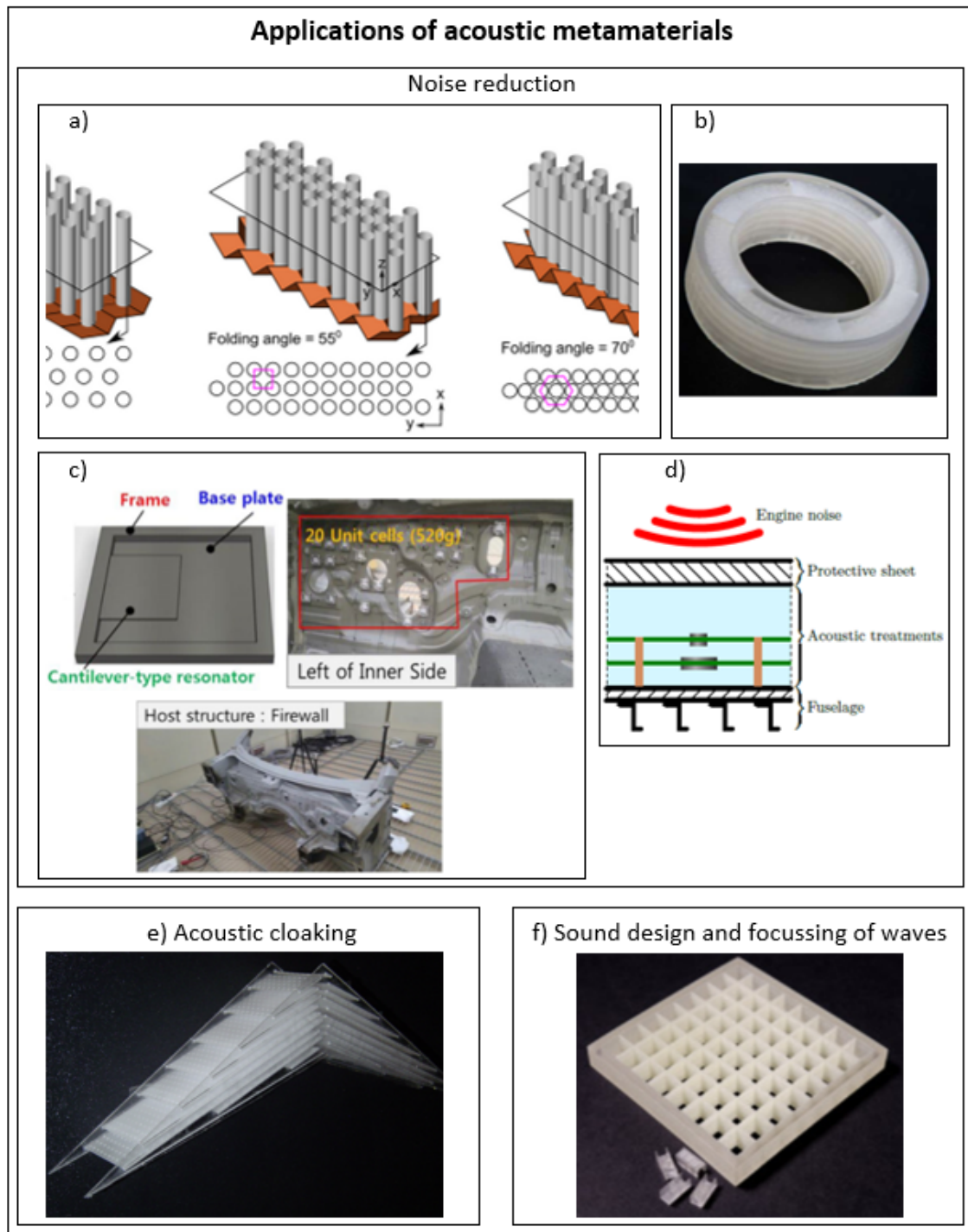


Figure 2.9: Applications of acoustic metamaterials

(Loefken, 2017b) (McAlpine, 2019) (Chang et al., 2018) (Spektrum, 2011) (Loefken, 2017a) (Langfeldt, 2018)

2.4 Additive manufacturing technologies

According to ASTM International, additive manufacturing refers to the generation of objects in layers from three-dimensional (3D) model data by joining materials. (Richter & Wis-

chmann, 2016) Many of the demonstrators referred to in Sec. 2.2 are made by means of additive manufacturing (AM). For example, Claeys et al. used selective laser sintering to fabricate models for experiential measurements. (Claeys et al., 2018) Guild et al. built their prototypes using fuel deposition modeling. (Guild et al., 2018) Amado-Mendes et al. investigated the fabrication of objects using the methods fuel deposition modeling and multi jet modeling. (Amado-Mendes et al., 2018)

2.4.1 Working steps of additive manufacturing

The manufacturing process basically comprises the three steps "data preparation", "layered object construction" and "post-processing". Only the printing of the object is made automated, while data preparation and post-processing are carried out manually (see Fig. 2.10). (Acatech, 2016)

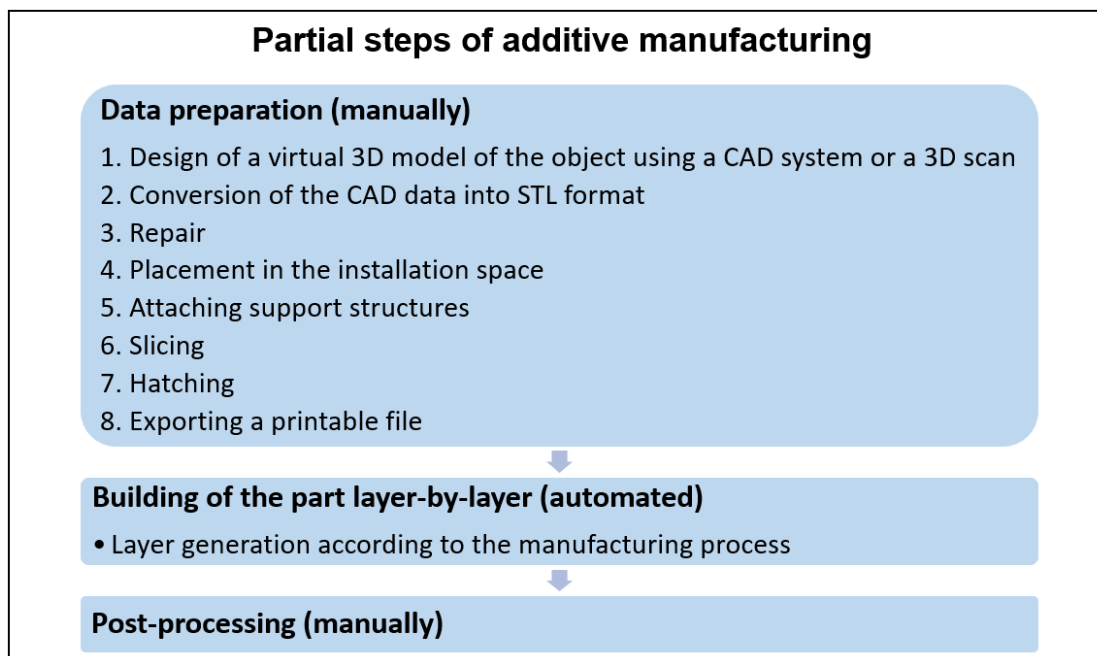


Figure 2.10: Partial steps of additive manufacturing
(Acatech, 2016)

- Data preparation

The first step is data preparation, that in turn consists of eight partial steps. First, a computer-aided 3D model of the component is created using a CAD program or a 3D scanner. The component surface generated in this way is represented by individual points, which are covered with a triangular network in the next step. In this step, the file is converted into a STL format (surface tessellation language), which contains geometric information of the three-dimensional data model. Due to the vulnerability of .stl files to inconsistencies, a repair ensures that the volume is completely and accurately enclosed by triangles. In the fourth step, the object is placed and aligned in the printer's installation space. For some manufacturing processes, supports are required that are either generated automatically or added manually in the following sub-step. The number of attachment points and dimensions of the supports have a decisive influence on the manufacturability of a

component, the process stability and the post-processing effort. In the sixth step, the 3D model is cut into horizontal layers, with each layer containing a contour of the object in polygon courses. During hatching, the contours are filled with hatches that are later printed by the 3D printer. The set parameters and boundary conditions for component geometry, material, machine and process are decisive for the quality of the printed object. Finally, the model is exported as a printable file and imported into the 3D printer. (Acatech, 2016)

- Layered object construction

In the second step, the component is built up layer by layer. Before starting the printing process, the 3D printer must be set up (calibration) and printing parameters must be defined (e.g. layer thickness and printing time). (Richter & Wischmann, 2016) The generation of the layers depends on the respective manufacturing process. Additive manufacturing is also referred to as direct digital manufacturing, since the layered structure of the object makes the time-consuming and cost-intensive use of casting moulds redundant. This eliminates the need to consider conventional limitations for component geometries such as undercuts or draft angles. Restrictions in the design freedom result only from the respective manufacturing process. If supports are required to realize overhangs, the connection points must be accessible in order to be able to remove the supports again after the print. (Acatech, 2016)

- Post-processing

After printing is finished, the component can be removed from the printer and, depending on the printing process, can be used immediately or needs to be individually finished. Possible work steps are the removal of excess printing material or the priming or painting of the created objects. (Richter & Wischmann, 2016)

2.4.2 Categorization of additive manufacturing processes

Classification of additive manufacturing technologies according to the materials and the respective joining principle

The usable materials and achievable product properties are determined by the physical or chemical principle according to which the raw material is joined together and by the process conditions specified by the installation. (Acatech, 2016) A categorisation of additive or generative manufacturing processes can be carried out by distinguishing the technologies according to the joining principle and the materials used in the plants, respectively. A basic distinction is made between solid or liquid starting materials (see Fig. 2.11). Solid materials are for example wire, powder or foils. (Peters, 2018)

Classification of additive manufacturing technologies according to the physical active principle

A further criterion for categorizing additive manufacturing processes is the physical active principle, according to which the layered construction of the objects takes place. Wires are

fused and solidify after shaping, which is referred to as fused deposition modelling (FDM). Powder can be melted and solidified according to the principle of selective laser sintering (SLS) or selective laser melting (SLM) or it is bonded by a binder using the process of 3D-printing (3DP). The generation of objects using foils or plates which are cut out and joined is called laminated object modelling (LOM). In the case of liquid raw materials, shaping is carried out by photopolymerisation according to stereolithography (SLA) (see Fig. 2.11). (Peters, 2018)

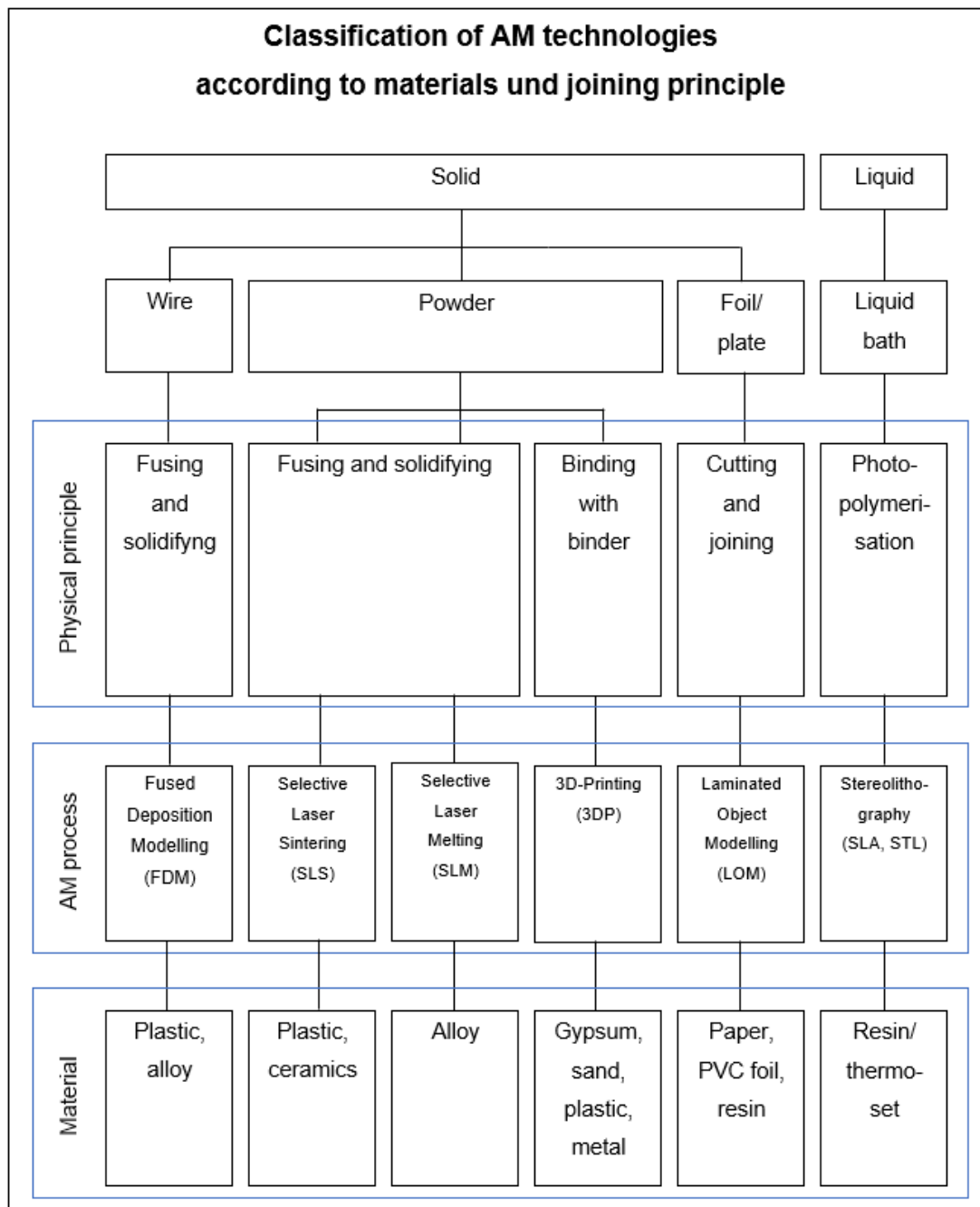


Figure 2.11: Classification of AM technologies according to materials und joining principle
(Peters, 2018)

Classification of additive manufacturing technologies according to facility groups

In addition, the component requirements determine the additive manufacturing process. The additive manufacturing technologies are thus significantly different from each other. (Richter & Wischmann, 2016) The production facilities can be divided into the process groups (Ruettinger, n.d.)

- binder jetting (BJT),
- directed energy deposition (DED),
- material extrusion (MEX),
- material jetting (MJT),
- powder bed fusion (PBF),
- sheet lamination (SHL) and
- photopolymerisation (VPP).

Fields of application of additive manufacturing technologies

The decision for an additive manufacturing technology is also influenced by the intended use of the technique. There are basically three types of additive manufacturing processes, which are rapid prototyping, rapid tooling and rapid manufacturing (see Fig. 2.12). Rapid Prototyping is aimed at a fast production of prototypes whose component properties do not correspond to those of the end product. Rapid Tooling is used for the rapid production of complex geometries in tool making and mould construction. Rapid or direct manufacturing is used to implement flexible and prompt production of final components with complex geometric structures which can be installed after postprocessing. (Richter & Wischmann, 2016) (Acatech, 2016)

Application types of additive manufacturing		
Rapid Prototyping	Rapid Tooling	Rapid or Direct Manufacturing
Prototypes and specimen components whose component properties differ from those of the end product	Moulds and models, tools such as fixtures, gauges and drilling jigs	Final components with complex geometric structure, which can be installed after post-processing

Figure 2.12: Application types of additive manufacturing
(Acatech, 2016)

2.4.3 Selection of the additive manufacturing technology

The process of using additive manufacturing technologies described in Sec. 2.4.1 applies to all technologies. Since each technology has individual advantages and disadvantages and is therefore not equally suitable for all applications, six criteria are taken into account when deciding on an additive manufacturing process. The technologies can be categorized according to the characteristics (Peters, 2018)

- application,
- joining principle and usable materials,
- realizable accuracy,
- possible mechanical quality and postprocessing,
- maximum installation space and
- budget.

2.4.4 Stereolithography

The criteria listed in Sec. 2.4.3 are considered when choosing the additive manufacturing process for the present task. For the building of the models the additive manufacturing process stereolithography (SLA) is used. It is developed at the University of Texas in Austin in the early 1980s and is the oldest additive manufacturing principle. (Peters, 2018)

- **Application**

In the present work, the demonstrators of the acoustic metamaterials are made by means of rapid prototyping. Specimens are only used for experiments, so that a small number of objects of one type is sufficient. Since one to four versions are produced for each model, the number of pieces is very small. Furthermore, the demonstrators do not represent end products. The properties of the test objects are selected in such a way that it is possible to investigate the performance of the structures in terms of noise reduction. End products with defined properties are not conceptualized but the objects are constructed to perform an experimental investigation of parameter variations and to derive changes in geometry to improve sound absorption.

- **Joining principle and usable material**

Stereolithography uses photopolymerization to build objects in a vat of resin. A laser light source or controlled surface luminaire (Acatech, 2016) effects on a photosensitive photopolymer that cures locally where the laser beam or UV light hits the material (see Fig. 2.13). (Peters, 2018) The focussed laser beam or the UV light are led by scan mirrors and micro-mirror arrays (digital light processing (DLP)), respectively. In any case, a controlled illumination is performed, which draws the contour of the object in the liquid and the light source only hits material that is within this contour. (Acatech, 2016) A single layer is created by lowering the printing platform one thickness below the surface of the resin bath. The material then cures in this layer as soon as the photopolymer is exposed by the laser. In this way, the part is printed layer by layer. The objects, i.e. the already printed parts of them, are stabilized by support structures that are removed from the component after completion. After removing the object from the printer, the component is cured under UV light.

Objects are created from exclusively liquid photopolymers, such as epoxy or acrylic resins. The available materials differ in properties such as transparency, flexibility and ductility and are usually matched to a special printer. (Peters, 2018) (Just3DP, 2016)

- **Realizable accuracy**

To date, the highest accuracies have been achieved with this process, since the resolution of the objects only depends on the light beam of the projector, which can be

emitted as a very narrow beam. (Just3DP, 2016) Moreover one can realize a very small layer thickness and a detail resolution of 0.01 to 0.02 mm. The surface of the object is very smooth and the individual layers are no longer visible, because there is little pressure on the model during the printing process. (Peters, 2018) (Just3DP, 2016) Due to the high print quality, the process is used to create complex objects with even surfaces. (Just3DP, 2016) SLA is used, for example, in model making for the creation of study objects, in the manufacture of casting moulds, in the production of nano- and microstructures, in the dental sector and in medical technology or in the jewellery and toy industry. (Peters, 2018) (Just3DP, 2016) In the cured state, the objects have sufficient stability and temperature resistance only between 50 - 60 °C, which is why the aim is to improve thermal stability. A disadvantage of objects manufactured using SLA technology is their low durability, as the models age when exposed to light. (Just3DP, 2016) Furthermore, it is not possible to use different materials at the same time during a printing process and the resins are polluting. (Peters, 2018)

In the present case, the geometries of the prototypes to be generated are very small and must be exactly represented. Due to advantages of stereolithography such as high accuracy, very small realizable layer thicknesses, the possibility to create complex objects and the high stability, the method is very well suited for the prototyping process.

- **Possible mechanical quality and post-processing**

When the print is finished, there is still liquid resin on the surfaces and in cavities of the object, which must be removed - for example in a bath of isopropyl alcohol. If support material is required for the print, this must also be removed. (Just3DP, 2016) In order to improve the surface quality, the printed object can be finished by varnishing, painting, metallizing, polishing or machining. (Peters, 2018)

In the present case, a high surface quality of the test specimens is of great importance in order to exclude the occurrence of measurement results being falsified as a result of manufacturing inaccuracies. Due to the simple post-processing of the printed test specimens, the surfaces of the samples can be finished individually until the desired result is achieved.

- **Maximum installation space**

Basically, components can be formed by assembling several objects. Typical installation spaces for printers range from 250.00 × 250.00 × 250.00 mm (length × width × height) to 1000.00 × 800.00 × 500.00 mm, while a "mammoth stereolithography system" has installation space dimensions of 2100.00 × 700.00 × 800.00 mm. (Peters, 2018)

In this paper, the dimensions of the test objects do not exceed 60.00 × 60.00 × 60.00 mm. Thus, there are no restrictions in the production of the objects due to a limited installation space of a machine working according to the method of stereolithography.

- **Budget**

Due to its comparatively early development, SLA is the most commonly used additive manufacturing process, although the costs for precise printers are over 50000.00 euros and the material costs are about four times as expensive as for extrusion lines such as fused deposition modeling. (Peters, 2018) The printing costs for SLA printing comprise the material costs for the resin needed to create the objects and maintenance cost. As the number of printing processes increases, the resin tank becomes dirty, so

that the light source can no longer project the image accurately into the resin bath. Removing the objects from the printing platform can scratch it severely. The tank and the printing platform should therefore be replaced if they become very dirty or damaged. (Just3DP, 2016)

A stereolithography-based system is already part of the chair's inventory, so that there are no acquisition costs for a printer. Since one copy of each test specimen is built, the total number of objects is relatively small. As only material costs are accrued, these are not an exclusion criterion for the process despite their high values.

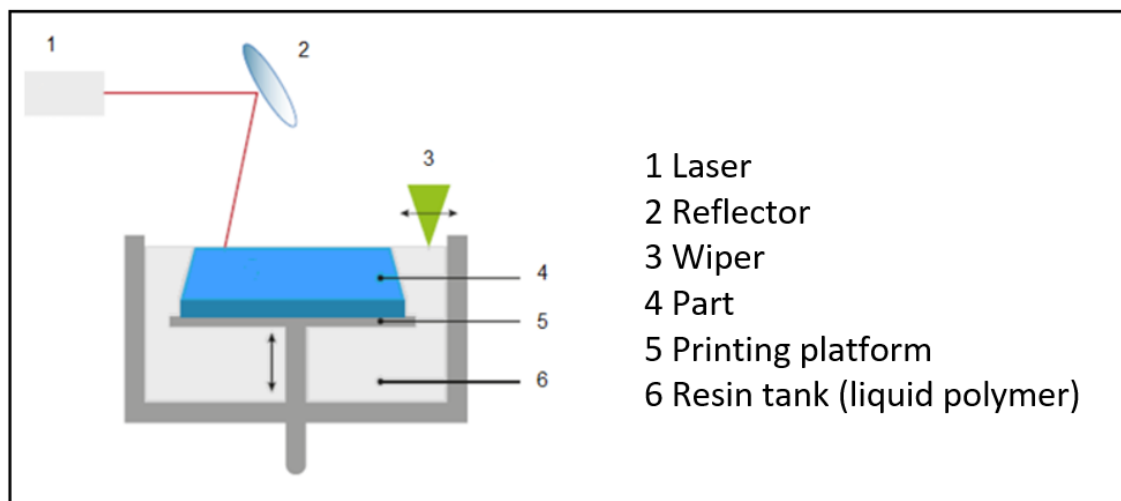


Figure 2.13: Stereolithography
(Peters, 2018)

2.5 Experimental measurement

In various studies additional simulations of acoustic metamaterials are carried out, which at high consistency with experimental investigations can substantiate the results. (Claeys et al., 2018) (Dong et al., 2019) (Guild et al., 2018) Since the implementation of simulations of acoustic metamaterials is very difficult and a simulation cannot replace measurements, the present work is limited to the experimental investigation of the manufactured prototypes.

2.5.1 Measured physical quantities

An important parameter to characterize the acoustic properties of prototypes is the absorption coefficient. In various studies on acoustic metamaterials, it is measured using an acoustic impedance tube, whereby the investigation is limited to one-dimensional sound propagation. In addition, the sound pressure level for demonstrators can be determined to measure three-dimensional sound propagation and noise insulation. In the following, the two measured quantities absorption coefficient and sound pressure level are explained.

Absorption, reflection and transmission coefficient (α, ρ, τ)

When a plane wave hits a barrier at normal incidence, e.g. a wall, it is partly reflected there, depending on the surface quality, and the remaining part is absorbed by the obstacle. The absorbed sound energy is composed of a part of dissipated sound energy that is converted into heat at or behind the interface and a part of transmitted energy. This sound energy passes the barrier and is radiated into the adjacent room (see Fig. 2.14). (DEGA, 2006)

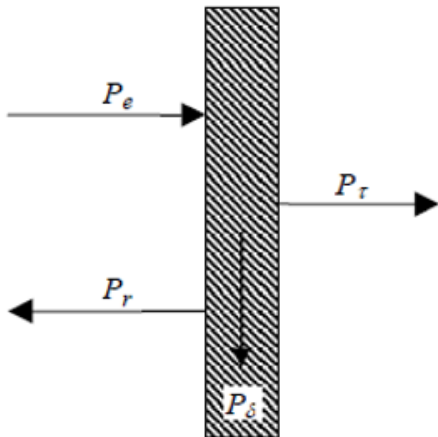


Figure 2.14: Power balance for sound waves at a barrier
(DEGA, 2006)

Accordingly, the energy or power of the incident wave is divided, which can be described by an energy or power balance established at the obstacle as follows (DEGA, 2006)

$$P_e = P_r + P_\delta + P_\tau . \quad (2.1)$$

There, P_e indicates the energy of the incident wave, P_r the energy of the reflected wave, P_δ the energy of the dissipated wave and P_τ the energy of the transmitted wave. Dividing all quantities by the energy of the incident wave, Eq. 2.1 can be written as (DEGA, 2006)

$$\begin{aligned} 1 &= \frac{P_r}{P_e} + \frac{P_\delta}{P_e} + \frac{P_\tau}{P_e} \\ 1 &= \rho + \delta + \tau . \end{aligned} \quad (2.2)$$

The reflection, dissipation and transmission coefficients, which are dimensionless values, are expressed by ρ , δ and τ and are calculated according to Eq. 2.3. (DEGA, 2006)

$$\begin{aligned} \rho &= \frac{P_r}{P_e} \\ \alpha &= \frac{P_\delta + P_\tau}{P_e} = \delta + \tau = 1 - \rho \\ \delta &= \frac{P_\delta}{P_e} \\ \tau &= \frac{P_\tau}{P_e} \end{aligned} \quad (2.3)$$

Sound pressure p and sound pressure level L_p

The sound pressure p describes the pressure fluctuations of a medium, in this case air, which occur during sound propagation. It is calculated according to Eq. 2.4 from the difference between the local sound pressure p_{total} and the static pressure p_0 (DEGA, 2006)

$$p = p_{total} - p_0 \quad . \quad (2.4)$$

By forming the logarithm of the square of the ratio of the effective value of the sound pressure \tilde{p} to the static pressure $p_0 = 2 \cdot 10^{-5} Pa$, the sound pressure level L_p , which is expressed in Decibel (dB) is obtained according to Eq. 2.5. (DEGA, 2006)

$$L_p = 10 \lg \left(\frac{\tilde{p}}{p_0} \right)^2 dB = 20 \lg \frac{\tilde{p}}{p_0} dB \quad (2.5)$$

2.5.2 Set-up

The acoustic properties of the above demonstrators mentioned in Sec. 2.2.1 are measured within various experimental studies. Different tools are used and set-ups are built up to experimentally determine various physical quantities.

Acoustic impedance and transmission tube - absorption, reflection and transmission coefficient

- Acoustic impedance tube with two microphones

- Theory of the acoustic impedance tube

The acoustic impedance tube is an apparatus to measure acoustic properties of materials. It is used in a standard procedure to determine the sound absorption coefficient α at normal incidence according to DIN EN ISO 10534 – 2 (Acoustics - Determination of sound absorption coefficient and impedance in impedance tubes) of the International Standard Organisation (ISO) (DIN, 2001) or ASTM E1050 – 19 (Standard Test Method for Impedance and Absorption of Acoustical Materials Using a Tube, Two Microphones and a Digital Frequency Analysis System of ASTM International). (International, 2019)

The functioning of the acoustic impedance tube is based on the principle of the Kundt tube, that consists of a tube with a small diameter compared to its length. The acoustical material properties are identified with a digital frequency analysis system (Kunio, Yoo, Jou, Bolton, & Enok, 2009) according to the transfer function method. (AED, n.d.) A sound source and a test sample, whose reflection or absorption coefficients are to be measured are mounted on each end of the tube and two microphones are fixed in front of the sample. (Kunio et al., 2009) When a wave propagates along the tube and hits the sample, it is reflected to a greater or lesser extent depending on the reflection factor of the material. If incident and reflected waves overlap, a standing wave is formed, whose minima and maxima provide information about the reflection factor and thus the absorption coefficient

of the material sample. (Hiebel, 2005)

- Structure of the acoustic impedance tube

The impedance tube is assembled as shown in Fig. 2.15a. It consists of a speaker module, an absorption tube and a specimen holder. (AED, 2019) A broadband white noise, which is generated by a noise generator and whose signal strength is reinforced by an amplifier, is fed to the tube via a loudspeaker. (Brunnader, 2002) The waves propagate in the tube, where they hit a sound absorbing sample placed in front of a hard termination.

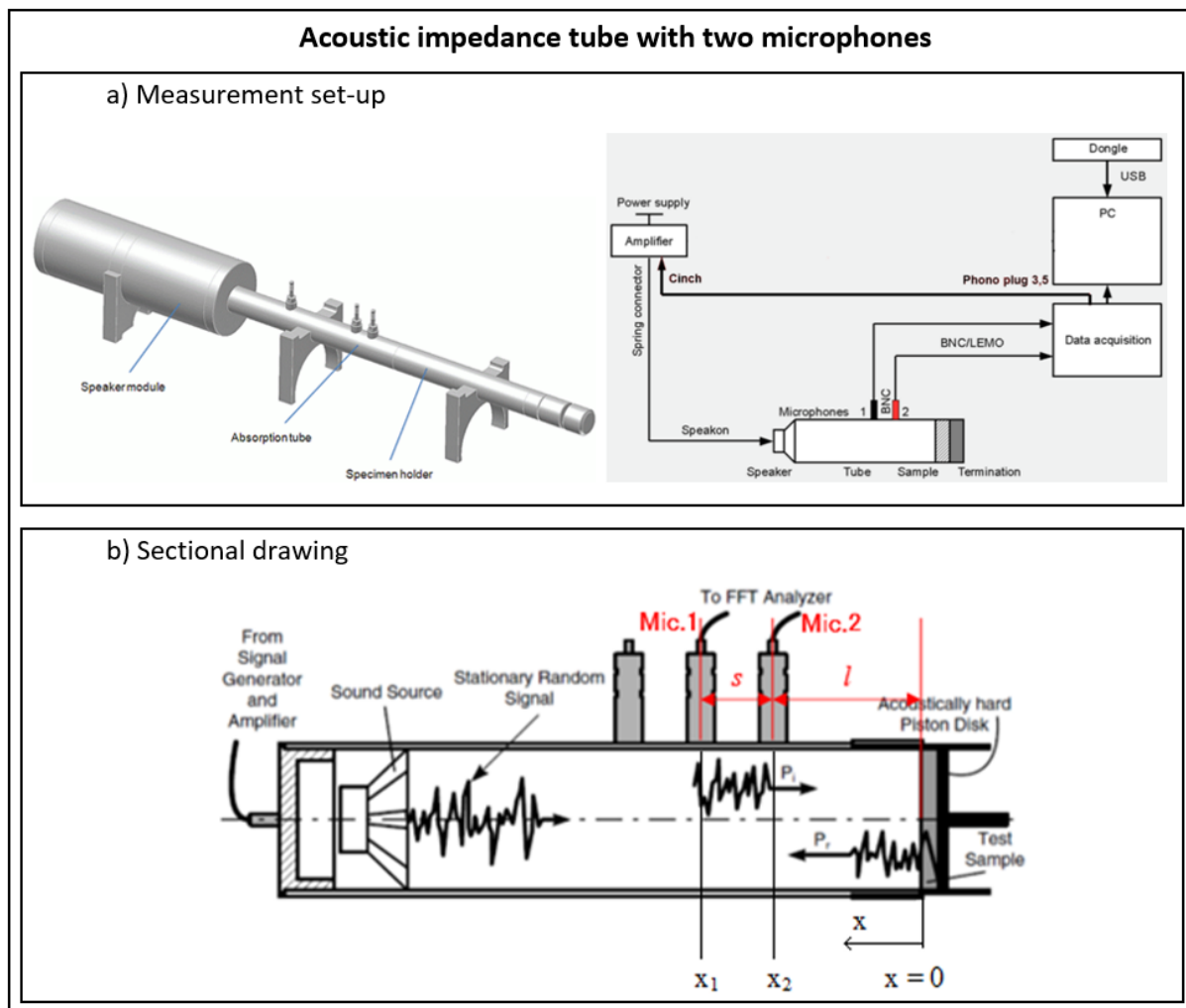


Figure 2.15: Acoustic impedance tube with two microphones
(AED, n.d.) (Kimura, Kunio, Schuhmacher, & Ryu, 2014)

Two microphones Mic. 1 and Mic. 2 mounted at fix positions in front of the sample measure the resulting sound pressures \underline{p}_1 and \underline{p}_2 , which are composed of components of the incident wave \underline{p}_e and the reflected wave \underline{p}_r (see Fig. 2.15b and Eq. 2.6). (Brunnader, 2002)

$$\begin{aligned}
 \underline{p}_1 &= \underline{p}_e(0)e^{jkx_1} + \underline{p}_r(0)e^{-jkx_1} \\
 \underline{p}_2 &= \underline{p}_e(0)e^{jkx_2} + \underline{p}_r(0)e^{-jkx_2} \\
 \underline{p}_1(x, \omega) &= \underline{p}_e(0) \cdot e^{jkx_1} + \underline{p}_r(0) \cdot e^{jkx_1} \\
 \underline{p}_2(x, \omega) &= \underline{p}_e(0) \cdot e^{jkx_2} + \underline{p}_r(0) \cdot e^{jkx_2}
 \end{aligned} \tag{2.6}$$

From this, the complex transfer function \underline{H}_{12} is calculated by transforming the sound pressure into the frequency range by Fourier transformation according to Eq. 2.7. (Brunnader, 2002)

$$\underline{H}_{12} = \frac{\underline{p}_2(x, \omega)}{\underline{p}_1(x, \omega)} = \frac{\underline{p}_e(0) \cdot e^{jkx_2} + \underline{p}_r(0) \cdot e^{-jkx_2}}{\underline{p}_e(0) \cdot e^{jkx_1} + \underline{p}_r(0) \cdot e^{-jkx_1}} \tag{2.7}$$

Analogous to the sound energy (see Eq. 2.3) the sound pressure of the reflected wave can be calculated as $\underline{p}_r = \rho \cdot \underline{p}_e$. By inserting this in the formula above, Eq. 2.7 becomes (Brunnader, 2002)

$$\underline{H}_{12} = \frac{\underline{p}_e(0) \cdot e^{jkx_2} + \rho \cdot \underline{p}_e(0) \cdot e^{-jkx_2}}{\underline{p}_e(0) \cdot e^{jkx_1} + \rho \cdot \underline{p}_e(0) \cdot e^{-jkx_1}} = \frac{e^{jkx_2} + \rho \cdot e^{-jkx_2}}{e^{jkx_1} + \rho \cdot e^{-jkx_1}} \tag{2.8}$$

and the reflection coefficient $\rho = \frac{(\underline{H}_{12} - e^{-jk(x_1-x_2)}) \cdot e^{jkx_1}}{(e^{jk(x_1-x_2)} - \underline{H}_{12}) \cdot e^{-jkx_1}}$. The absorption coefficient α can be derived by setting $\underline{\alpha} = 1 - \underline{\rho}$, which is in accordance with Eq. 2.3. (Brunnader, 2002)

- **Sound transmission tube with four microphones**

- **Theory of the sound transmission tube**

Similar to the calculation of the reflection and absorption coefficient with the acoustic impedance tube, the calculation of the normal incidence properties of acoustic materials is carried out with the transmission tube according to test method ASTM E2611-09. The transmission tube consists of a tube with a sound source attached to one end and a non-reflective termination at the other end (see Fig. 2.16). The source generates a broadband signal and thus allows waves to propagate in the tube. In the middle of the tube is a test specimen, next to which two microphones Mic.1 to Mic.4 are mounted on each side. These microphones measure the sound pressure from which the transmission loss can be calculated. (Kunio et al., 2009)

- **Structure of the sound transmission tube**

The standing wave pattern is separated into forward and backward moving components according to Eq. 2.9 by examining the relative amplitude and phase of the sound pressures measured at the four measuring positions. The coefficients A, B, C and D describe the amplitudes of the four plane waves and k is a complex

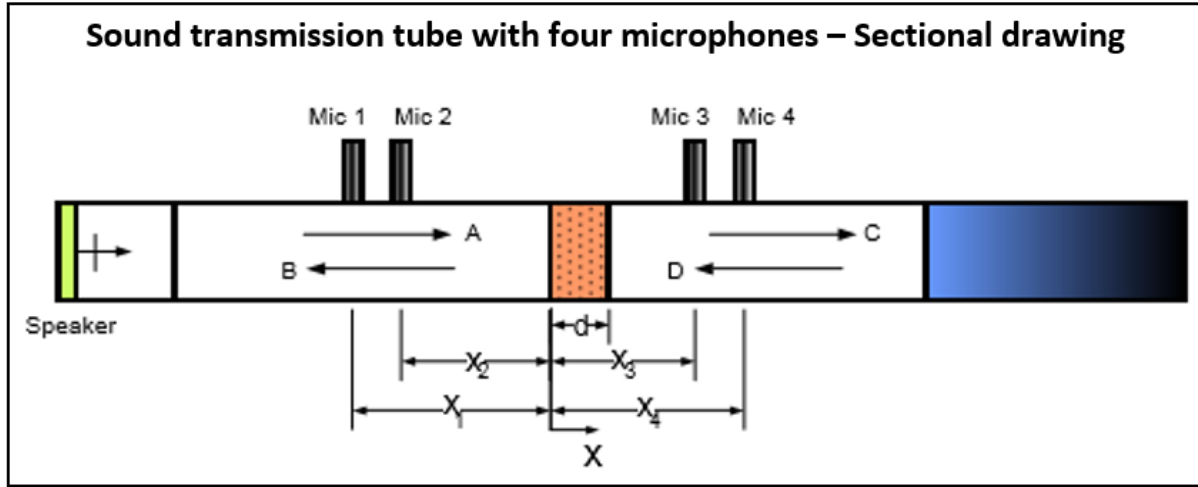


Figure 2.16: Sound transmission tube with four microphones
(Kunio et al., 2009)

wave number. (Kunio et al., 2009)

$$\begin{aligned} P_1 &= (Ae^{-jkx_1} + Be^{jkx_1}) e^{j\omega t} \\ P_2 &= (Ae^{-jkx_2} + Be^{jkx_2}) e^{j\omega t} \\ P_3 &= (Ce^{-jkx_3} + De^{jkx_3}) e^{j\omega t} \\ P_4 &= (Ce^{-jkx_4} + De^{jkx_4}) e^{j\omega t} \end{aligned} \quad (2.9)$$

The transfer matrix is calculated from the respective pressure P and the respective particle velocity V on both sides of the sample, which extends from point $x = 0$ to $x = d$ according to Eq. 2.10. (Kunio et al., 2009)

$$\begin{bmatrix} P^{(a)} & P^{(b)} \\ V^{(a)} & V^{(b)} \end{bmatrix}_{x=0} = \begin{bmatrix} T_{11} & T_{12} \\ T_{21} & T_{22} \end{bmatrix} \begin{bmatrix} P^{(a)} & P^{(b)} \\ V^{(a)} & V^{(b)} \end{bmatrix}_{x=d} \quad (2.10)$$

By performing tests with two different terminations (a) and (b), the 2×2 transfer matrix is solved and yields (Kunio et al., 2009)

$$\begin{bmatrix} T_{11} & T_{12} \\ T_{21} & T_{22} \end{bmatrix} = \frac{1}{P^{(a)} \left| \begin{array}{c} V^{(b)} \\ V^{(a)} \end{array} \right|_{x=d} - P^{(b)} \left| \begin{array}{c} V^{(a)} \\ V^{(b)} \end{array} \right|_{x=d}} \cdot \begin{bmatrix} P^{(a)} \left| \begin{array}{c} V^{(b)} \\ V^{(a)} \end{array} \right|_{x=0} - P^{(b)} \left| \begin{array}{c} V^{(a)} \\ V^{(b)} \end{array} \right|_{x=0} & -P^{(a)} \left| \begin{array}{c} P^{(b)} \\ V^{(a)} \end{array} \right|_{x=0} + P^{(b)} \left| \begin{array}{c} P^{(a)} \\ V^{(b)} \end{array} \right|_{x=0} \\ V^{(a)} \left| \begin{array}{c} V^{(b)} \\ V^{(a)} \end{array} \right|_{x=0} - V^{(b)} \left| \begin{array}{c} V^{(a)} \\ V^{(b)} \end{array} \right|_{x=0} & -P^{(b)} \left| \begin{array}{c} V^{(a)} \\ V^{(b)} \end{array} \right|_{x=0} + P^{(a)} \left| \begin{array}{c} V^{(b)} \\ V^{(a)} \end{array} \right|_{x=0} \end{bmatrix}. \quad (2.11)$$

The resulting sound pressures and particle velocities at the front and back of the sample result in (Kunio et al., 2009)

$$\begin{aligned} P\Big|_{x=0} &= 1 + R \\ P\Big|_{x=d} &= Te^{-jkd} \\ V\Big|_{x=0} &= \frac{1 - R}{\rho_0 c} \\ V\Big|_{x=d} &= \frac{Te^{-jkd}}{\rho_0 c}. \end{aligned} \quad (2.12)$$

Defining the reflection and transmission coefficients R and T as $R = \frac{B}{A}$ and $T = \frac{C}{A}$ and inserting Eq. 2.12 in Eq. 2.10, the reflection and transmission coefficients can be written as functions of the transmission matrix elements as (Kunio et al., 2009)

$$\begin{aligned} T_a &= \frac{2e^{jkd}}{T_{11} + \frac{T_{12}}{\rho_0 c} + \rho_0 c T_{21} + T_{22}} \\ R_a &= \frac{T_{11} + \frac{T_{12}}{\rho_0 c} - \rho_0 c T_{21} - T_{22}}{T_{11} + \frac{T_{12}}{\rho_0 c} + \rho_0 c T_{21} + T_{22}} \end{aligned} \quad (2.13)$$

and the sound transmission loss (STL) is calculated as (Kunio et al., 2009)

$$STL_n = 20 \log_{10} \left| \frac{1}{T_a} \right|. \quad (2.14)$$

Besides the transmission loss, the sound absorption coefficient can be extracted from the transmission matrix. When measuring the absorption coefficient with the two-microphone method, the sample is mounted at the end of the tube in front of a hard termination. This situation is simulated by applying a zero particle velocity condition of $V\Big|_{x=d} = 0$ at $x = d$. The reflection coefficient for a hard termination R_h is calculated as (Kunio et al., 2009)

$$R_h = \frac{T_{11} - \rho_0 c T_{21}}{T_{11} + \rho_0 c T_{21}} \quad (2.15)$$

and the absorption coefficient is given by (Kunio et al., 2009)

$$\alpha_h = 1 - \left| R_h \right|^2. \quad (2.16)$$

For example, Al-Zubi et al. used an acoustic impedance tube in the experiments with two microphones for determining the absorption coefficients of the test specimens (see Fig. 2.17a). (Al-Zubi et al., 2013) Similarly, Liu et al. measured the sound transmission of the prototype shown in Fig. 2.8 by means of an acoustic impedance measuring tube (2 microphone method) in the range from 250 Hz to about 1600 Hz. (Liu et al., 2000)

Guild et al., for instance, measured the magnitude and phase of reflection and transmission

coefficients of their prototype up to 6400 Hz by means of a sound transmission tube with four microphones. (Guild et al., 2018) Chen et al. analyzed experimental collected data for verifying the effective mass density of the prototype. They measured the amplitudes and phase curves of transmission and reflection by means of a transmission tube with four microphones using the transfer function method (see Fig. 2.17b). (H. Chen et al., 2013) Since in the present work the absorption coefficients are measured using an acoustic impedance tube, reference is made to the description of the measuring instrument in Chap. 4.

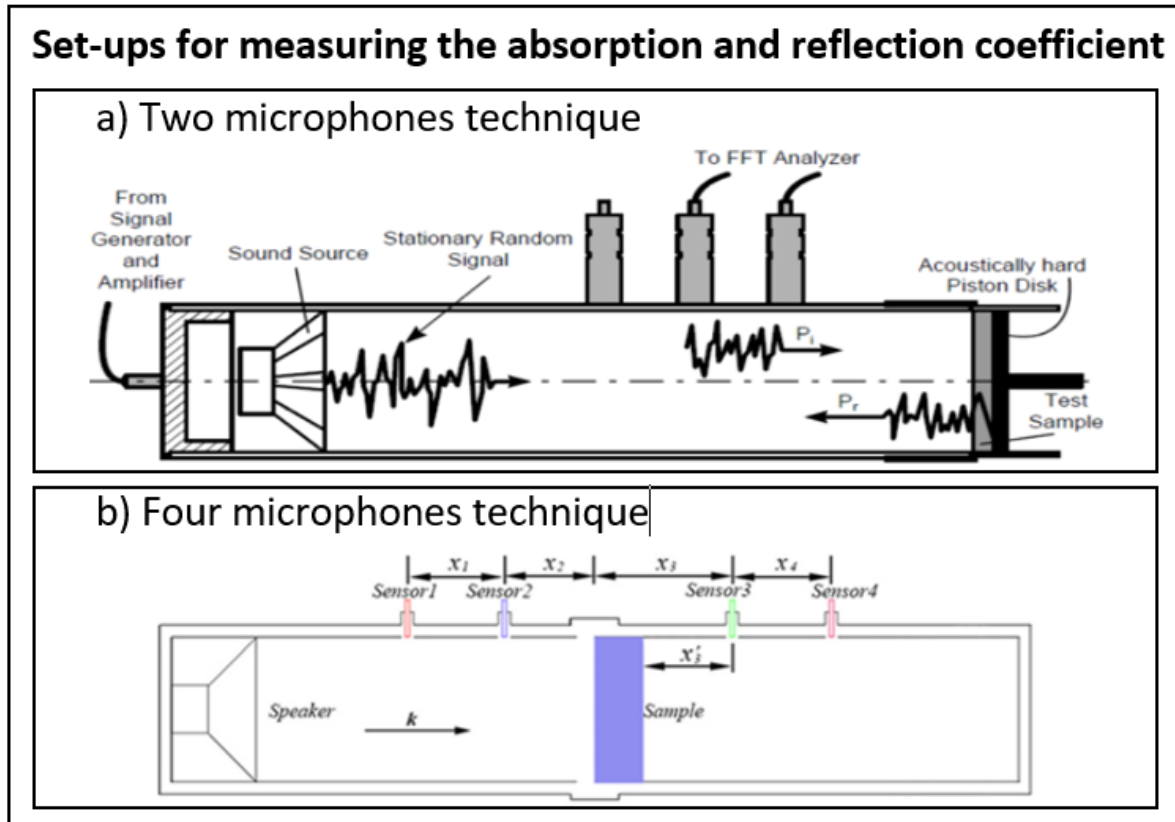


Figure 2.17: Set-up for measuring the absorption and reflection coefficient
(Al-Zubi et al., 2013) (H. Chen et al., 2013)

Speaker and microphone - sound transmission loss

Wang et al. designed a prototype consisting of a supporting frame to which a thin plate consisting of 484 (22 × 22) rectangular unit cells was glued. They determined the transmission loss of their prototype according to SAE J1400 by means of a measurement set-up consisting of a sound source chamber and a semi-anechoic chamber (see Fig. 2.18). The AMM plate was screwed to the sound source chamber, which was made of composite panels and sealed with sealing paper, clay and sound-absorbing cotton. A noise generator produced white noise which was radiated into the room from a loudspeaker located in the sound source room. The sound pressures in both rooms were measured simultaneously with three microphones, of which two were located in the sound source room and one in the semi-anechoic chamber. The transmission loss is given by Eq. 2.16 from the ratio of incident sound energy W_{in} and

transmitted sound energy W_{out} . (Wang, Chen, Zhou, Chen, & Ma, 2019)

$$STL = 10 \log\left(\frac{W_{in}}{W_{out}}\right) \quad (2.17)$$

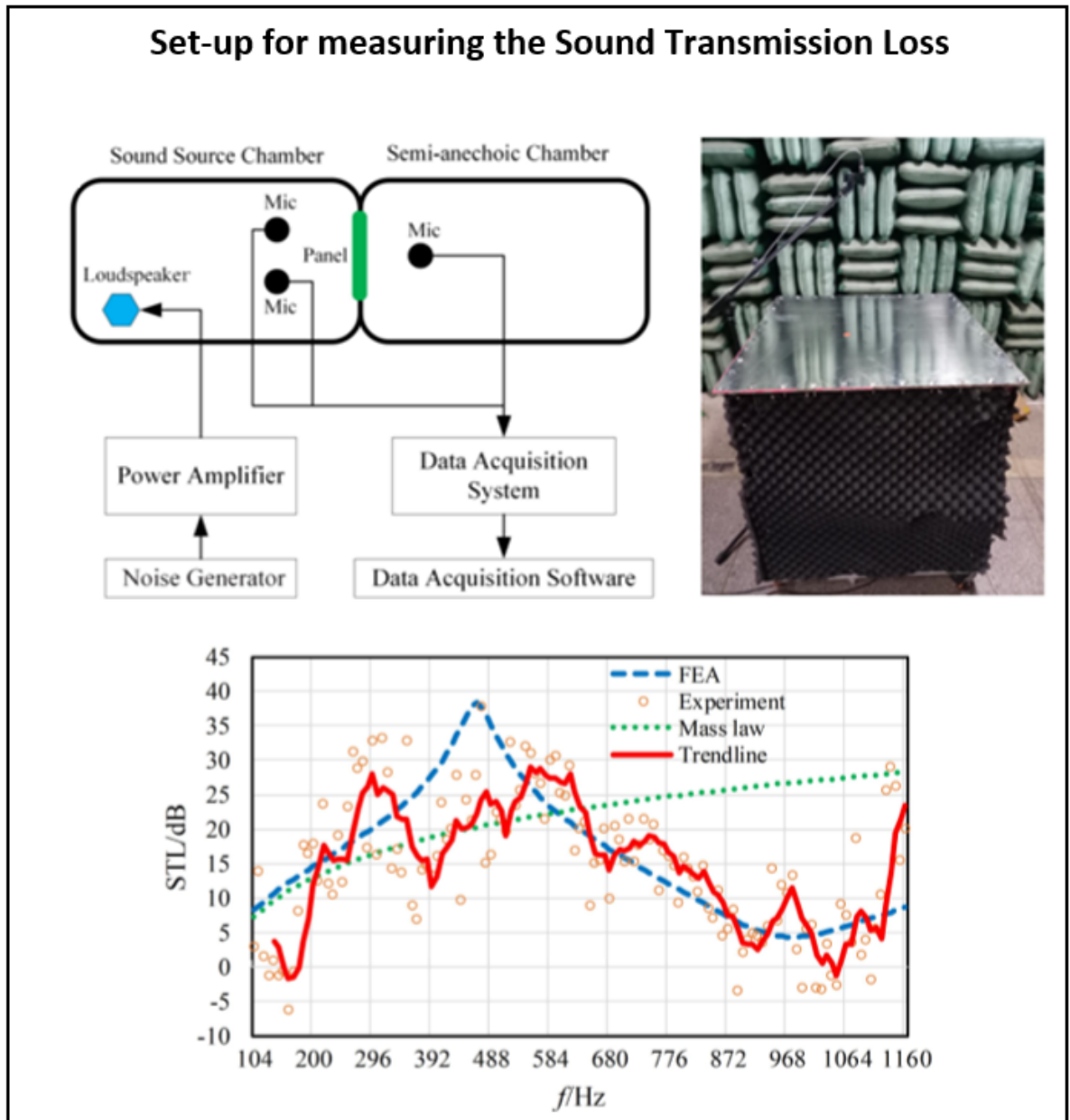


Figure 2.18: Set-up for measuring the sound transmission loss
(Wang et al., 2019)

Speaker and microphone - sub-wavelength imaging

Chen et al. determined the sub-wavelength imaging of their prototypes at 1630 Hz. For that purpose, they packed sound-absorbing material around the demonstrator to eliminate the diffraction of acoustic waves. They placed an aluminum screen between the test specimen

and a loudspeaker emitting continuous sinusoidal waves. The one-dimensional acoustic field distribution was detected with a microphone, that was fixed on the other side of the metamaterial (see Fig. 2.19a). As a result, they obtained the normalized pressure amplitudes of the metamaterial with three transfer peaks compared to the sponge matrix with only one peak over the wave vector. (H. Chen et al., 2013)

In turn, Dong et al. built a measurement set up as presented in Fig. 2.19b. It consisted of acoustic absorbing foams to avoid reflections, a loadspeaker, that emits waves and a microphone measuring the acoustic pressure. They placed their metamaterial prototype in this apparatus to experimentally demonstrate the broadband sub-wavelength imaging in a range from 1700 Hz to 2500 Hz by analyzing the measured pressures using the fourier transformation. (Dong et al., 2019)

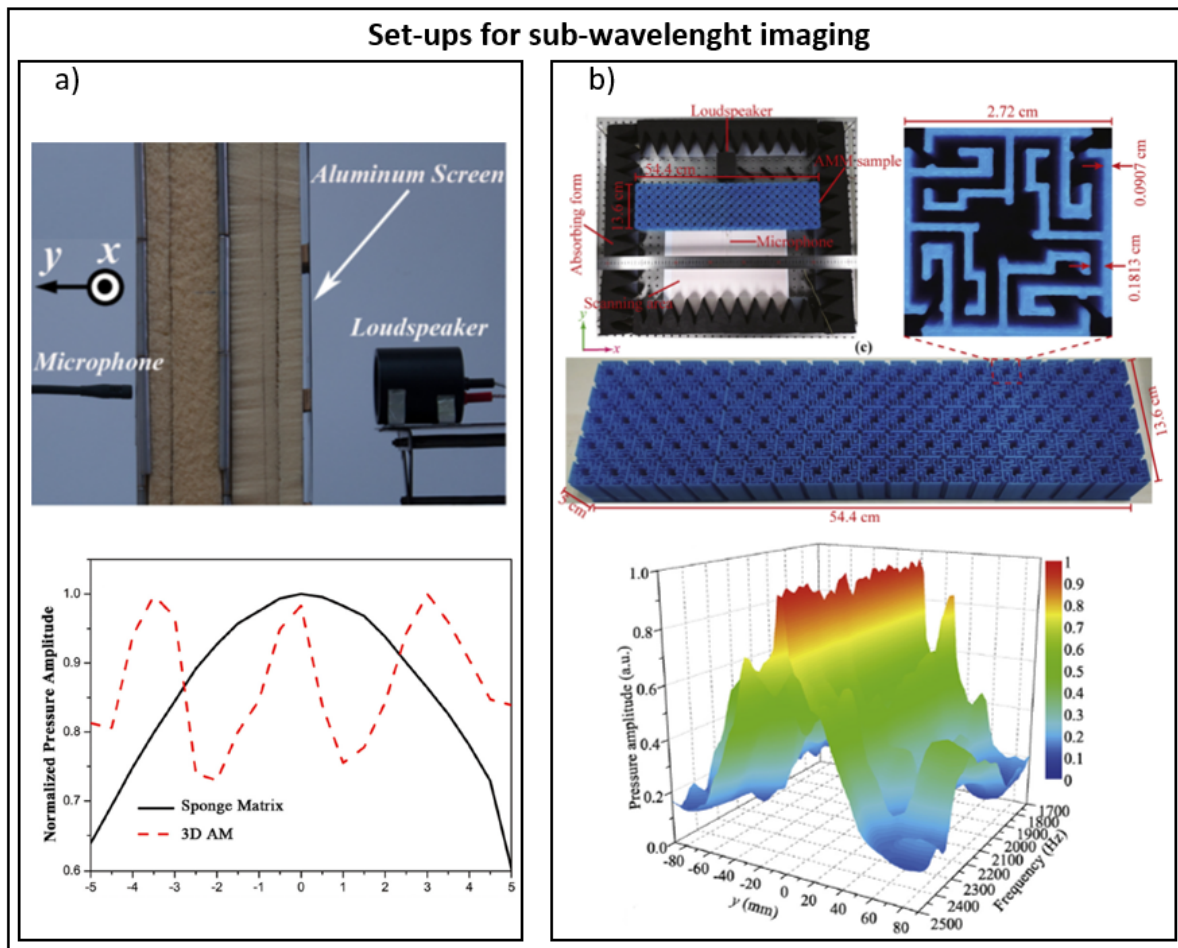


Figure 2.19: Set-up for sub-wavelength imaging
(H. Chen et al., 2013) (Dong et al., 2019)

Speaker and microphone - insertion loss

To determine the insertion loss (IL) of the constructed prototypes, Claeys et al. fixed a small loudspeaker on a wooden plate, that in turn was fixed on an iron support. To cover the cable of the speaker, acting as a point source of noise, a piece of fabric was placed between the loudspeaker and the wooden plate, which perfectly reflected sound. Moreover a trim of the

same size as the enclosure was added to reflect the trim on the wooden plate. To determine the insertion loss, each cube was placed over the loudspeaker and the acoustic power on each side of the cube was measured using a microphone (see Fig. 2.20). The insertion loss results from the ratio of the acoustic power emitted by the loudspeaker in the case without enclosure P_{without} to the acoustic power obtained with a prototype placed above the speaker $P_{\text{with enclosure}}$ according to Eq. 2.18. (Claeys et al., 2016)

$$IL = 10 \log_{10} \left(\frac{P_{\text{without}}}{P_{\text{with}}} \right) \quad (2.18)$$

As a result, one obtaines the insertion loss, which is a dimensionless quantity, represented over the frequency in hertz.

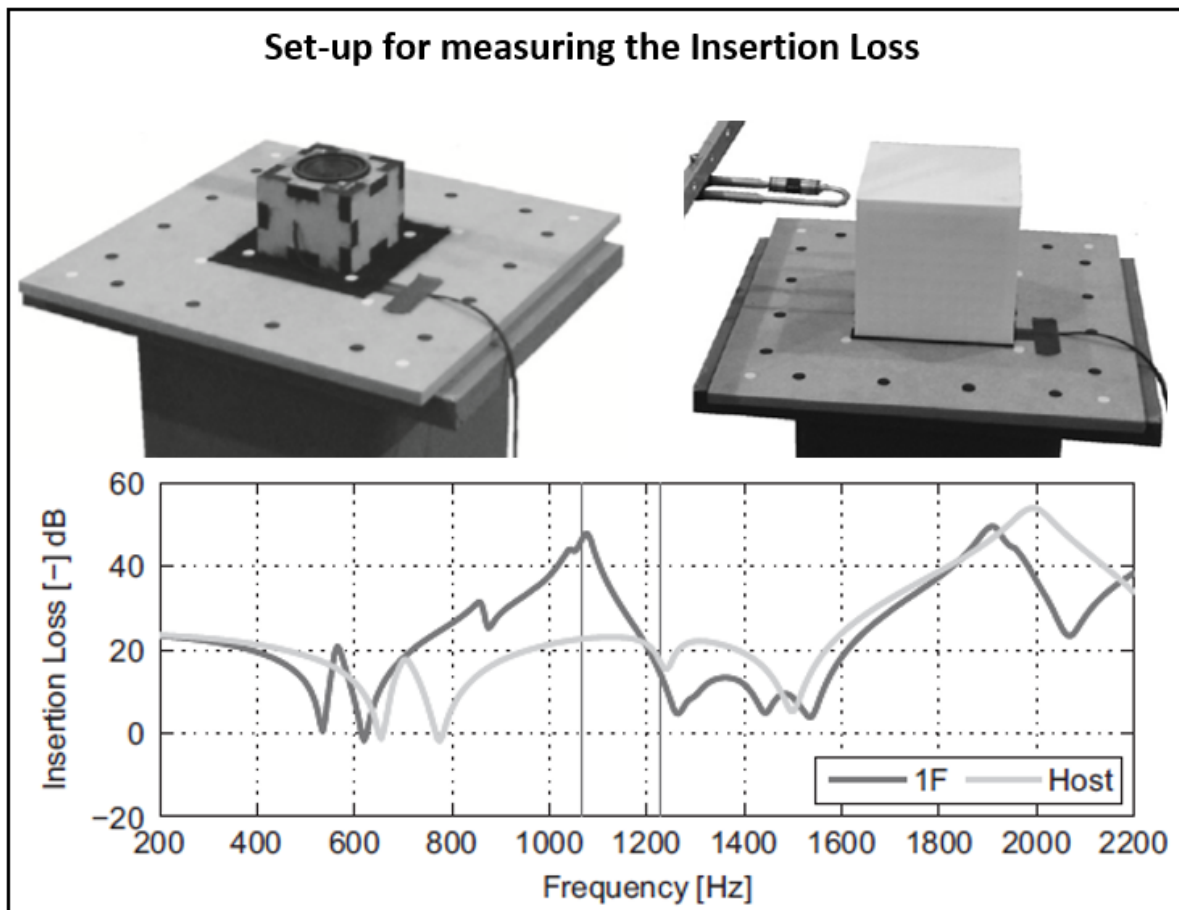


Figure 2.20: Set-up for measuring the insertion loss
(Claeys et al., 2016)

3 Prototyping of metamaterial structures

In order to analyze the effectiveness of an acoustic metamaterial on sound insulation, different prototypes are built and their influence on noise reduction is investigated experimentally. In the present case, sound that propagates in one spatial direction is attenuated by a cylindrical plate and the insulation of three-dimensional propagating sound waves is realized by an acoustic enclosure. To ensure a proper comparison of the potential of the metamaterial in noise reduction, all demonstrators are manufactured as one part. For this purpose, the prototypes are built by means of the additive manufacturing technology stereolithography (SLA). Thus, influences like screws, welding seams or adhesive joints, which might have a distorting effect on the noise attenuation are excluded. (Claeys et al., 2016)

3.1 Concept development of acoustic metamaterials

For the development of an acoustic metamaterial with resonance-based stop bands, two demonstrators from acoustic metamaterial research are used as templates. Similar to the structure developed by Amado-Mendes et al. (see Fig. 3.1b), in the present work a panel into which cavities with embedded resonators are inserted are created. Fig. 3.1a illustrates a hand-drawn sketch of the created panel. The voids act as a host structure in which incident waves of a certain frequency can propagate. The resonant structures absorb energy when the frequencies of the incident waves coincide with the natural frequencies of the resonators.

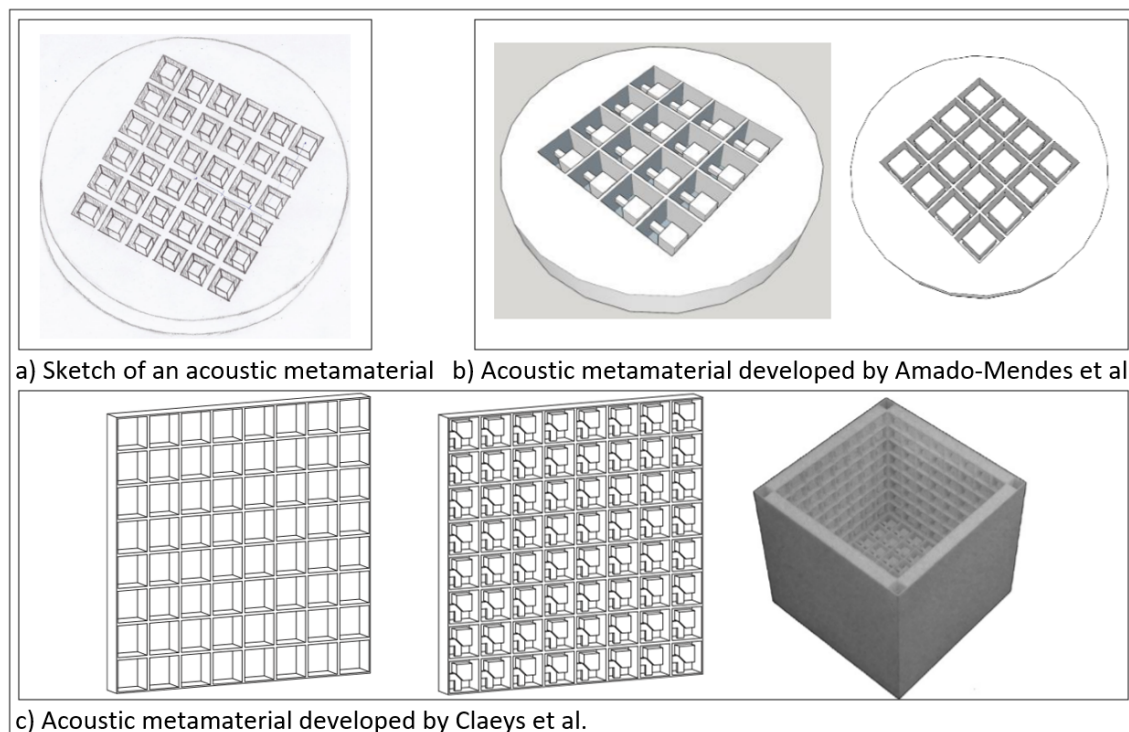


*Figure 3.1: Hand-drawn sketch of an acoustic metamaterial
 (Amado-Mendes et al., 2018) (Claeys et al., 2016)*

Each resonator can be considered as a mass-spring system (see Fig. 3.2a). In this arrangement the effective mass m , the effective spring stiffness D and an external force $F(t)$ are related according to Eq. 3.1, where $x(t)$ describes the displacement. (Heinrich & Dufour, 2015)

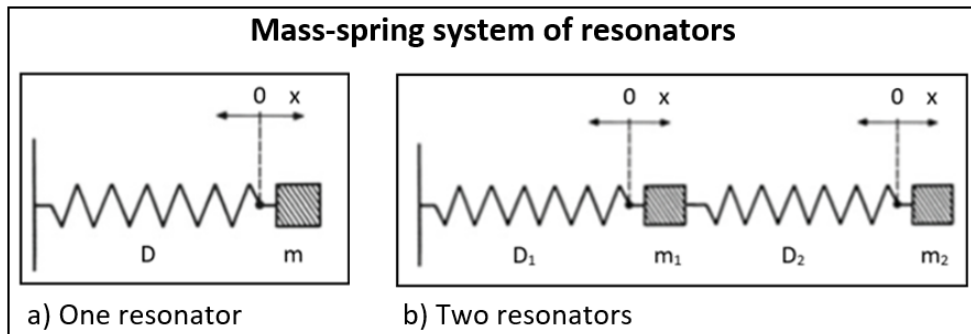


Figure 3.2: Mass-spring system of resonant structures
(Klages & Stuart, 2010)

For a balance of forces, the external excitation $F(t)$ assumes the value zero and the undamped angular frequency ω_0 can be derived. It describes the natural frequency of the resonator system, at which sound waves are absorbed (see Eq. 3.1). (Heinrich & Dufour, 2015)

$$\begin{aligned} m \cdot \ddot{x}(t) + D \cdot x(t) &= F(t) \\ m \cdot \ddot{x}(t) + D \cdot x(t) &= 0 \\ \rightarrow \omega_0 &= \sqrt{\frac{D}{m}} \end{aligned} \tag{3.1}$$

Whereas the acoustic metamaterial is generated on the basis of this literature example by Amado-Mendes et al., various parameters are changed to differentiate from this literature example. The selection of the plate geometry is motivated by the decision to use the acoustic impedance tube as a measuring instrument for recording the sound absorption coefficient.

The acoustic enclosure developed by Claeys et al. is used as a template for the concept generation of the three-dimensional prototype. Like the structure from this literature example shown in Fig. 3.1c, the created demonstrator in the present case consists of five side surfaces and is hollow inside. The individual side walls are divided into cells into which resonators are inserted. Designing the prototype as a cube open on one side allows the demonstrator to be placed over a sound source and the reduction of sound radiation to be measured.

3.2 CAD modeling

The models of the prototypes are created using SG-Library®, that was developed by the Chair of Micro Technology and Medical Device Technology at the Technical University of Munich led by Prof. Lüth. Solid Geometry Library Toolbox® (SG-Library®) is a Matlab toolbox for creating surface models for components, mechanisms and robots based on Matlab codes. Thereby, a geometric body is completely described by the total amount of its flat surfaces spanned by the corners of the body. The modeling of a body by planar surfaces is called Boundary Representation (BREP) and is used by default in additive manufacturing.

Advantages of SG-Library are the fast generation of three-dimensional models, which can be exported as STL files and imported directly into the 3D printer. In addition, the models can be further processed via an interface to Simscape Multibody and the PDE toolbox to perform shape optimization (CAO) and topology optimization (SKO). (Lueth, 2019) (Lueth, Irlinger, et al., 2013)

In the appendix under Sec. A1 all commands, which were used for the geometry generation are listed and commented out. It is necessary to consider, that the volume of the printed body expands during post-processing. Therefore, one reduces the diameter of the models by 0.10 mm and obtains a real diameter that is a few millimeters larger than the nominal dimension. The excess material is removed manually with sandpaper. Since the round base surface of the panel is only approximated and therefore not completely round, the shell surface exhibits slight unevenness. Furthermore, the base surface contains coarse defects, which stem from applied support structures for a safe printing process. As the unevenness of the floor surface caused by the supports is very large, the thickness of the model is not lowered but the extension of the material is deliberately accepted for the purpose of having enough excess material for smoothing out all asperities with emery paper. Likewise, when creating the acoustic enclosures, 0.10 mm of material is subtracted for each outer edge length to compensate for the material expansion and to create the prototype with the desired dimensions by finishing it with sand paper.

3.2.1 CAD modeling of the panel

A 16.00 mm thick plate with a diameter d of 40.00 mm and flat surfaces is used as a reference body for comparison with the metamaterial structures (see Fig. 3.3 and 3.4a).

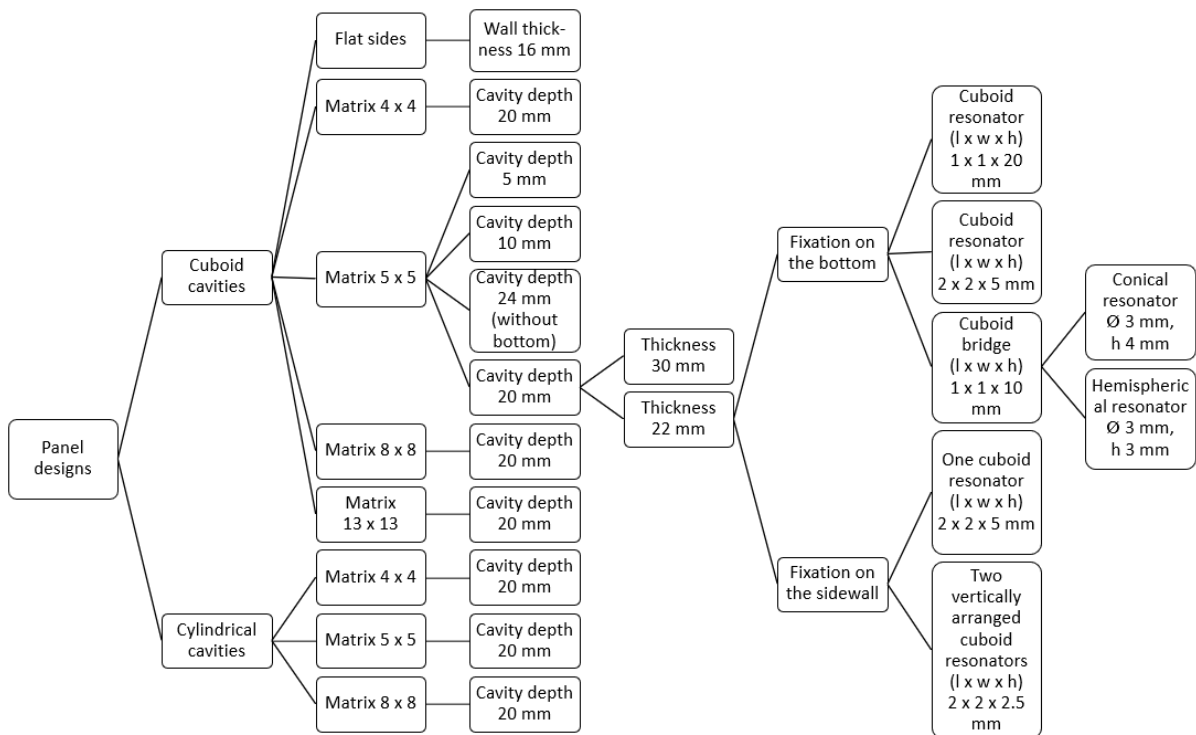


Figure 3.3: Designs of the panels - variated parameters

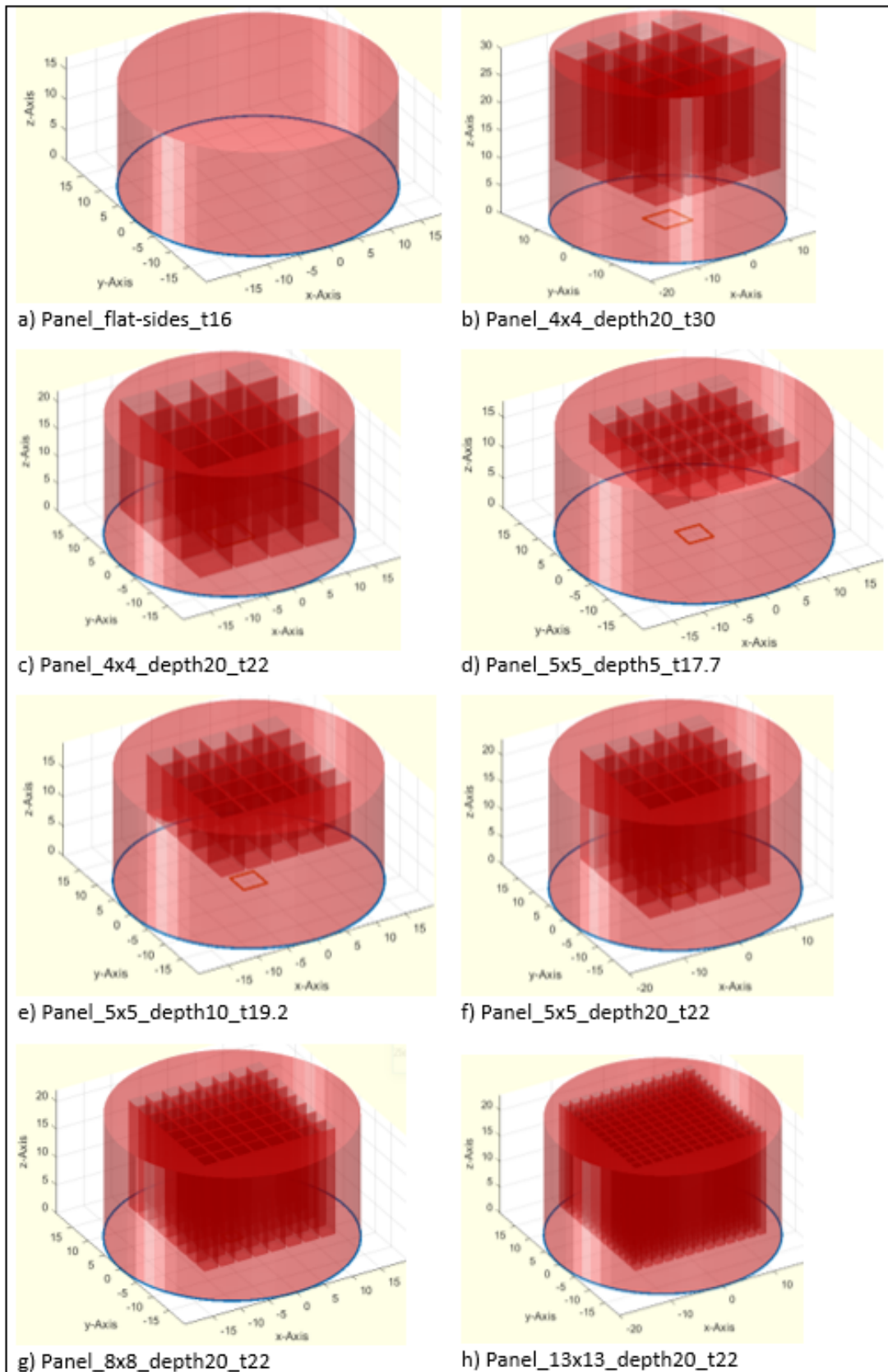


Figure 3.4: Panel designs - variation of cavity depth and geometry, grid size and number

The programming code to construct this geometric body is

```
SGofCPLcommand('c 40,h 16,write Panel_flat-sides_t16').
```

The programming code can be divided into individual commands. The function '*c 40*' creates a two-dimensional circle with a diameter of 40.00 mm, which is extruded up to a height of 16.00 mm in the vertical direction by the further command '*h 16*'. The addition '*write Panel_flat-sides_t16*' specifies the file name under which the STL file is to be saved.

3.2.2 CAD modeling of acoustic enclosure

In the three-dimensional case the base body is defined as an one open side cube with edge lengths *l* of 60.00 mm (see Fig. 3.5 and 3.6a) and a thickness *t* of 5.00 mm.

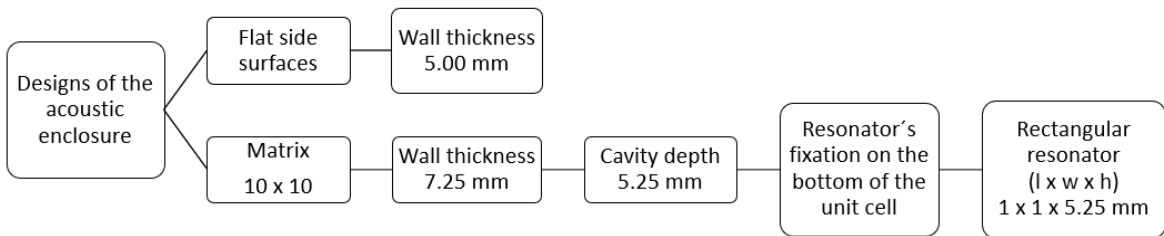


Figure 3.5: Designs of the acoustic enclosures - variated parameters

The programming code of the acoustic enclosure is defined as

```
SGofCPLcommand('b 60,h 5,dup,rotx 90,move 0 30 0,dupr 4,move 0 0 30,cat,
write Cube_flatsides_t5').
```

Using the command '*b 60,h 5*' a square area of side lengths 60.00 × 60.00 mm is created, which is extruded in vertical direction up to a height of 5.00 mm. By entering the command '*dup,rotx 90,move 0 30 0*', the created cuboid is duplicated, rotated by 90 ° and moved by 30.00 mm in the x-y plane. The cuboid is quadrupled again by the command '*dupr 4,move 0 0 30*', rotated by 90 ° each and shifted by 30.00 mm in the z-direction. By entering the command '*cat*' the individual cuboids are connected to form one object. The surface model is saved under the name *Cube_flatsides_t5* by formulating the command '*write Cube_flatsides_t5*'.

3.3 Parameter variation of metamaterial structures

Besides these base bodies for panels and acoustic enclosures, variations of both geometries are created. Since the sample thickness *t* depends on the volume or mass of the bodies, the

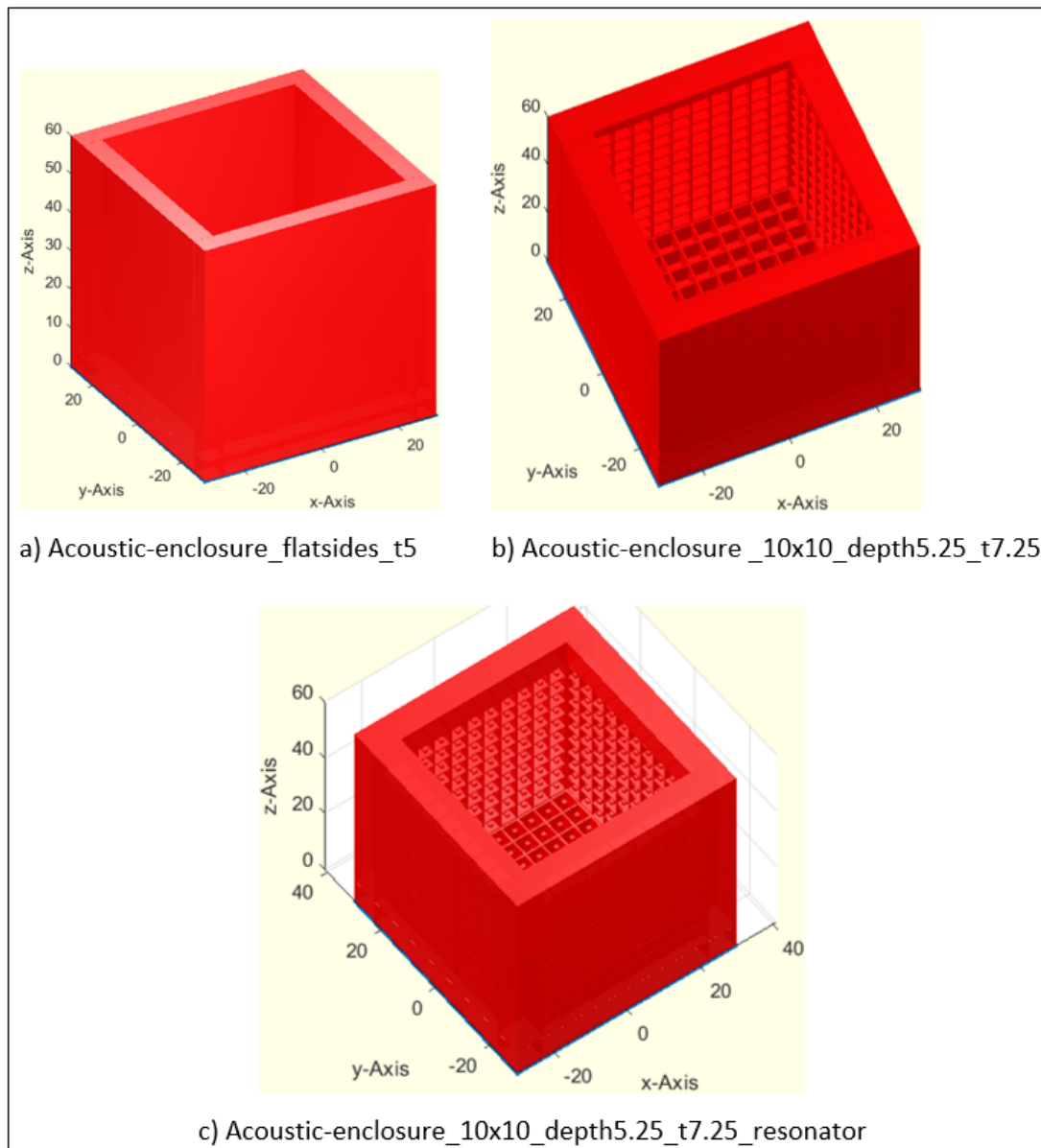


Figure 3.6: Designs of the acoustic enclosures

panels and one open side cubes are between 17.70 mm and 30.00 mm or between 5.00 mm and 7.25 mm thick. To ensure that investigations of the acoustic behavior of the samples only consider the influence of the geometry, the mass deviations between the models should be as small as possible. Furthermore, an increase in the weight of the prototype is to be avoided in the present investigation, since the aim is to achieve structures that are as light as possible.

3.3.1 Parameter variation of the panels

Besides the base panel, a host structure and resonators are added to the panel. Parameters like the thickness of the panel and of the bottom, the geometry, size and number of the voids as well as the design of embedded resonators are variated to create further panels.

- A panel of diameter 40.00 mm and thickness 30.00 mm with host structure is developed by inserting cuboid cavities (see Fig. 3.3 and 3.4b). The voids have a base area of 6.00×6.00 mm and a depth of 20.00 mm, so that a 10.00 mm thick soil under the cavities is created. A total of 16 voids are arranged in a 4×4 matrix in the x-y plane in the center of the plate with a distance between the cavity edges of 1.00 mm.

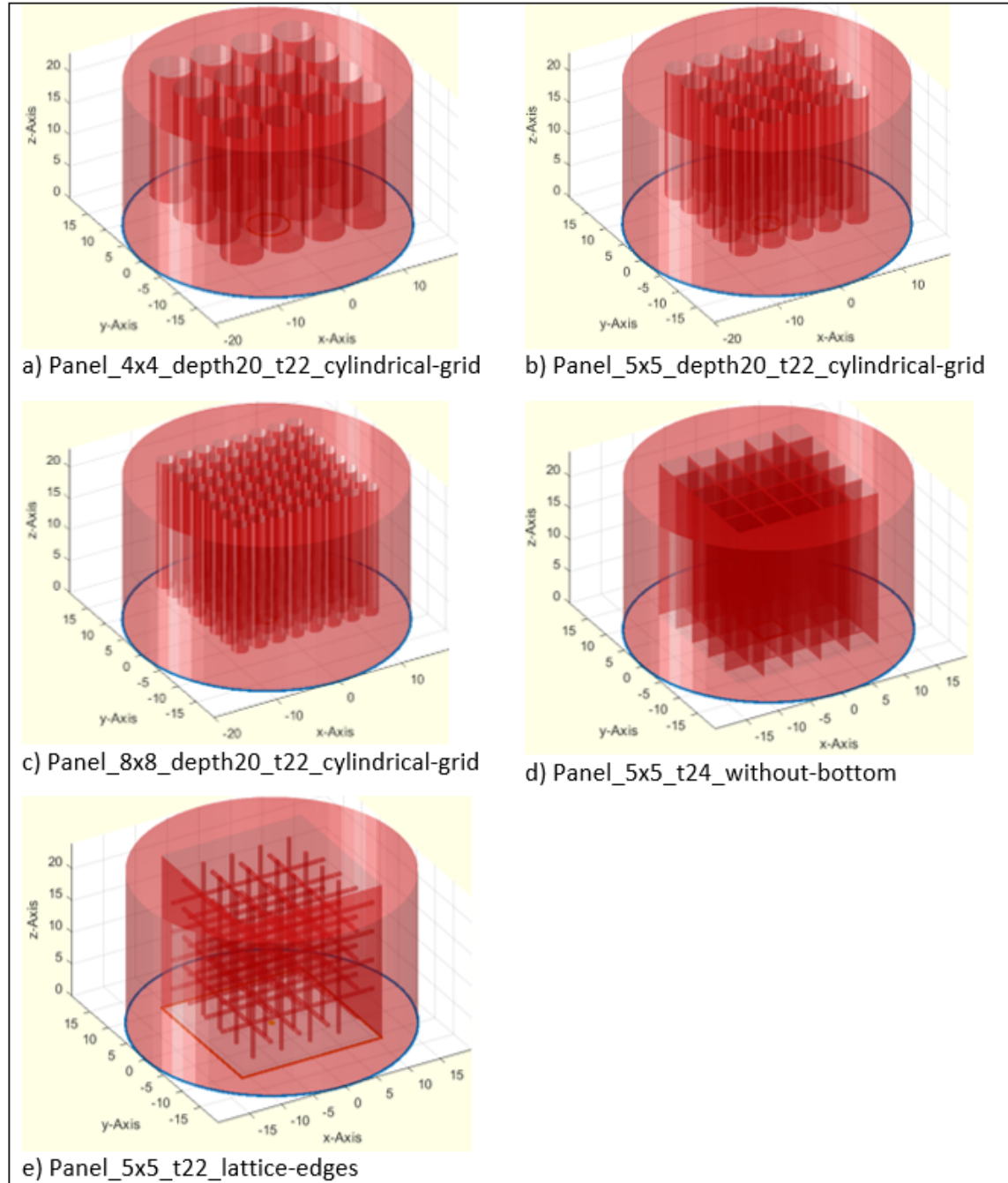


Figure 3.7: Panel designs - variation of cavity depth and geometry, grid size and number

- To experimentally determine the influence of cavity geometry, number and size on noise reduction, voids are designed as cuboids (see Fig. 3.4c-h) or cylinders (see Fig. 3.7a-c). The number of cavities arranged in one plane is 4×4 , 5×5 , 8×8 and 13×13 . Depending on the matrix size, the dimensions of the square bottom surfaces of the cavi-

ties are 6.00×6.00 mm for the 4×4 grid, 4.00×4.00 mm for the 5×5 grid, 2.50×2.50 mm for the 8×8 grid and 1.50×1.50 mm for the 13×13 grid.

Cylindrical voids measure 6.00 mm in diameter for the 4×4 grid, 4.00 mm in diameter for the 5×5 grid and 2.50 mm in diameter for the 8×8 grid. The cavities are separated from each other by webs of a wall thickness of 0.50 mm or one millimeter.

- In order to investigate the influence of cavity depth on sound propagation, hollow voids between five and 20.00 mm are formed. Basically, the depth of the cavities is less than the thickness of the panel, so that a thin bottom layer is formed on the lower surface of the panel. In the design presented in Fig. 3.7d, cavity depth and panel thickness are identical (24.00 mm) to measure the influence of a removed floor on the sound absorption in comparison to an added bottom.
- In addition to these cavity designs, an arrangement of bars with edge lengths of $0.50 \times 0.50 \times 22.00$ mm is inserted into the plate. This results in a $5 \times 5 \times 5$ grid structure as illustrated in Fig. 3.7e, that consists of bars only and has no closed surfaces. The cavity dimensions are then $4.00 \times 4.00 \times 4.00$ mm. This variant is used to measure the influence of three-dimensionally arranged cavities instead of continuous one-dimensional cavities on the sound reduction.

Furthermore, panels with resonators placed in the cavities are constructed. The bodies placed in the voids interact with air and cause local resonance-based band gaps. The resonator designs differ in terms of dimension, shape and fixation point to identify and compare their respective effectiveness in terms of noise reduction.

- Two rectangular resonator designs of the dimensions $1.00 \times 1.00 \times 20.00$ mm and $2.00 \times 2.00 \times 2.50$ mm respectively are created, that are attached centrally to the bottom of the voids (see Fig. 3.8a-b and 3.9a-b). The two variants are used to experimentally determine the influence of the geometry of the resonant structures on the absorption coefficients.
- In a further design, the influence of the resonator geometry is measured. For this purpose, a $1.00 \times 1.00 \times 10.00$ mm thin beam of cuboid shape is mounted centrally to the cavity floor. To the end of this bridge, a resonant body of conical form with a diameter of three millimeters and a height of four millimeters (see Fig. 3.8e and 3.9d) or of hemispherical shape with a diameter of three millimeters (see Fig. 3.8f and 3.9e) is attached.
- Furthermore, the effect of a $2.00 \times 2.00 \times 5.00$ mm cuboid fixed to the inner sides of the cavities at a height of 10 mm above the cavity floor is investigated. The resonator and panel are presented in Fig. 3.8c and 3.9b. By fixing the resonators to the side walls, the difference in sound reduction compared to the floor is measured.
- Besides one resonator, the influence of two resonators placed one behind the other with the same total mass as a single resonator is measured. In Fig. 3.9c two $2.00 \times 2.00 \times 2.50$ mm large rectangular bodies are illustrated, that are fixed to the inner sides of the cavities at a 10 mm distance from the cavity floor and at a spacing of 2.50 mm above each other (see Fig. 3.8d).

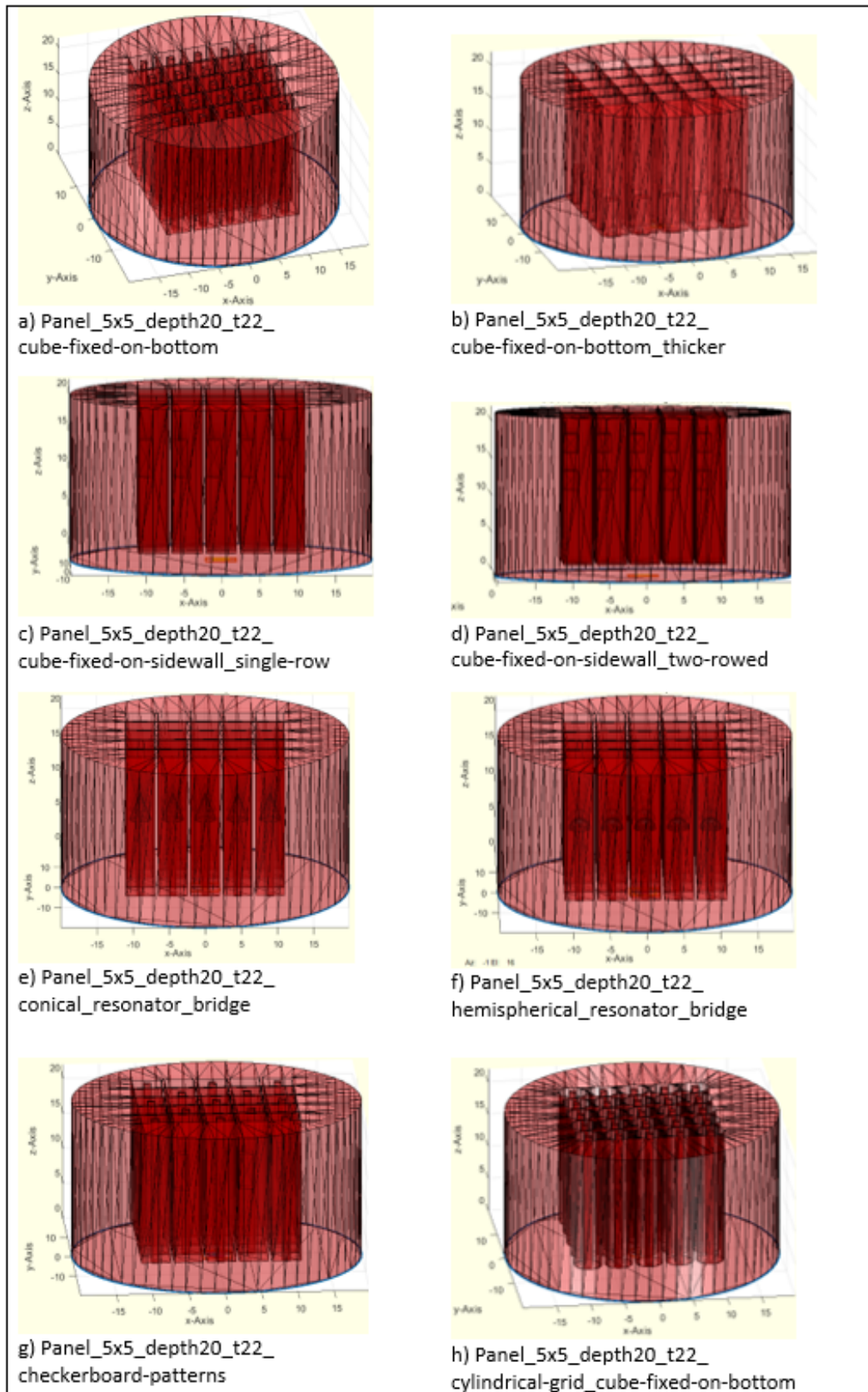


Figure 3.8: Panel designs - variation of the resonator design and fixation point

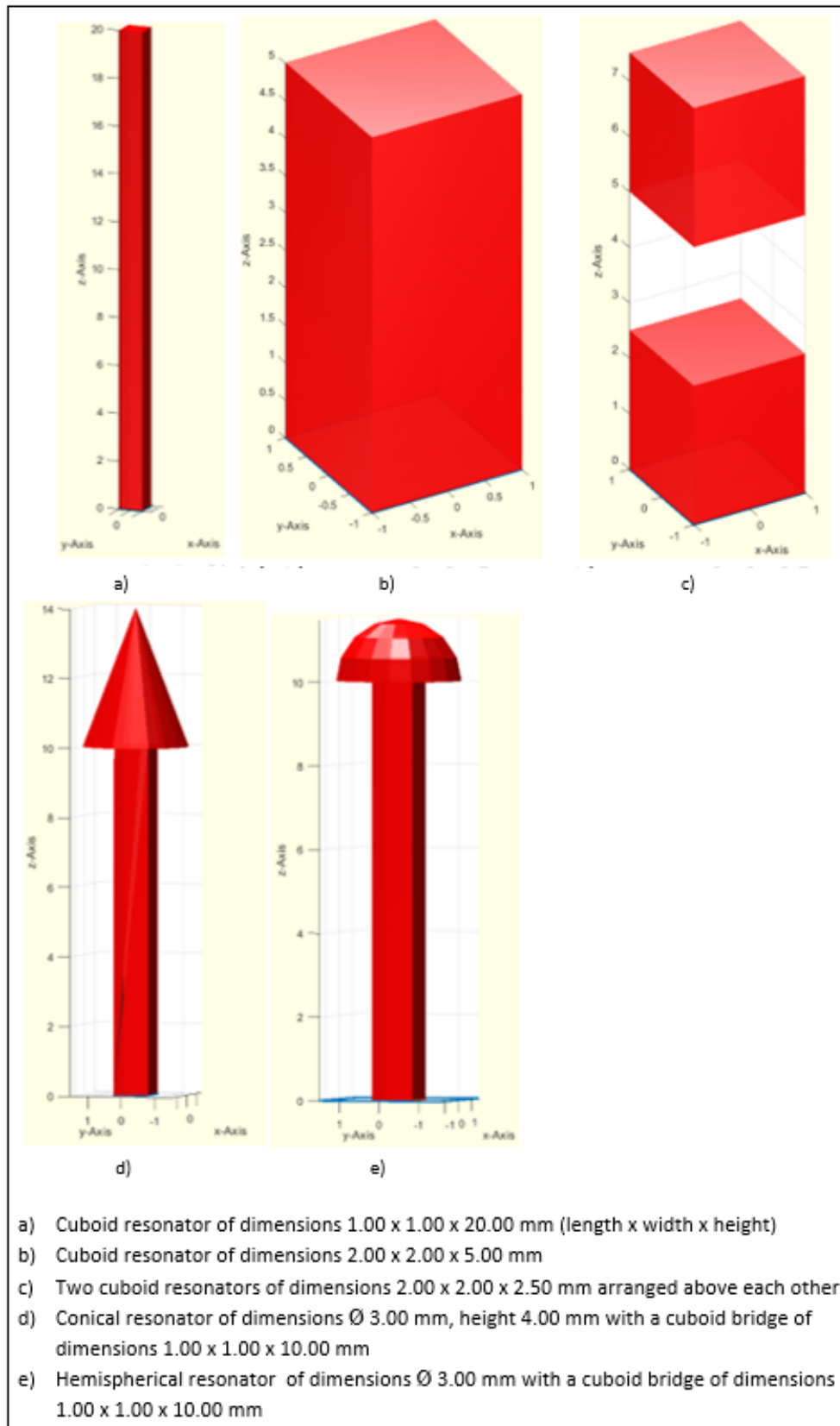


Figure 3.9: Resonant structures

- Moreover, rectangular resonators of the dimensions $1.00 \times 1.00 \times 20.00$ mm are inserted in cylindrical voids with a diameter of four millimeters (see Fig. 3.8h) to measure the difference in sound absorption compared to square cavities with the same inserted resonators.
- Fig. 3.8g shows a panel with cavities in which two different resonator geometries are embedded. Thereby the effect of a combination of the resonator variants presented in Fig. 3.8a and 3.8c on the sound absorption is to be investigated.

Besides these parameter variations of the panels, the influence of material properties on sound propagation is investigated. For that purpose, three versions of the panels are built from two different materials, that are tough and casting. Thus, a total of 21 plates are created, whose sound reduction potentials are investigated and compared.

3.3.2 Parameter variation of the acoustic enclosures

Besides a base version of the acoustic enclosure consisting of five cuboids of dimensions $60.00 \times 60.00 \times 5.00$ mm and flat surfaces, two additional prototypes are designed.

- In one variant, a host structure is embedded in the 7.25 mm thick side walls, so that each side surface is divided into 100 cells, arranged in a 10×10 matrix and designed as cuboid cavities. The voids measure $4.00 \times 4.00 \times 5.25$ mm and are separated from each other by 0.50 mm (see Fig. 3.6b).
- Fig. 3.6c presents a prototype, which basically equals that in Fig. 3.6b, but is additionally supplemented by resonators. The embedded resonant structures of geometry $1.00 \times 1.00 \times 5.25$ mm are fixed centrally to the bottom of the cells.

Thus, a total of three acoustic enclosures are developed, whose effectiveness in sound reduction are investigated and compared.

3.4 Prototyping of acoustic metamaterials

3.4.1 3D printer Prusa SL1[®]

The prototypes are built by means of additive manufacturing. Therefore a 3D printer of the type Prusa SL1[®] of the manufacturer Prusa Research[®] is used (see Fig. 3.10). It is a MSLA 3D printer, i.e. it works according to the principle of stereolithography. The "m" at the beginning means "masked". (PrusaResearch, 2019)

To generate a layer of the component, a built-in LCD print display shows a mask (shape) of the respective layer. An UV LED panel generates UV light that is transmitted through the mask and hits photosensitive liquid resins through the transparent bottom of the resin tank. The resins are composed of a core, photoinitiators, which initiate the solidifying process when reacting to UV light and additives, that improve the filaments properties or colour. The resin

hardens and the printed object adheres to the printing platform. After each layer created in this way, the printing platform moves upwards one layer width at a time so that there is room for another layer. The achievable quality of the demonstrators is limited by the resolution of the 3D printer. The Prusa SL1® can print layer heights from 0.01 mm to 0.10 mm, whereby the creation of a single layer takes six seconds, regardless of the object. Another constraint to be considered in prototyping is the installation space of the printer, which limits the maximum print volume to $120.00 \times 68.00 \times 150.00$ mm. (PrusaResearch, 2019)



Figure 3.10: 3D printer Prusa SL1®
(PrusaResearch, 2019)

In addition, the PrusaSlicer® software is required for "slicing" the models and a Curing and Washing Machine® (CW1®) from Prusa Research® (see Fig. 3.11) is used for post-processing the printed objects (washing / curing / drying). As it is not possible to print the models created in STL formats directly, they need to be converted into SL1 files, which contain printing instructions compatible with the Prusa SL1®. (PrusaResearch, 2019)

Data preprocessing – Prusa Slicer®

The slicer analyses the 3D model and cuts it into a number of separate thin layers. One places the converted file on a USB drive to import the data in the 3D printer. The 3D printer then creates objects layer by layer, beginning on the bottom and adding new layers on already printed ones. (PrusaResearch, 2019)

Since the object is generated layer by layer, there must be something to build upon. This can either be a layer or, as it is not possible to print layers mid-air, a support below it. Thus, it is hardly possible to print an object completely without support structures. Depending on the geometry of objects and their orientation in the installation space, supports are added to the model to achieve a good object positioning on the printing platform. In addition to the automatically added supports, PrusaSlicer® also offers the possibility to add additional supports manually. It is advisable to add more or thicker supports to a large object to ensure that the



Figure 3.11: Curing and Washing Machine®
(PrusaResearch, 2019)

printer delivers a perfect result. Otherwise it may detach due to its weight (see Fig. 3.12). On the other hand, even very small supports can leave marks on the surface of the object, and thus reduce the surface quality. Therefore it is highly recommended to add a pad, that is a small structure under the print and the base for supports, when printing structures with supports. (PrusaResearch, 2019)



Figure 3.12: Manufacturing defects due to incorrect pressure settings

In the present case, all objects are printed on a pad and, if required, support structures are placed between the bottom of the component and the pad. One can tilt the object to support the structure by reducing peeling force during layer separation process. Fig. 3.13 to 3.15 show two configurations of object placement. In the first variation, the upper side of the

object is parallel to the FEP film (bottom of the tank) and the underside of it is in parallel with the printing platform. In the second example, the objects are tilted at an angle of 45 °, which improves the utilization of the printing space and allows three objects to be printed simultaneously.

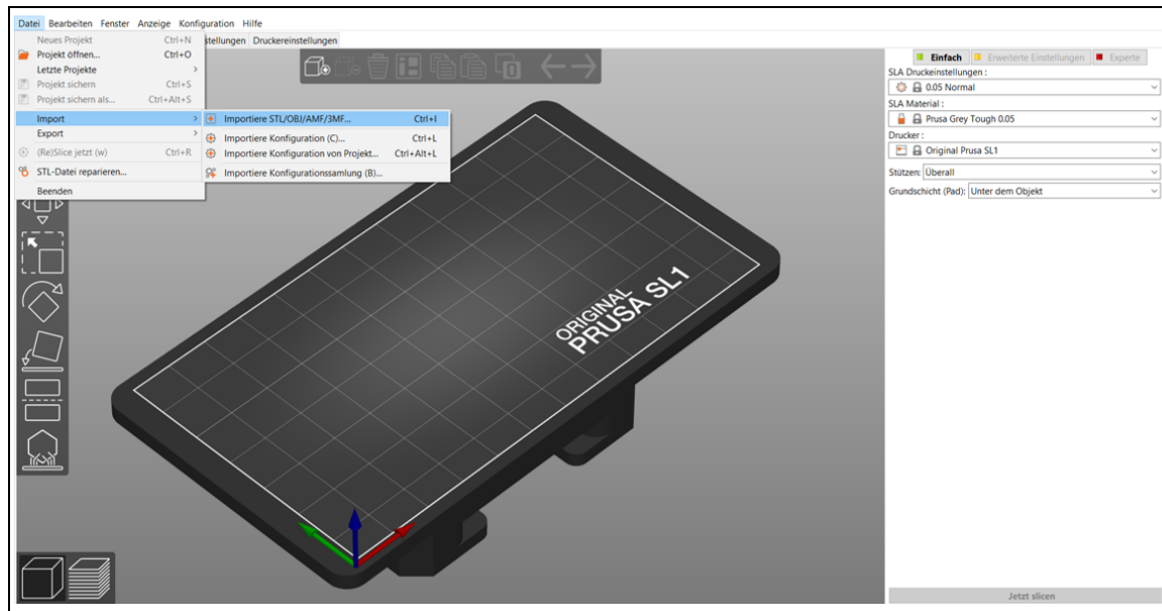


Figure 3.13: Prusa Slicer - Loading an object

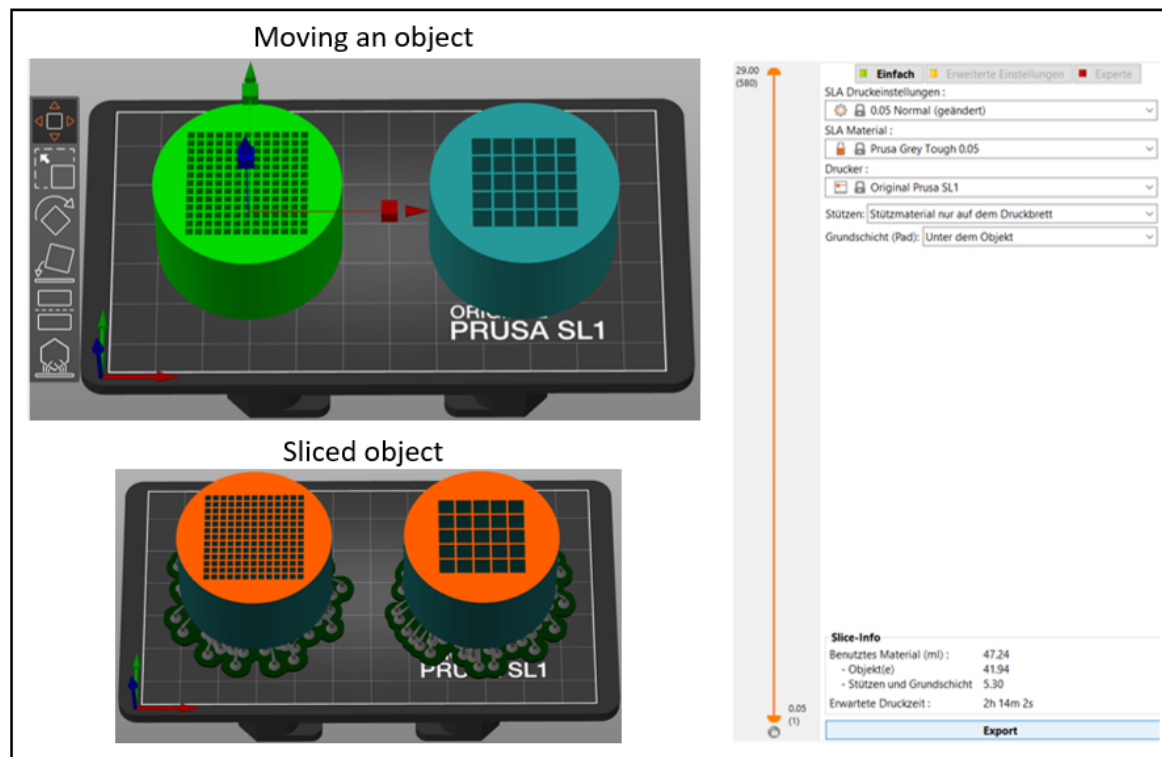


Figure 3.14: Prusa Slicer - Moving an object

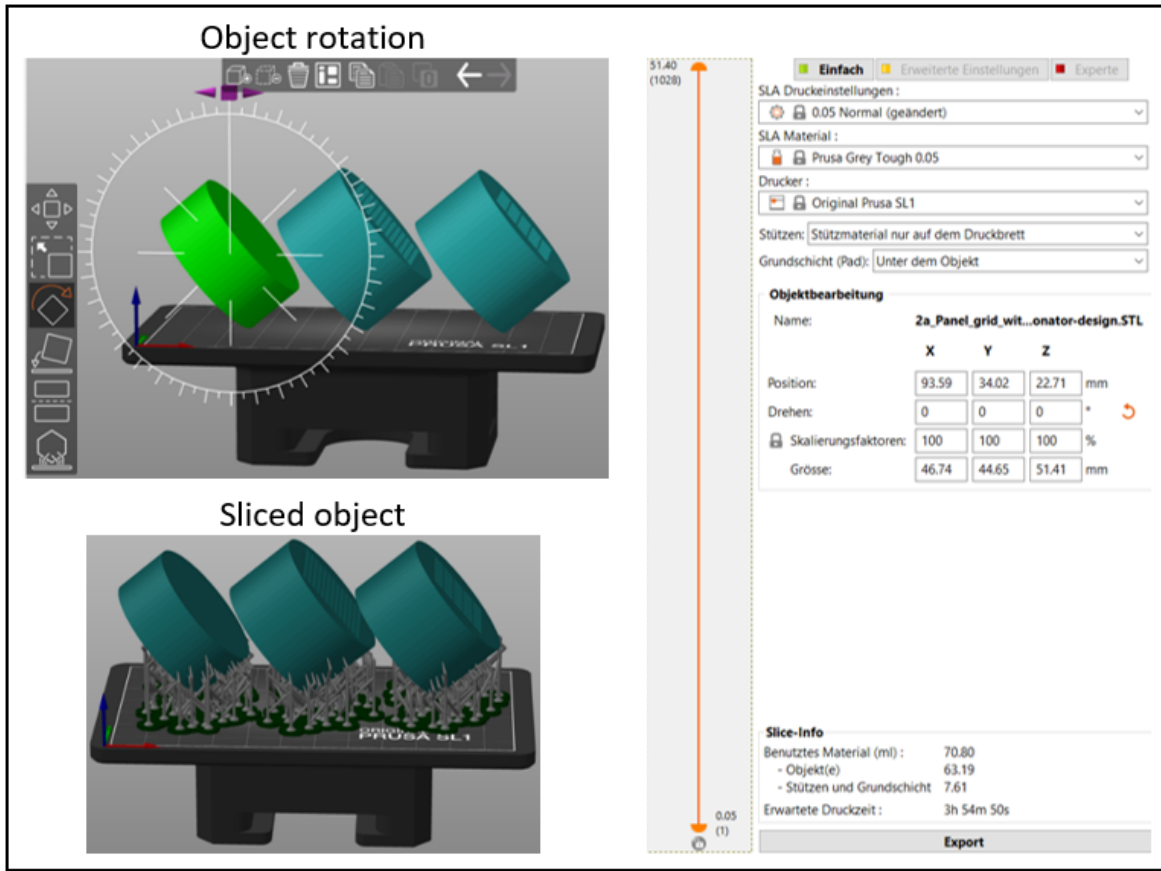


Figure 3.15: Prusa Slicer - Tilting an object

It is important to find a compromise between quality and safety of the printed object. The orientation also determines how long it takes to print it. Print time rises with increasing height of the object. One can change the object orientation arbitrarily by using commands from the toolbox until the object is green, which means the object is placed on the printing bed correctly and therefore printable. To save time, several objects can be placed on the print platform at once. Their layers are printed at the same speed and the objects are completed in the same time. (PrusaResearch, 2019)

Printing process – 3D printer Prusa SL1®

Before the printing process can be started, the printer must be calibrated by following the on-screen calibration wizard. The second step is to check whether the printing platform and the tank are clean. One also must make sure that the screws on the cantilever and the resin tank are slightly loosened as the platform moves during printing. Finally, the FEP film on the bottom of the tank is checked for cleanliness and the absence of any kind of damage. After a successful calibration, one can fill the resin in the tank. It should be noted that gloves should be worn when handling resin to avoid direct contact of the resin with the eyes and the skin. One pours the tank with resin until the marked maximum level indicator is reached (see Fig. 3.16). If the built-in level sensor registers a too high or low level of resin, the printing process is paused and an information message prompting to fill up the required amount of fluid is shown on the display. (PrusaResearch, 2019)



Figure 3.16: Resintank
(PrusaResearch, 2019)

In the next step, one connects the USB drive, on which a sliced project file is saved with the port on the printer and selects the model to print from the menu. When the lid is closed and the start button is pressed, the printer performs a quick self-test. During the printing process, a single layer is completed within six seconds regardless of the object geometry. In the present case, the number of layers is between 360 layers and 1028 layers for the panels or 1220 layers for the acoustic enclosures, resulting in a total printing time of between 01:25 hours to 03:55 hours and 04:38 hours, respectively. (PrusaResearch, 2019)

Postprocessing – Curing and Washing Machine[®](CW1[®])

Once the printing process is finished, the object can be removed from the printer. For that purpose, one opens the cover and loosens the knob on the top of the tower to remove the printing platform. The remaining, still liquid resin in the tank can be reused. To collect the resin, one releases the screws on the tank and decants the liquid by help of a funnel with inserted filter into the bottle. Finally, one carefully removes the object from the platform with a metal spatula (see Fig. 3.17a) and checks the print for defects such as missing parts, dents or inaccuracies. It is advisable to clean the printing platform thoroughly and immediately with isopropyl alcohol (IPA) after every print to avoid that drops of liquid resin solidify in sunlight and are therefore difficult to remove. (PrusaResearch, 2019)

As objects printed from liquid resins have a somewhat sticky and soft surface, they are washed in isopropyl alcohol, dried with air and cured with UV light in the Curing and Washing Machine[®] (CW1[®]) from Prusa Research[®]. Before finishing the objects by use of the CW1[®], it is advisable to properly clean all parts of the object by hand in a bath of isopropyl alcohol (see Fig. 3.17b). Moreover the objects should not be submerged in IPA for extended periods of time (hours or days) in order to avoid that the objects develop various cracks. The supports are dismantled immediately after printing with a sharp plier, as removing becomes more difficult after the material has cured (see Fig. 3.17c). (PrusaResearch, 2019)

After removing the support structures, one puts the objects into the tank, which includes isopropyl alcohol. The tank is placed in the holder system of the Curing and Washing Machine[®] and after closing the lid, the cleaning process is started (see Fig. 3.17d). After three minutes of washing, the tank is removed and the objects are taken out of the bath of isopropyl alcohol. Then one puts the objects directly on the round base plate of the Curing and Washing Machine[®], which has a pitted silver surface and closes the lid (see Fig. 3.17e). Following

the washing process, the display automatically indicates the next process step for selection. The drying and curing steps at a temperature of almost 31 °C each take four minutes and are performed directly one after another. (PrusaResearch, 2019)

Although the objects are basically ready for use, the surfaces are additionally sanded off by hand using 120 grade grit-paper. In the simulation model, the surface of the prototype is only approximated to a cylindrical surface and is therefore not completely circular. Hence, the edges are rounded off by grinding. In addition, any unevenness in the base surface which is formed at the attachment points of the support structure is removed with sandpaper (see Fig. 3.17f).

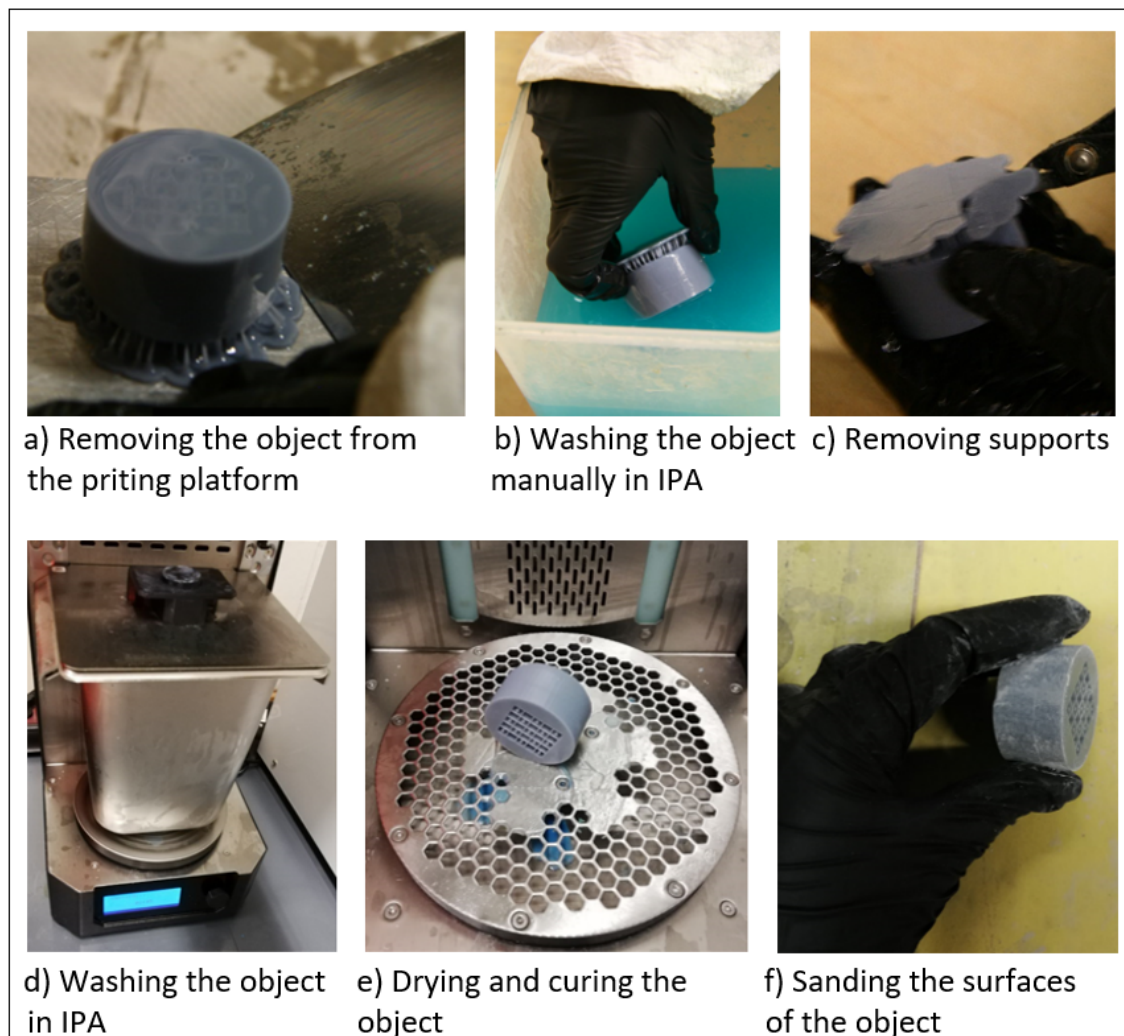


Figure 3.17: Post-processing an object

3.4.2 Practical aspects of the manufacturing process

In this paper, the demonstrators are built by means of additive manufacturing. In theory, stereolithography offers great design freedom compared to other additive manufacturing technologies. Indeed, the print quality of the 3D printer Prusa SL1® can not produce models with the desired accuracy. Contours with very small dimensions, e.g. narrow and deep cavities,

are created only inadequately, as liquid resin is hardly removed from the recesses. Fig. 3.18 presents plots of two panels with cuboid cavities in the x-z plane. Compared to the prototype with cavities with a square base area of 4.00×4.00 mm (see Fig. 3.18a), the cavities of the prototype in Fig. 3.18b ($2.50 \times 2.50 \times 20.00$ mm) are significantly narrower. Resin that remains on the inner side surfaces of the object after printing is less able to flow out of the narrower cavities. If residual liquid material can not be completely removed from the voids, it hardens. Thus, the depth of the cavities deviates from the actual nominal dimension and the object is distorted due to manufacturing inaccuracies.

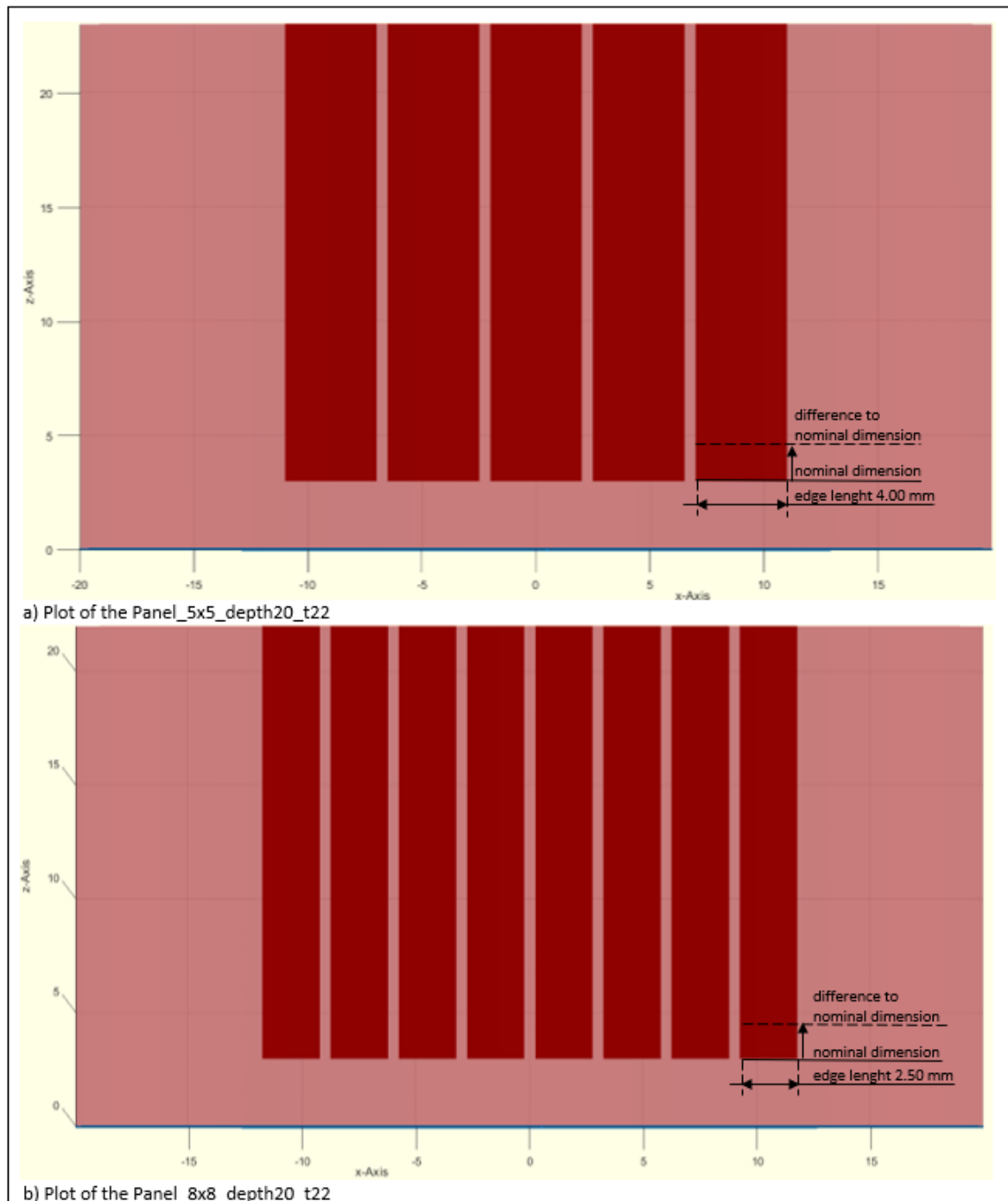


Figure 3.18: Manufacturing inaccuracies due to resin residues in cavities

Moreover, the manufacturing accuracy depends on the object orientation in the installation space and the use of support structures. To save time and print multiple objects simultaneously, the models can be tilted. However, this can lead to warping of the components. If, in addition, supports are added, the surface becomes uneven at the fixation point. If too few or too thin support structures depending on the geometry and mass of the object are used, the printing could fail completely. Especially with regard to supports, safety and surface quality must be carefully weighed up.

Besides the printing process, the accuracy of the prototypes is influenced by the post-processing. Since the objects are dried and cured after printing, the material expands by slightly less than five percent. This material strain must be taken into account in the manufacturing process, either by reducing the model by the factor mentioned or by removing the excess material after manufacture. Furthermore, it must be considered that the surfaces of the demonstrators were not ground, which led to further inaccuracies in the collection of measurement data.

Due to these deficiencies, the Prusa SL1® may not be the most suitable 3D printer for producing bodies with defined geometric properties. For resonance-based metamaterials, however, precisely this characteristic is a decisive criterion.

4 Experimental measurement of the panels

After designing and manufacturing the individual demonstrators one can define and install the test set-up to determine experimentally the influence of the prototypes on the acoustic wave propagation. The absorption coefficients α are determined for investigating the sound reduction by the panel designs.

4.1 Determination of the sound absorption coefficient of panel designs in the acoustic impedance tube according to DIN EN ISO 10534-2

4.1.1 Structure of the acoustic impedance tube

In the present paper, the AED 1000 - AcoustiTube Type 1[®] with the corresponding analysis software AED 1001[®] from Gesellschaft für Akustikforschung Dresden mbH[®] is used for determining the sound absorption coefficient of a material under laboratory conditions according DIN EN ISO 10534-2. The tube has an inner diameter of 40.00 mm and can be used for measurements in a frequency range from 100.00 Hz to 4950.00 Hz. The measurable frequency range is divided into a low-frequency (HF) and a high-frequency (HF) range. To measure the absorption coefficients for low frequencies from 100.00 Hz to 881.25 Hz, two microphones are placed in the outer two connection points Mic. 1 and Mic.3 of the tube between the test specimen and the loudspeaker. To investigate the absorption of high frequencies from 556.25 Hz to 4950.00 Hz, the microphones are mounted at a smaller spacing in the attachment points Mic. 2 and Mic.3 (see Fig. 4.1). In each case, a venting plug is inserted into the connection point at which no microphone is positioned. (AED, 2019)

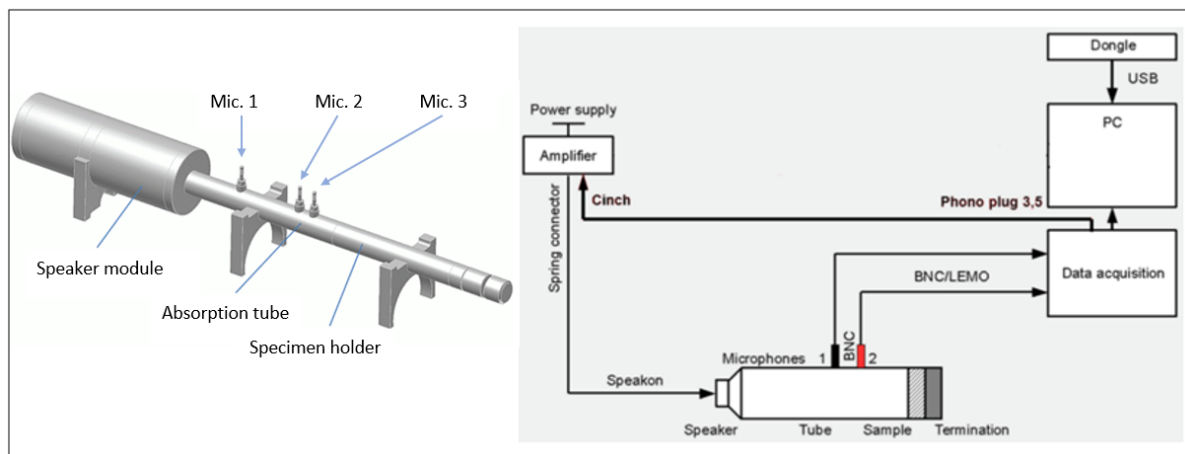


Figure 4.1: Structure of the AED 1000 - AcoustiTube Type 1[®]
(AED, n.d.)

The microphones of type 1/4", BNC (female), Kl. 1 can detect sound pressures in the frequency range from 20.00 Hz to 20.00 kHz and are connected with simultaneously sampled analog input channels of the data acquisition module IEPE conditioning module via BNC connections. The IEPE conditioning module is also connected to the amplifier via a cinch

connection to transmit information about the signal amplification. The processed data is transferred to a computer via USB interfaces. (AED, 2019)

4.1.2 Working steps

As presented in Fig. 4.2, there are six basic steps in taking measurements with the AED 1000 - AcoustiTube Type 1®.

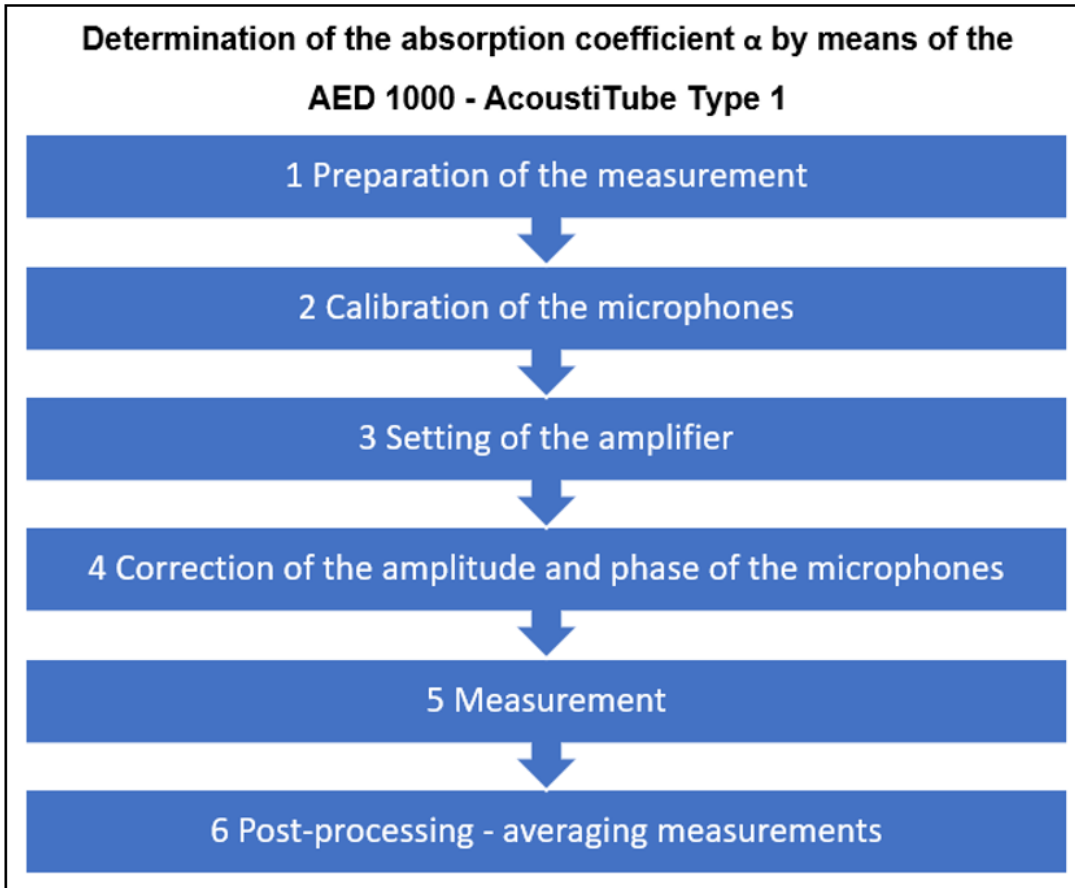


Figure 4.2: Determination of the absorption coefficient α with the AED 1000 - AcoustiTube Type 1®
(AED, n.d.)

1. Preparation of the measurement

Before starting measurements, one enters data on the environmental conditions, the measurement, the geometry of the acoustic impedance tube and the sampling rate into the analysis software. (AED, n.d.)

2. Calibration of the microphones

The next step is the calibration of the microphones. The microphones are plugged into a calibrator and the measured sound pressure level is averaged over a fixed time interval. The output values indicate the sound pressure level in decibel in the third-octave band with the center frequency of 1000 Hz and the gain factor in decibel. (AED, n.d.)

3. Setting of the amplifier

Another important task is the adjustment of the amplifier. Amplifier settings are selected so that a high signal-to-noise ratio is achieved, i.e. the difference between the sound pressure levels recorded by the microphones under test conditions and at background noise is as large as possible. For precise measurements, the signal-to-noise ratio should be at least 20 dB over the entire frequency range. For this purpose, the material sample is inserted into the sample holder and the sound pressure level of the background noise and the measurement signal are measured. (AED, n.d.)

4. Correction of the amplitude and phase of the microphones

Subsequently, an amplitude and phase correction of the microphones must be carried out. To compensate amplitude and phase differences in the frequency response between the microphones and thereby increase the accuracy of the measurement results, the transfer functions H'_{12} and H''_{12} between the two microphones are measured. The first measurement is performed with reversed microphone positions (interchanged microphone position), the second measurement is performed with the microphones placed at their actual measurement position. The channel correction H_c is calculated from the contributions of the transfer functions. (AED, n.d.)

5. Measurement

In order to measure the sound reflection factor and thus the sound absorption coefficient, one describes the measurement object to which the measured values are assigned by details on the measurement, the specimen, the impedance tube and the environmental conditions. While the measurement is running, the determined values are visualized in a diagram. One can select the values that are to be displayed and save the measurements in a database or files, e.g. PNG or XML file. (AED, n.d.)

6. Post-processing - averaging measurement data

After completion of the data acquisition, the measured values can be post-processed. If averaging over several measurement results is required, one can select those measurements which are to be considered in the mean value calculation from the measurements performed. Moreover, data of measured materials and specimens, contacts and projects can be managed in list format and loaded for comparison purposes. (AED, n.d.)

4.2 Analysis of the measurement data

4.2.1 Base panel and reference measurements

Fig. 4.3 illustrates the absorption coefficient α of a plate with a diameter of 40.00 mm and a thickness of 16.00 mm over a frequency range up to 5000 Hz. A panel with flat, smooth sides, whose outer dimensions exactly correspond to the inner diameter of the impedance tube, should totally reflect the incoming sound waves and the value of the absorption coefficient α should therefore be zero. As shown in the diagram, sound is absorbed in those areas where the absorption coefficients assume positive values and in fact, absorption coefficients of up to 22 % are detected.

There are three possible causes that could explain the curve. For one thing, sound could

be absorbed by the material properties. If a sound wave hits a flat surface that completely reflects waves due to its material properties, no energy is absorbed. According to Eq. 4.1, the absorption coefficients α assume zero. (DEGA, 2006)

$$\alpha = 1 - \rho \quad (4.1)$$

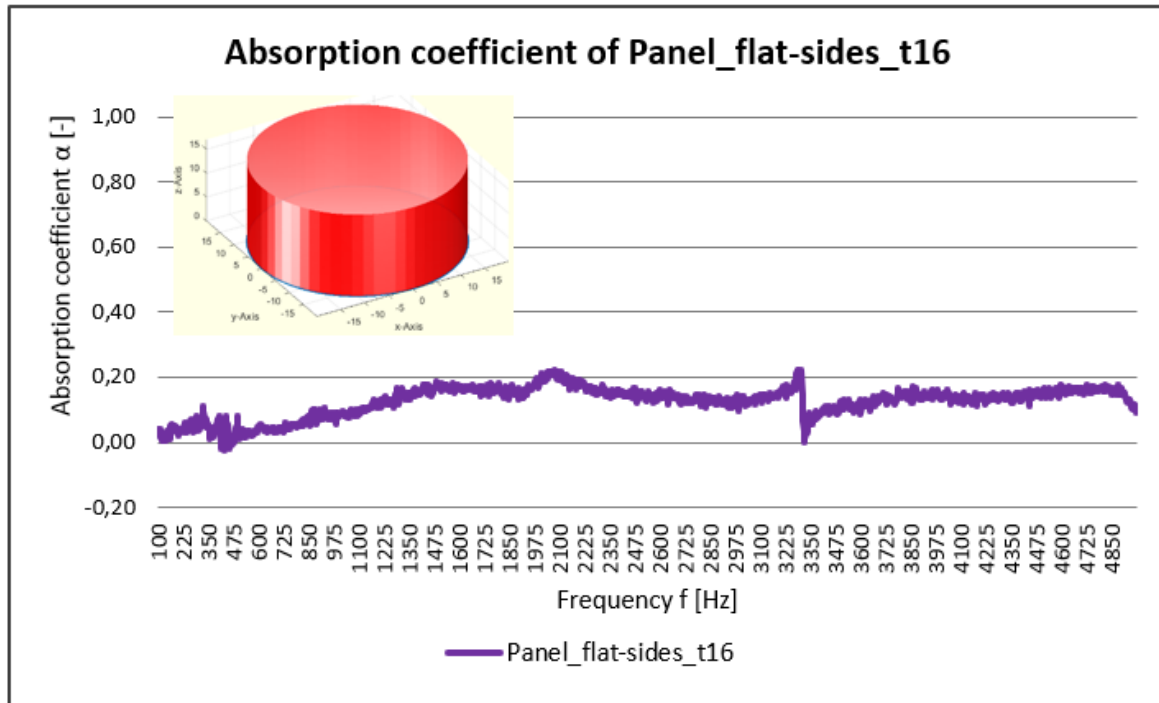


Figure 4.3: Absorption coefficient α of a panel with flat sides and a thickness of 16.00 mm

Secondly, the measured values could occur due to an incorrect set-up setting. The measurement data are collected in three passes. Before starting each measurement series, the measurement setup is adjusted according to an identical procedure. Due to pressure fluctuations of the air in the measuring room or disturbances such as external noise, there may be slight differences between the set-ups. The objects examined during the first series of measurements show a collapse of the curves at 3300 Hz, which is due to a measurement set-up that is influenced by disturbances. Comparing the curves of the reference measurements taken for the three measurement series, the deviation of the curve of the set-up setting influenced by disturbances can be seen (see Fig. 4.4). Whereas the curve of the first reference measurement at 3300 Hz shows a discontinuity (blue curve), the other two reference measurements run without interference as smooth curves (yellow and green curves).

A third cause for sound absorption could be inadequacies in the manufacture of the prototypes. Since the diameter of each model is slightly smaller than the inner diameter of the impedance tube and moreover the surface of the cylinder jacket is not perfectly flat but has unevenness, there are narrow gaps around the prototype through which sound flows. The waves are reflected at the sound absorbing end behind the sample and part of it is absorbed. If, in addition, a cavity is formed between the plate and the termination due to an uneven floor surface, sound is also absorbed. Thus the measured curve therefore deviates from the theoretically zero line.

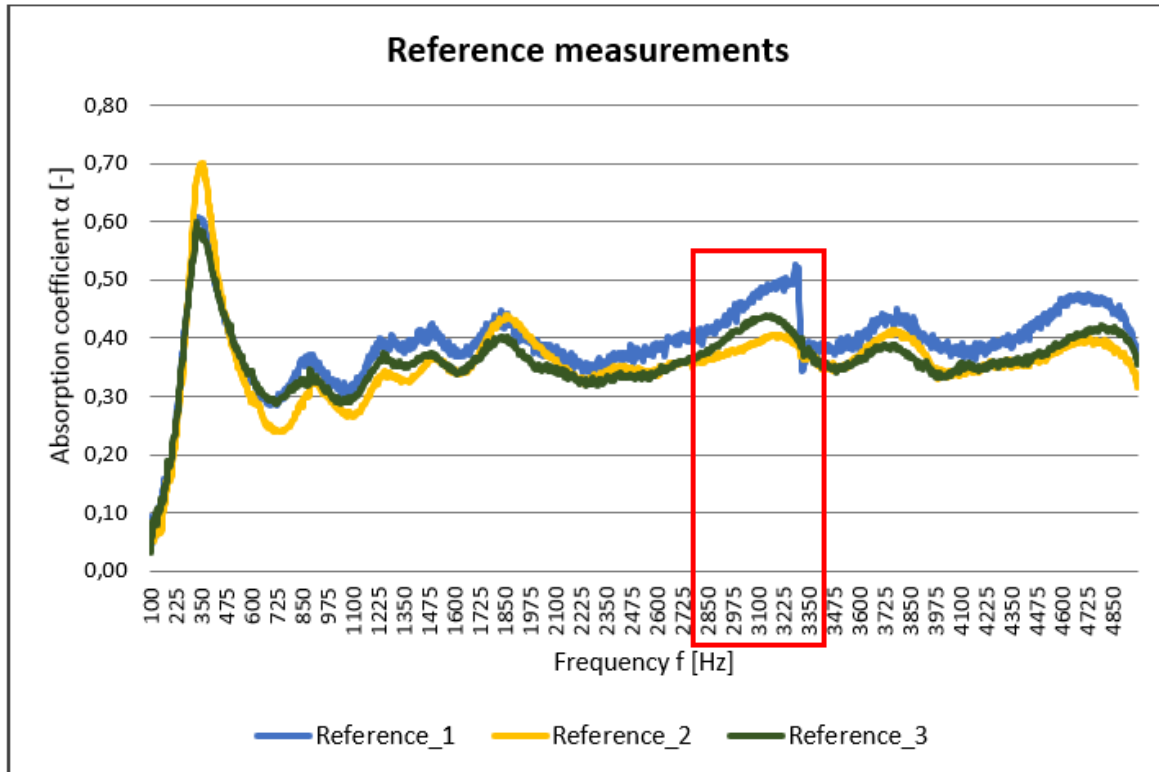


Figure 4.4: Comparison of the reference measurements

4.2.2 Measurement data of all prototypes

Fig. 4.5 illustrates the measured absorption coefficients for all prototypes. Whereas the panel with flat, smooth side surfaces absorbs hardly any sound (see Fig. 4.2), the sound propagation can be influenced by various metamaterial designs in such a way that sound is absorbed significantly better. The curves of the demonstrators show similarities, such as that the upper frequency range is influenced more strongly. In the range up to 700 Hz hardly any sound is absorbed. The highest absorption coefficients are registered in the range from 3500 Hz to 4000 Hz. Depending on the design of the test object, the influenced frequency bands shift a few frequencies up or down.

4.2.3 Cavity geometry

Panels with and without bottom

First, the effect of introducing cavities into the panels, which have a continuous bottom is examined. The dimensions of the cuboid cavities are $4.00 \times 4.00 \times 20.00$ mm (length \times width \times height) and $4.00 \times 4.00 \times 24.00$ mm for the version with a two millimeter thick bottom and without bottom, respectively. The curves representing the measurement results of the prototypes with and without floor, show significant deviations (see Fig. 4.6).

- **The maximum value of absorption**

For the panel with bottom a maximum value of $\alpha = 0.82$ is reached at 3850 Hz. When

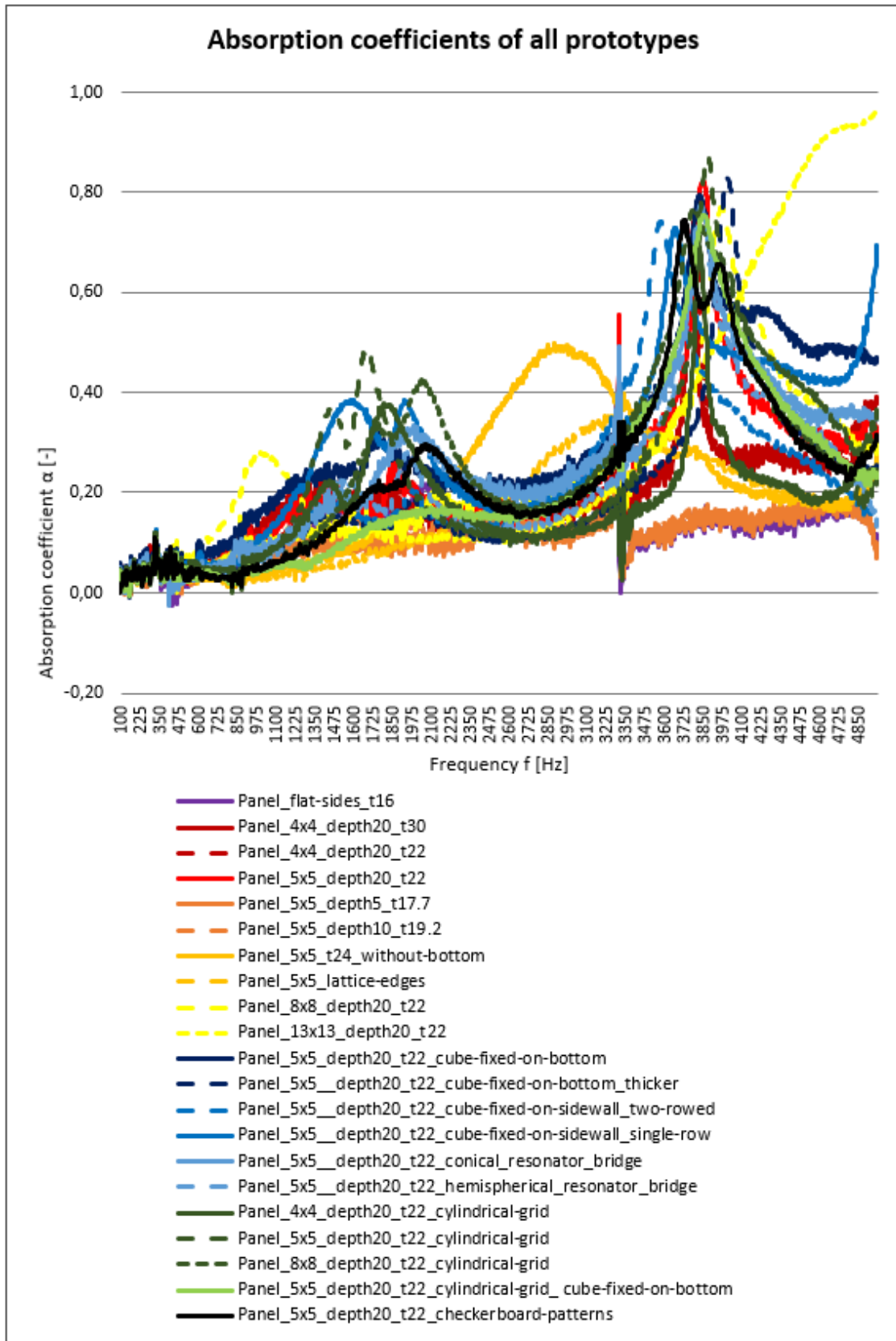


Figure 4.5: Absorption coefficients α of all demonstrators

the bottom is removed, a maximum peak of $\alpha = 0.50$ at 2950 Hz is measured, so that the maximum value is 40 % smaller and is about 900 Hz lower. The lower amplitude of the curve in the case of continuous cavities could be caused by the fact that the sound does not hit the sample material behind the cavities but rather the hard closure, where it is reflected by 100 % and thus reduces the absorption coefficient. This phenomenon supports the assumption that the specimens also absorb sound due to their material properties.

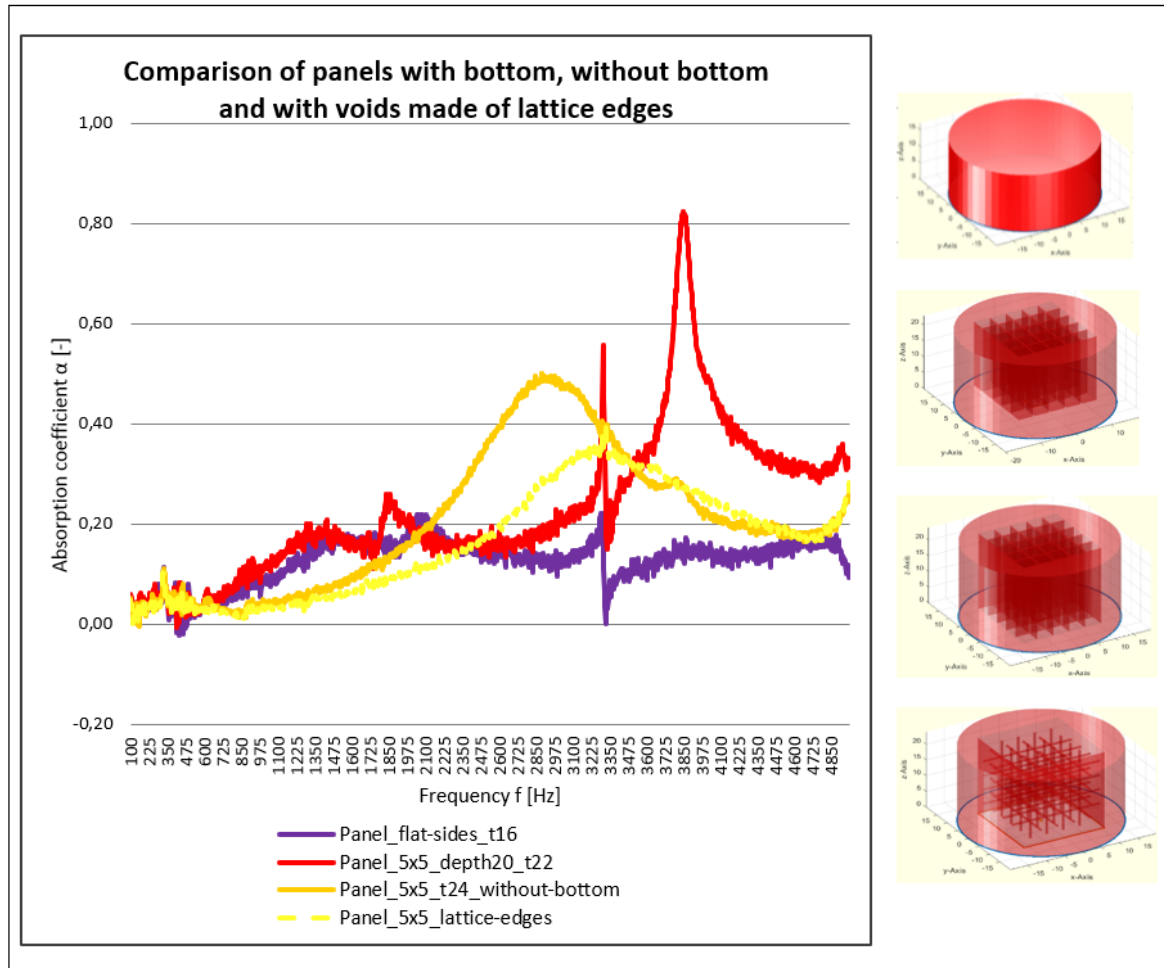


Figure 4.6: Comparison of panels with bottom, without bottom and with lattice edges

- **The location and width of the peak**

The investigation of the panel with floor indicates that the highest absorption coefficient occurs in the range of 3600 Hz to 4300 Hz. Using a prototype with continuous cavities, i.e. without a bottom, the sound absorption is concentrated in a frequency range from 1700 Hz to 4700 Hz. It therefore encompasses a wider band gap than the panel with bottom. The location of the maximum peaks can be explained by the fact that the cavities function as $\lambda/4$ resonators. For a void with a length of 20.00 mm the resonance wavelength λ corresponds to $4 \cdot 20.00 \text{ mm} = 80.00 \text{ mm}$. According to Eq. 4.2, the resonant frequency f at a sound velocity c_0 of $343.00 \frac{\text{m}}{\text{s}}$ is 4287.50 Hz . (Wanja, 2017)

$$\lambda \cdot 4 = \frac{c_0}{f} \quad (4.2)$$

Since the panel with continuous cavities is two millimeters deeper, the resonance frequency shifts downwards by about 400 Hz according to Eq. 4.2. In fact, the two maximum values are separated by about 900 Hz.

Panels with cavities made of lattice edges

Furthermore, Fig. 4.6 presents the measurement data of a prototype without bottom and containing a grid structure composed of cuboid bars. In each plane, four bars of size $0.50 \times 0.50 \times 24.00$ mm are arranged and thus form 125 cavities in a $5 \times 5 \times 5$ matrix.

- **The maximum value of absorption**

As is the case with the prototype with continuous voids, the highest absorption is found in the medium frequency range with a maximum value of $\alpha = 0.41$ at 3320 Hz. The comparatively lower amplitude could be explained by the fact that the waves again hit the hard surface of the closure. Moreover, there are no complete cavities but only beams placed inside the panel, so that a much smaller part of the sound waves is absorbed and a consideration of the geometry as $\lambda/4$ resonators is not valid.

- **The location and width of the peak**

The curve determined for the design with bars is similar to the curve for the prototype without floor. The frequency band covers 2100 Hz to 4700 Hz. The maximum values of the designs with bars are localized at medium frequencies because the depth of the cavities is smaller than that of the design without a bottom.

Bottom thickness

A further investigation of the influence of the bottom thickness is carried out. If the absorption coefficients of two prototypes, which differ in the wall thickness of the floor by eight millimeters, are plotted over frequency, hardly any difference can be seen (see Fig. 4.7).

- **The maximum value of absorption**

A maximum absorption coefficient is measured at around 3800 Hz for both test specimens. In the design with a floor thickness of two millimeters, the height of the peak is about 30 % higher than the value recorded with a wall thickness of ten millimeters. The higher absorption for a demonstrator with lower floor thickness, as well as the shift of the maximum absorption coefficients by almost 500 Hz to lower frequencies, can not be explained by the available measurement data. This shift of the resonance frequency may be influenced by the lower air pressure prevailing at the time of the measurement and the resulting lower speed of sound. Nevertheless, the identical position of the peaks indicates that they represent the resonant frequencies of the designs with a cavity depth of 20.00 mm.

- **The location and width of the peak**

For both panels the rise and fall of the curves around the point of highest sound absorption follow a similar course. However, it is not possible to provide a substantiated explanation of the location of the frequency band on the basis of the available data.

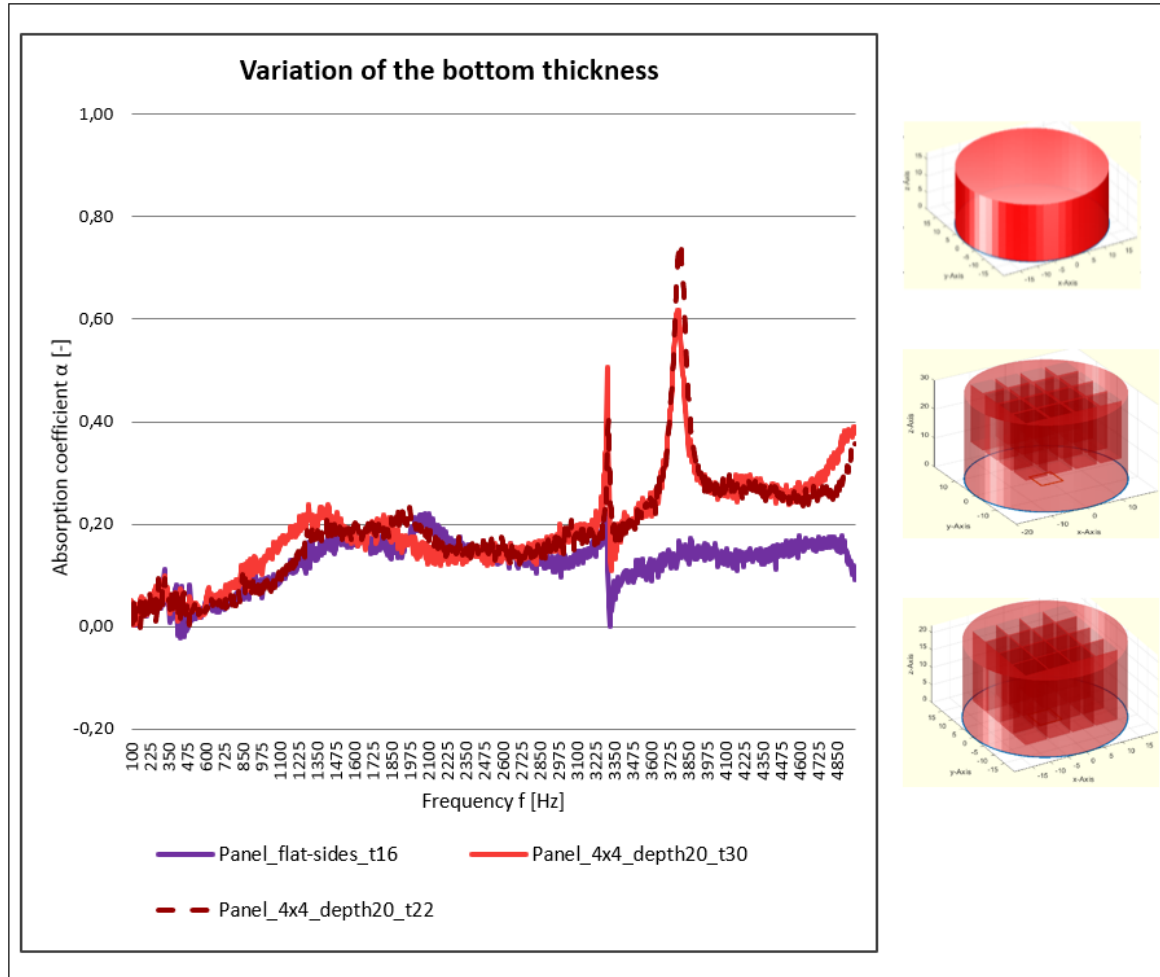


Figure 4.7: Variation of bottom thickness

Number and geometry of the cavities

Alternatively to the bottom thickness, the effect of varying the number and geometry of the cavities is investigated (see Fig. 4.8). For a 4×4 matrix the edge length of the rectangular cavity floor is 6.00 mm, for a 5×5 or 8×8 matrix the edge length is 4.00 mm and 2.50 mm, respectively.

- **The maximum value of absorption**

The highest sound absorption coefficients are measured in the upper frequency range. A maximum value of $\alpha = 0.75$ is measured at 3790 Hz for an edge length of 6.00 mm. Considering edge lengths of 4.00 mm or 2.50 mm, the maximum peaks are at 3850 Hz ($\alpha = 0.82$) and at 3970 Hz ($\alpha = 0.77$), respectively.

- **The location and width of the peak**

Whereas the panels containing cavities with edge lengths of 6.00 mm and 4.00 mm behave similarly to the panel with flat, smooth side surfaces in the lower and medium frequency range, the design with cavities of edge length 2.50 mm absorbs significantly more sound from 750 Hz to 1200 Hz. One reason for the sound absorption may be

that the individual cavities, especially the depths, are not built identically due to their small dimensions, and sound of different wavelengths is absorbed due to these deviations. If the differences in these resonance frequencies are very small, beat could occur, which means that oscillations with closely spaced frequencies f_1 and f_2 occur simultaneously. The frequency spectrum then contains peaks at three frequencies, namely at the frequencies f_1 , f_2 and the difference between the two at $\Delta f = f_1 - f_2$. (Hussmann, n.d.) (Shive & Weber, 1993) Another explanation may be a superposition of vibrations. In addition to the excitation of the voids by the incident wave, the cavities could also influence each other and induce to vibrate at low frequencies.

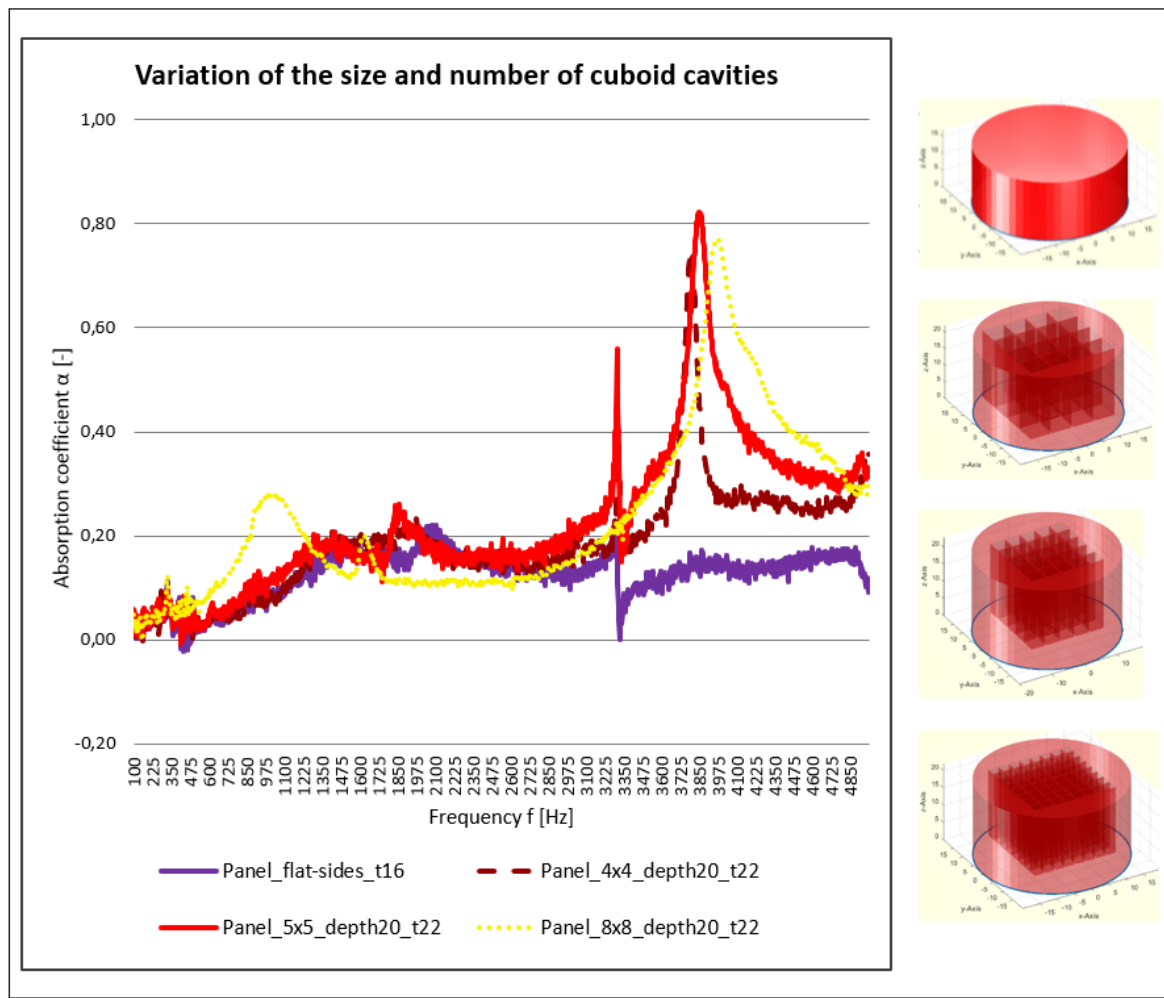


Figure 4.8: Variation of grid size and number

Starting from the frequency at which the maximum absorption coefficient is measured, the rise and fall of the curve progressions is analyzed for the three panels. One could derive a correlation between the dimensions of the cavity and the width of the band gap. Accordingly, the smaller the cross-sectional area, the wider the frequency band becomes. Choosing cavities with edge lengths of 6.00 mm and thus a base area of 36.00 mm^2 , frequencies from 3700 Hz to 4000 Hz are absorbed. For medium and small cross sections with base areas of 16.00 mm^2 and 6.25 mm^2 , the absorption coefficient curves are wider, covering 3600 Hz to 4600 Hz and 3500 Hz to 5000 Hz, respectively. Considering that the total volume of the cavities is identical for each configuration, it

can be assumed that the number and dimensions of voids influence the width of the frequency band. Fig. 4.9 illustrates the boundary layer of a pipe through which a fluid flows. A boundary layer builds up on a cavity surfaces due to friction, whereby energy is absorbed. With increasing ratio of boundary layer thickness to cavity edge length and also with a greater number of voids, more energy is absorbed. (Spurk, 2010)

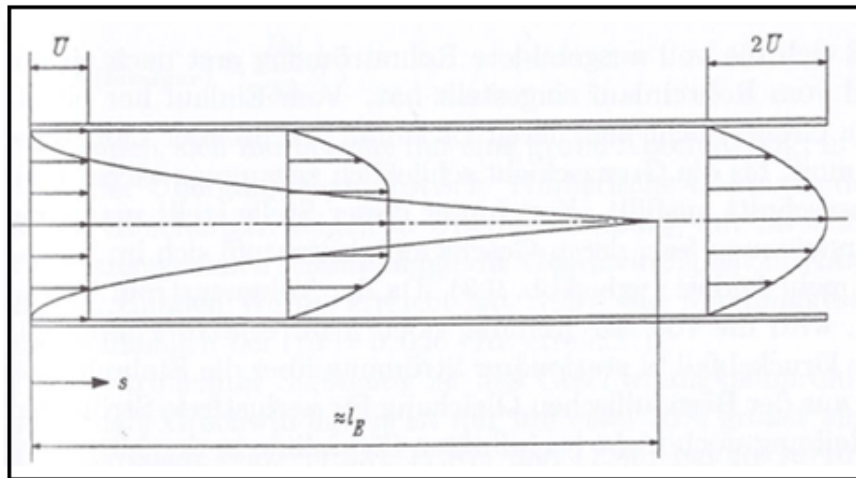


Figure 4.9: Boundary layer in a pipe
(Spurk, 2010)

An additional explanation for the course of the curve is again the manufacturing inaccuracy of the cavity geometries. During the production of the prototypes, defects may occur due to the low accuracy of the Prusa SL1® as well as the CW1®. Especially for small geometries the probability of deviations from the nominal dimension of the created geometries increases. For example, some cavities may have smaller depths instead of the set design parameters. As a result, the wavelengths of the $\lambda/4$ resonators differ slightly from one another. Thus, waves with different wavelengths or various frequencies can propagate in the voids and sound of different frequencies is absorbed. This results in a wider frequency band and a shift of the curve representing the course of the absorption coefficients to higher frequencies.

As Fig. 4.10 illustrates, the sound reducing properties of a plate with voids arranged in a 13×13 matrix can not be measured completely. Whereas there is hardly any absorption in the lower and middle frequency range, a significant increase in the absorption coefficients can be detected for frequencies above 3500 Hz. This rise in the curve can be measured by means of the acoustic impedance tube, but the maximum absorption coefficient as well as the further course of the curve are beyond the detectable frequency range of 5000 Hz. Although according to Eq. 4.2 the resonant frequency for the considered model with 20.00 mm deep cavities results in 4287.50 Hz, the resonance frequency is clearly shifted to higher values. The measurement results support the hypothesis that the resonant frequency is moved to higher frequencies as a result of a smaller cavity geometry and a larger lattice matrix. In addition, the curve demonstrates the limits of the impedance tube with regard to the geometry of the test specimens.

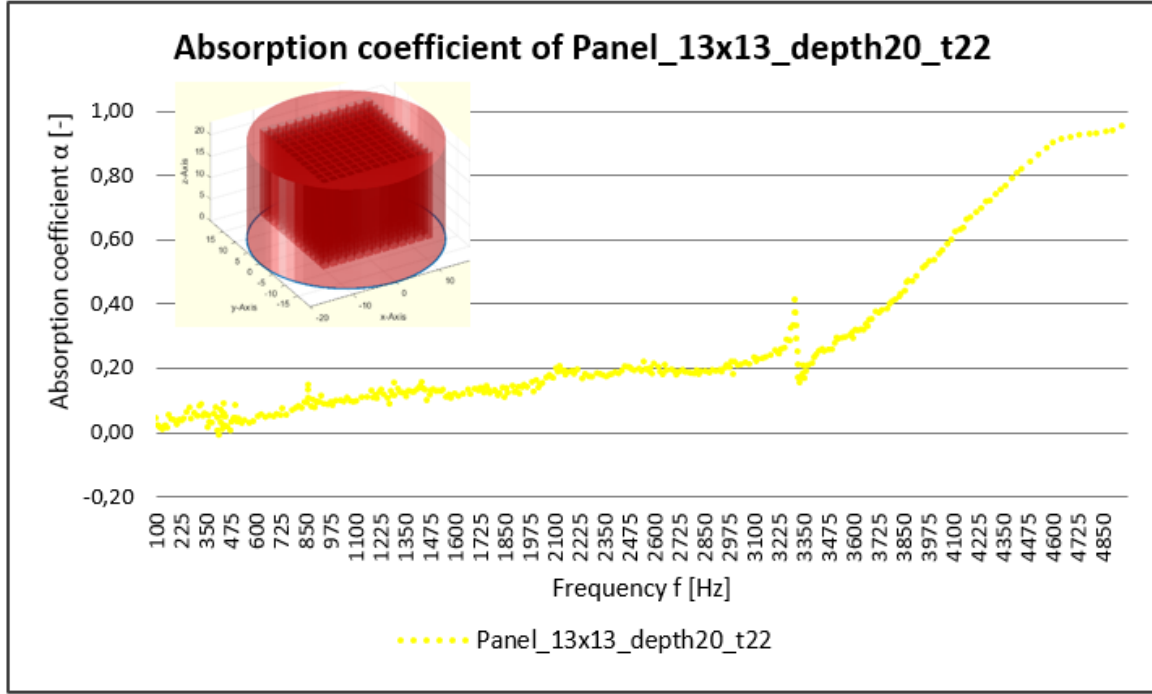


Figure 4.10: Absorption coefficient α of Panel_13 × 13_depth20_t22

Reproduction of the same design

Fig. 4.11 shows the absorption coefficients of four identical panels with cuboid cavities of dimensions $4.00 \times 4.00 \times 20.00$ mm arranged in a 5×5 matrix.

- **The maximum value of absorption**

The fact that all curves have a maximum peak at about 3850 Hz in common proves the accuracy of the treatment of the cavities as $\lambda/4$ resonators and the natural frequency at 3850 Hz.

- **The location and width of the peak**

Whereas the position and the maximum value of the absorption coefficients are almost identical for the four curves, significant deviations between the measured values of the four panels, that are built from the same 3D model, can be noticed especially in the lower frequency range. The curves deviate considerably from each other in the range from 700 Hz to 3400 Hz. This may be due to the fact that the specimens with names "numb1", "numb2" and "numb3" are made of a different material (grey tough resin) than the first object(azure blue tough resin). These two materials are each made of a resin that is used to build robust and immovable components and should therefore only differ in the colour. In fact, significantly different absorption coefficients are measured especially in the lower frequency range, depending on the material. The influence of the material on the sound absorption can be seen in the detected curves. An explanation of the measurement data is not possible, since the data sheets do not include information about the specific composition and therefore the differences between the two materials.

Furthermore, there are large differences in the location of the peaks in the range from 1700 Hz to 2600 Hz among the three prototypes "numb1", "numb2" and "numb3". Since they all have the same design and are made of the same material, identical measured values should be determined. It can be assumed that manufacturing accuracies, in particular the surface qualities of the shell surfaces of the plates and the lower bottom surfaces, influence the progression of the curves and cause these large deviations.

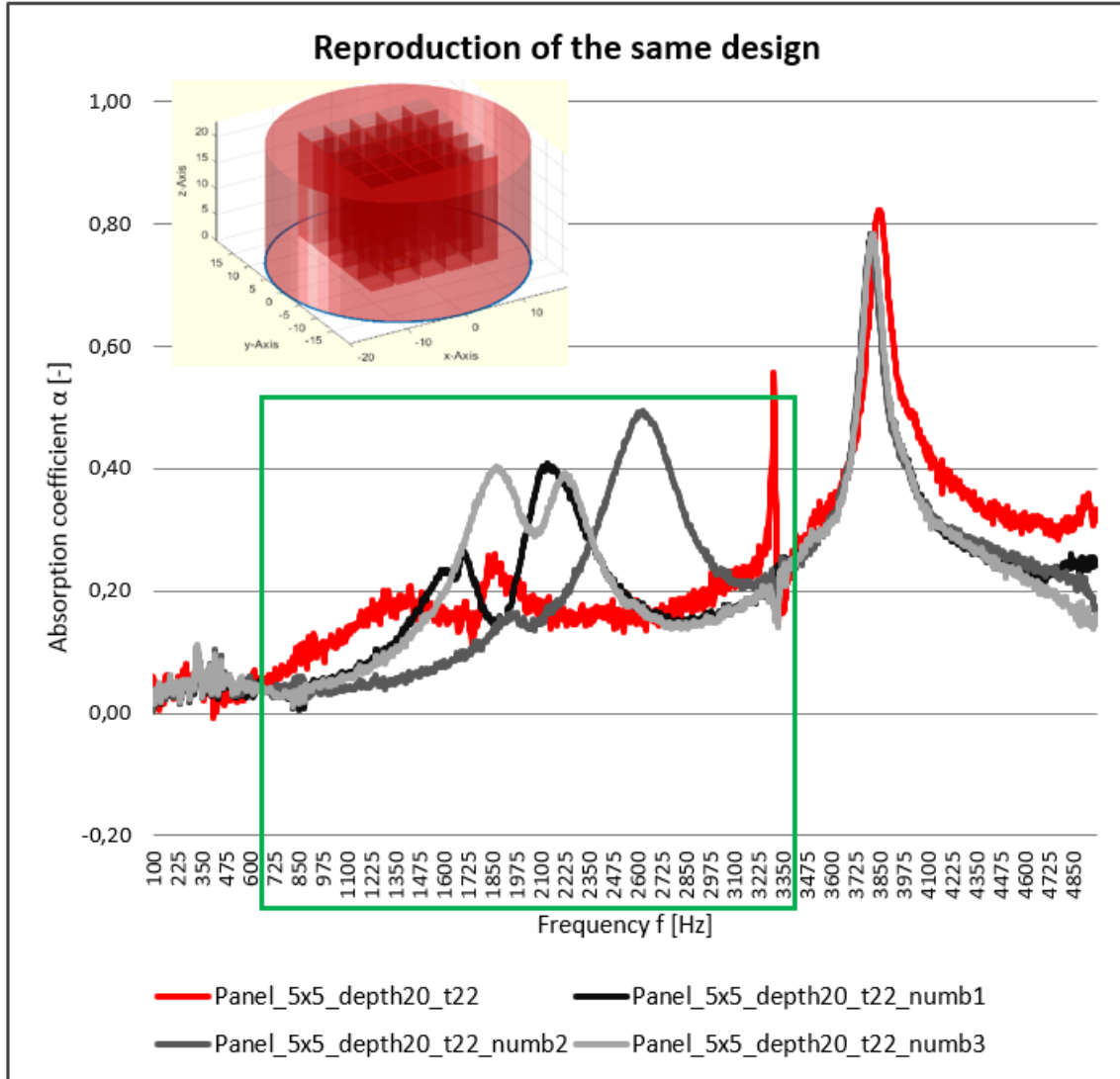


Figure 4.11: Reproduction of the same design

Cavity depth

Besides the base area of the voids, the cavity depth is another design parameter that is varied. The curves shown in Fig. 4.12 illustrate the absorption coefficients of prototypes with cavity depths of five millimeters, ten millimeters and 20.00 mm.

- **The maximum value of absorption**

Again, the curves for the different cavity depths can be explained by Eq. 4.2. With

resonant frequencies of 17150 Hz and 8575 Hz for a depth of five millimeters and ten millimeters, respectively, the resonance frequencies of the smaller cavities are substantially higher than for the void with a depth of 20.00 mm and are thus outside the recordable measuring range of 5000 Hz.

- **The location and width of the peak**

For 20.00 mm deep voids high absorption coefficients especially in the upper frequency range at 3850 Hz are measured. Compared to this, no significant absorption coefficients are recorded in the case of smaller cavity depths. Moreover, the measurement data determined for the demonstrators with a depth of five millimeters and ten millimeters hardly differ from one another when regarding a frequency range up to 5000 Hz.

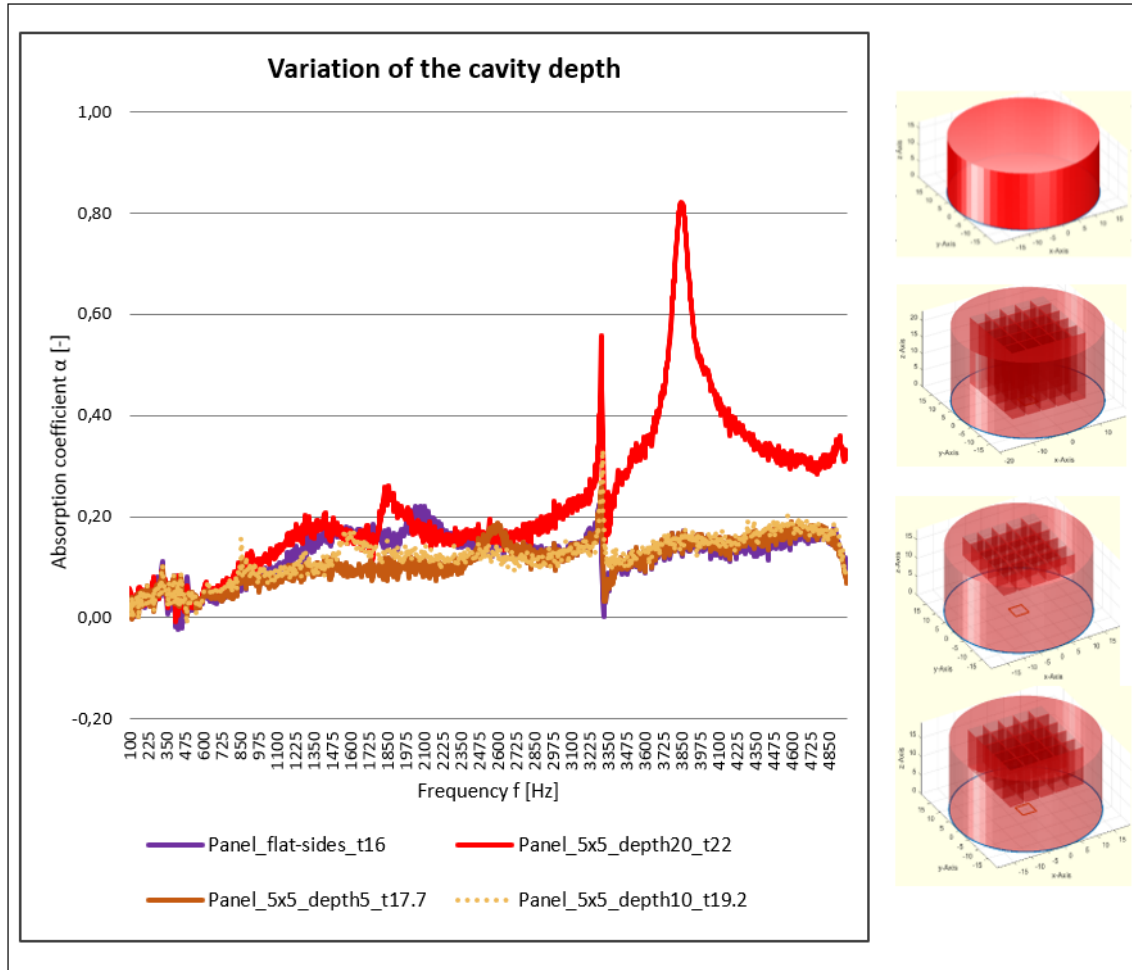


Figure 4.12: Variation of cavity depth

Cavity geometry

Furthermore, variations of the geometry of the individual cavities are investigated. Whereas previous investigations have focused only on rectangular cavities that are embedded in the plate, a comparison with cylindrical grids is carried out in the following. Fig. 4.13 shows the absorption coefficients of cuboidal cavities with dimensions of $4.00 \times 4.00 \times 20.00$ mm

and of cylindrical cavities with a diameter of four millimeters and a depth of 20.00 mm, each arranged in a 5×5 matrix structure.

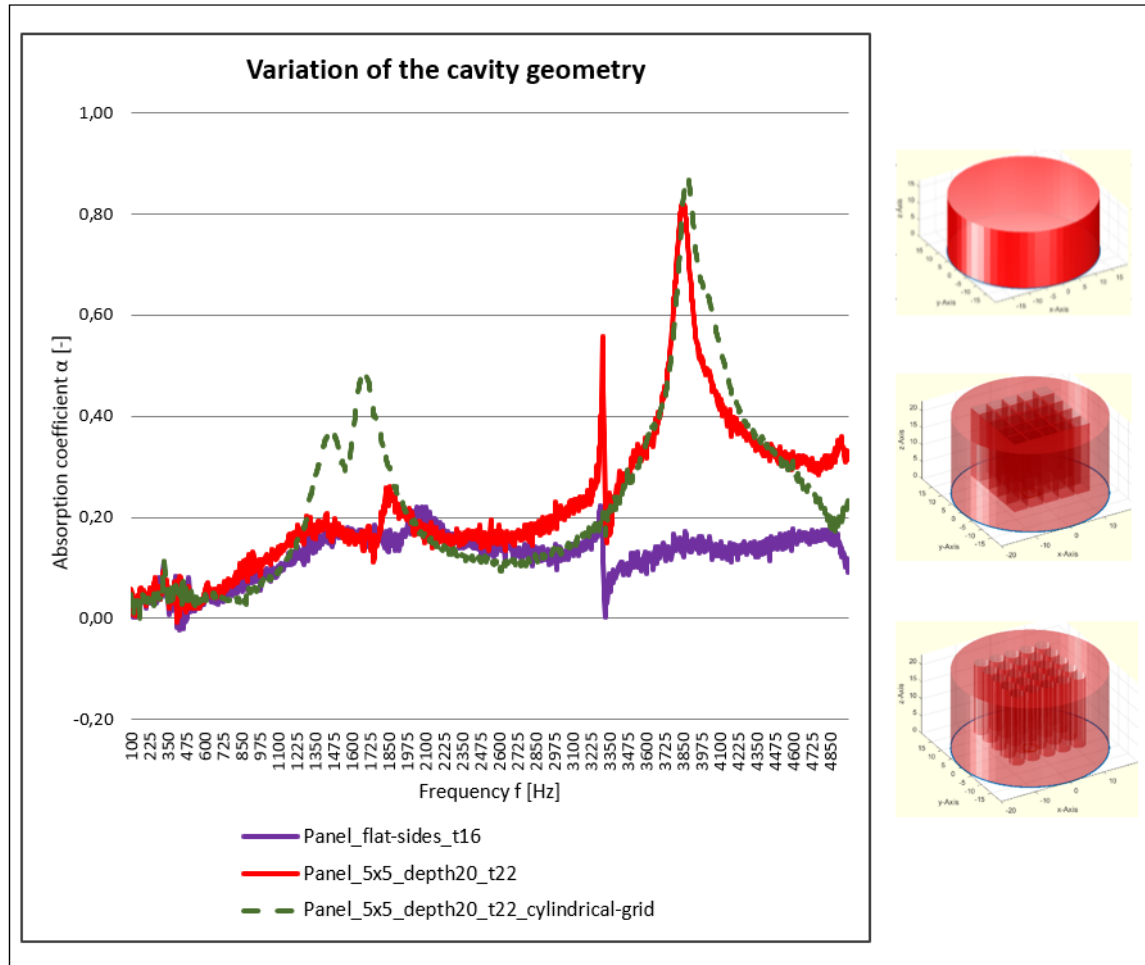


Figure 4.13: Variation of cavity geometry

- **The maximum value of absorption**

Choosing cylindrical cavities, two high peaks at 1460 Hz ($\alpha = 0.37$) and 1680 Hz ($\alpha = 0.49$) are measured. The difference with the cuboid design is up to 364 % in this range. Possible reasons for these high absorption coefficients correspond to the above-mentioned hypotheses on manufacturing inaccuracies, beat and superimposition of vibrations. Another explanation of the two peaks and the curve dip at 1550 Hz, respectively is destructive interference. If two rectified linear vibrations overlap, a resulting oscillation is obtained whose amplitude corresponds to the sum of the amplitudes of the partial oscillations. If two waves of the same amplitude and frequency meet with a phase difference of 180° , the oscillations extinguish (see Fig. 4.14). (Stuart, 1966) Similar to the square cavity design, the variation with cylindrical voids has maximum absorption values in the higher frequency range. In the case of the square design, a maximum absorption of $\alpha = 0.82$ at 3850 Hz is achieved, whereas for cylindrical cavities the peak rises up to a value of $\alpha = 0.87$ at 3880 Hz, and is thus only six percent higher.

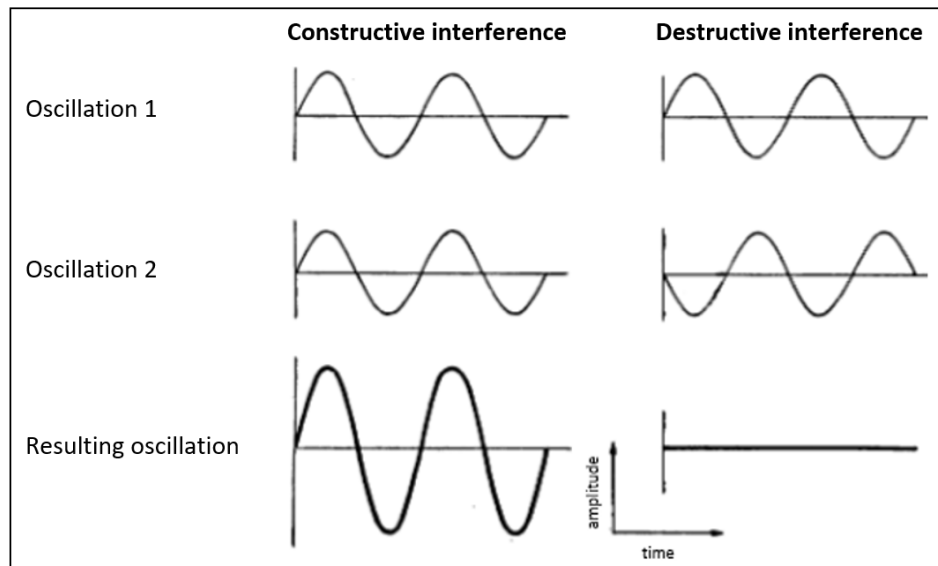


Figure 4.14: Constructive and destructive interference
(Stuart, 1966)

- **The location and width of the peak**

The panel with cylindrical voids absorbs frequencies from about 1300 Hz to 1900 Hz much more than the demonstrator with cuboid cavity geometry. Considering the further frequency range, it can be noticed that both curves rise identically, but the curve decreases significantly steeper in the design with cuboidal cavities up to about 4300 Hz. As the curve progresses, almost constant values around $\alpha = 0.3$ are detected. In contrast, the decline of the curve is less precipitous in the model with cylindrical voids, but the absorption coefficients decrease continuously. From 4690 Hz onwards lower absorption values are measured in the cuboid cavity design. The almost identical position and approximately equal height of the maximum absorption coefficients of both demonstrators is explained by the identical resonant frequency of the two cavity geometries at 4287.50 Hz according to Eq. 4.2.

The slight widening of the frequency band of cylindrical voids can be explained by the fact that the base area of the cavity with a diameter of four millimeters is slightly smaller than that of the cuboid cavity with edge lengths 4.00×4.00 mm. The base area for cylindrical cavities, each measuring 12.57 mm^2 , is about 27% smaller than for cuboid voids with 16.00 mm^2 . The widening of the band gap with a smaller cavity geometry correlates with the results of the investigation of differently sized cuboid cavity designs (see Fig. 4.8 to 4.10). In the following, the assumption made for cuboid voids, that a smaller footprint affects the width of the frequency band, is examined to investigate whether such a hypothesis is also valid for cylindrical cavities.

Number and size of cylindrical cavities

Fig. 4.15 illustrates the absorption coefficients determined for panels with cylindrical cavities of different dimensions over the considered frequency range. The diameters of the voids are 6.00 mm, 4.00 mm and 2.50 mm for the 4×4 , 5×5 and 8×8 matrix, respectively.

- **The maximum value of absorption**

The measured resonance frequencies of the considered panels are located approximately in the same frequency range. For the demonstrator with 4×4 lattice matrix, the maximum absorption coefficient is $\alpha = 0.69$ at 3830 Hz or $\alpha = 0.87$ at 3880 Hz and $\alpha = 0.77$ at 3790 Hz for the models with 5×5 or 8×8 matrix. As shown in Fig. 4.15, the smaller the footprint and the greater the number of cavities, the wider the frequency band is. This confirms the hypothesis that the size of the base area has an influence on the width of the frequency band.

Since the high values of the absorption coefficients in the range below the resonance frequency can not be clearly explained on the basis of the measurement data, it is referred to the assumptions already made regarding an incorrect set-up, sound absorption due to material properties, manufacturing inaccuracies, beat and superimposition as well as destructive interference.

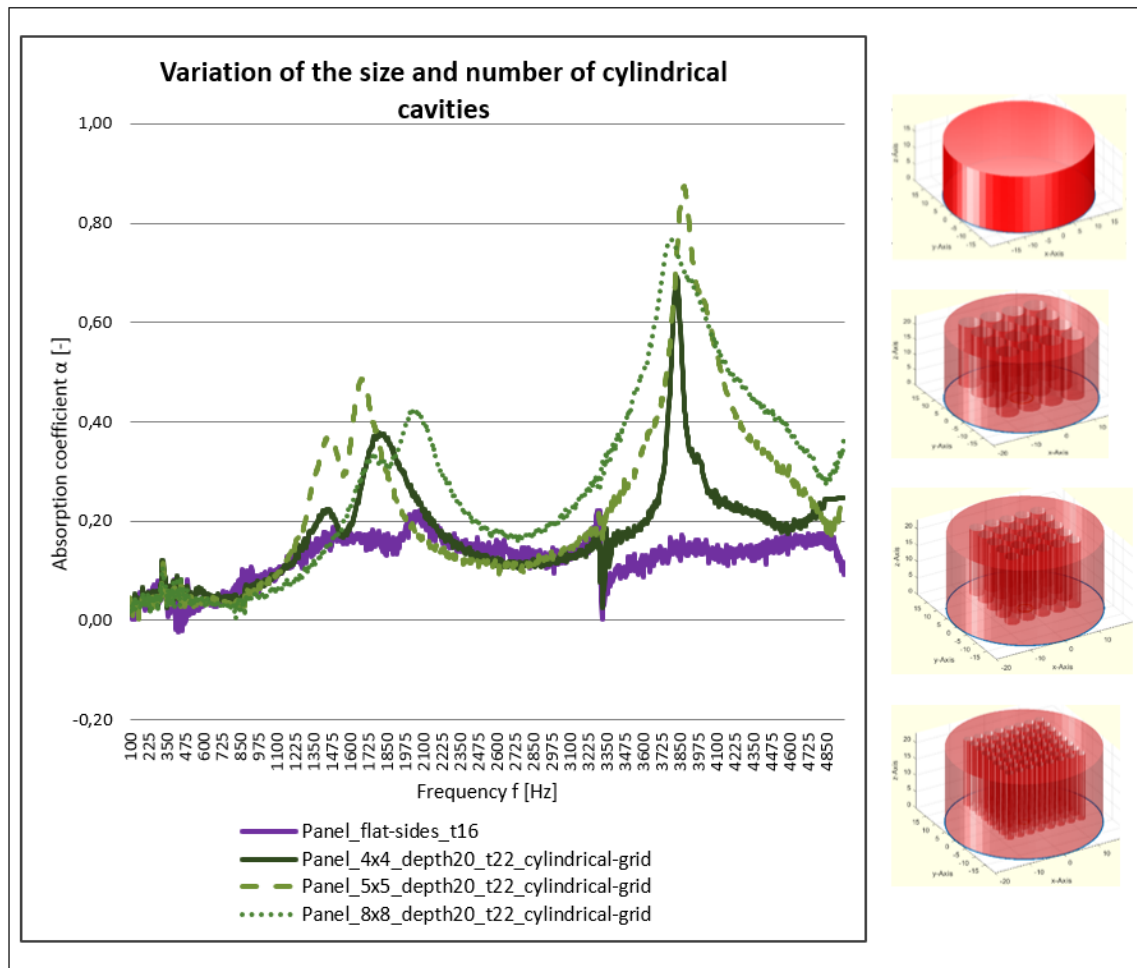


Figure 4.15: Variation of grid size and number of cylindrical cavities

- **The location and width of the peak**

For voids with the smallest diameter, the frequency bands are significantly wider than for those with medium and large dimensions. Thus, it can be deduced that the geometry also affects the width of the band gap. Whereas smaller cuboid shaped cavities cause an expansion of the frequency band only to higher frequencies, the band gap widens simultaneously to higher and lower frequencies with a smaller cylindrical base area.

4.2.4 Resonant structures

Small cuboid resonators embedded in cuboid voids

After investigating the impact of cavity geometry and number as well as floor thickness on the sound absorbing effect of panels, the influence of embedded resonators is analyzed. Fig. 4.16 shows the absorption coefficients over frequency of two samples with cuboid cavities arranged in a 5×5 grid, of which one contains cuboid resonators. A similar curve is obtained for both panels. However, by attaching cuboid resonators with dimensions of $1.00 \times 1.00 \times 20.00$ mm (length \times width \times height) to the bottom of the voids, the sound absorption can be improved in almost all frequency ranges.

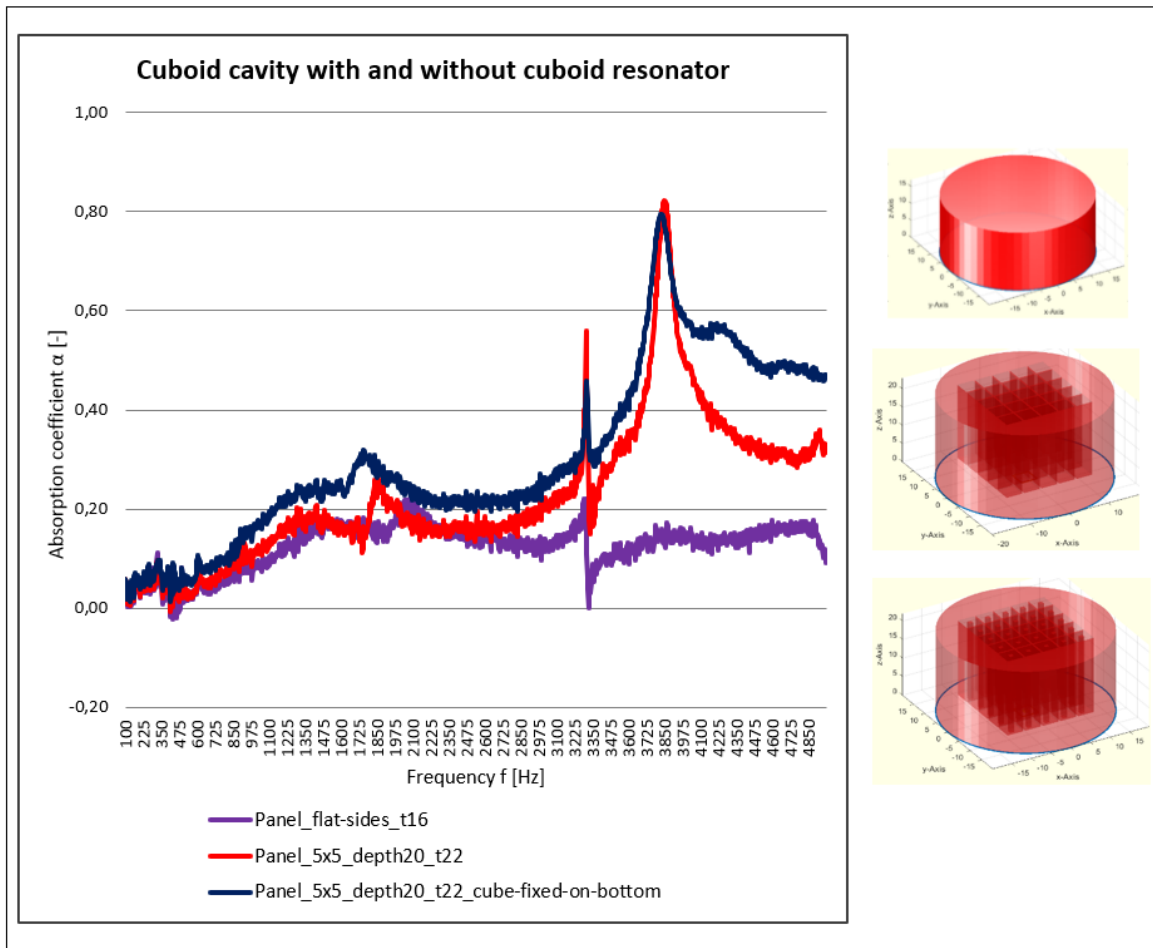


Figure 4.16: Cuboid cavity with and without rectangular resonator

Fig. 4.17 illustrates the sound absorption improvement which is determined for the demonstrator with inserted resonant structures of cuboid shape in the cavities. The curve represents the ratio of the absorption coefficients α of the model which contains resonators to those of the prototype without resonant structures over the frequency. All points above the orange line indicate an enhancement of sound absorption due to the added resonators by x -times of the vertical axis display. The presented curve shows clearly that the sound absorption is improved in almost all frequency ranges, if resonators are inserted into the cuboid cavities.

Especially above 4000 Hz the addition of resonant structures increases the absorption coeffi-

cient by 67 %. With a maximum absorption coefficient of $\alpha = 0.80$ at 3830 Hz, the prototype with resonators absorbs only 2.5 % more sound than the design without resonant structures ($\alpha = 0.82$ at 3850 Hz). Moreover, the curve of the sample body with inserted resonators decreases substantially less after reaching the maximum absorption value.

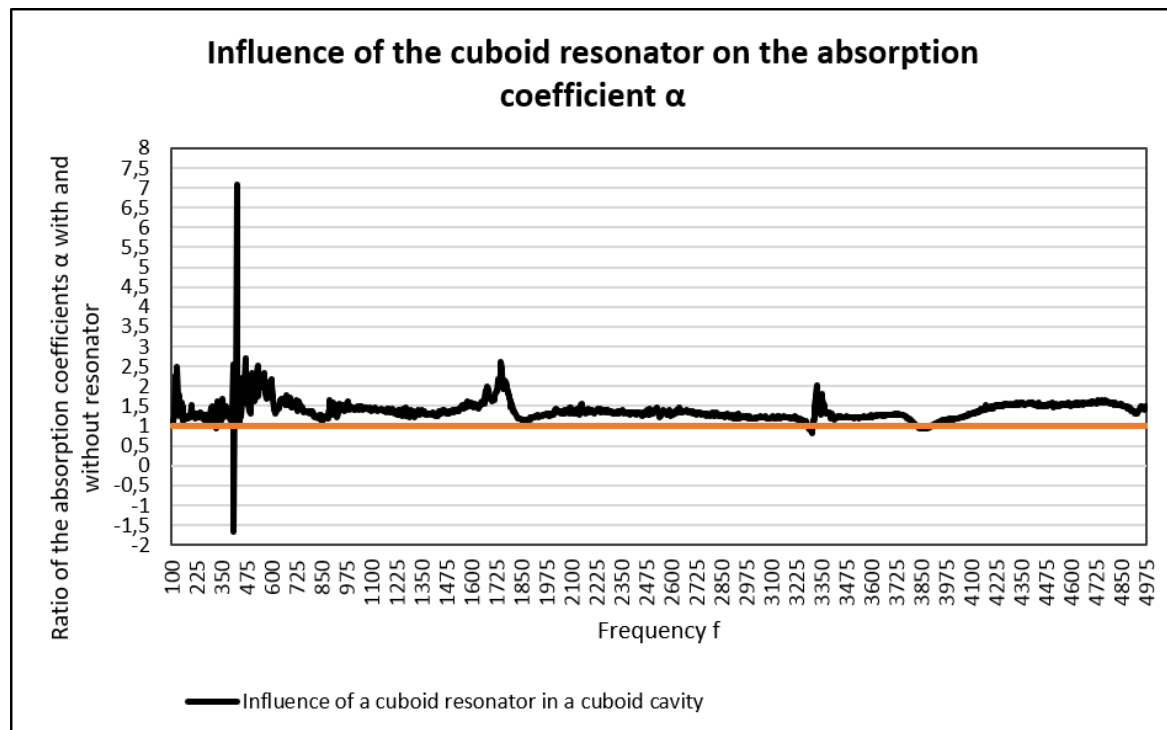


Figure 4.17: Influence of the cuboid resonator on the absorption coefficient α

Small cuboid resonators embedded in cylindrical voids

Besides cuboid cavities, resonant structures of size $1.00 \times 1.00 \times 20.00$ mm are inserted in cylindrical voids with a diameter of four millimeters and a depth of 20.00 mm. The measured absorption coefficients are illustrated in Fig. 4.18.

- **The maximum value of absorption**

With a maximum absorption coefficient of $\alpha = 0.75$ at 3850 Hz, the curve for the prototype with embedded resonators lies 16% below the curve obtained for the sample without resonant structures ($\alpha = 0.87$ at 3880 Hz).

- **The location and width of the peak**

If the described resonators are attached to the cavity floors, the sound absorption deteriorates in the range below 2100 Hz and above 3820 Hz. Furthermore, noticeably lower absorption coefficients are recorded in the low-frequency range from about 950 Hz to 2000 Hz. The difference here is almost 500 % to the panel without resonator. However, for frequencies from 2000 Hz to 3850 Hz the absorption values of the prototype with resonators are slightly higher than those measured for the panel without resonant structures. The limits of the band gap around the highest peak are slightly wider for the

design with resonators. Both curves decrease significantly after reaching the maximum value of sound absorption.

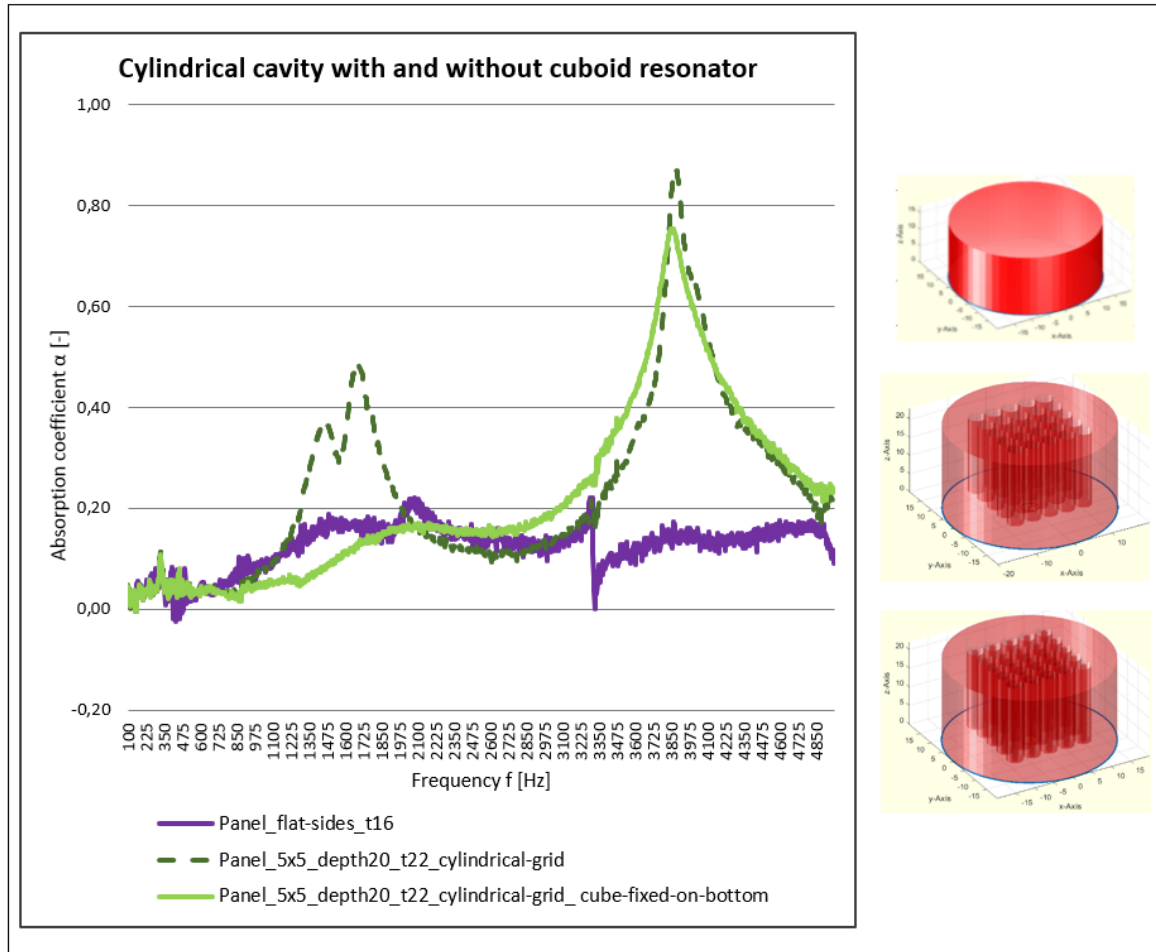


Figure 4.18: Cylindrical cavity with and without rectangular resonator

Cuboid resonators

Fig. 4.19 presents the influence of varying the dimensions of the resonant structures on the sound absorption. Instead of a cross-sectional area of 1.00 mm^2 and a length of 20.00 mm, resonant bodies of size $2.00 \times 2.00 \times 5.00 \text{ mm}$ are added to cuboid voids that are of the dimensions $4.00 \times 4.00 \times 20.00 \text{ mm}$.

- **The maximum value of absorption**

A similar curve is obtained for both variants. Due to the wider, shorter resonator geometry, the absorption coefficients are shifted to higher frequencies, resulting in a maximum value of $\alpha = 0.83$ at 4000 Hz. In the design with resonator dimensions of $1.00 \times 1.00 \times 20.00 \text{ mm}$, the highest peak is $\alpha = 0.79$ at 3820 Hz.

- **The location and width of the peak**

Furthermore, the prototype with shorter resonators absorbs less sound in large parts and

the bandwidth around the frequency at which the highest absorption occurs is narrower. The difference between the absorption characteristics of the two resonator designs is particularly large for frequencies above 4200 Hz. For narrower resonators, characteristic values are in part more than twice as high.

Firstly, the increase in resonant frequency could be explained by the fact that the footprint of the resonator with dimensions $2.00 \times 2.00 \times 5.00$ mm is very large compared to the cavity floor with size 4.00×4.00 mm. As a result, the cavity depth is reduced by the height of the resonant structure to 15.00 mm. According to Eq. 4.2, this increases the resonant frequency up to 5716 Hz. On the other hand, Eq. 3.1 indicates that the spring stiffness of the resonator is increased and the natural frequency thus rises, since the volume and the mass of the resonators are identical.

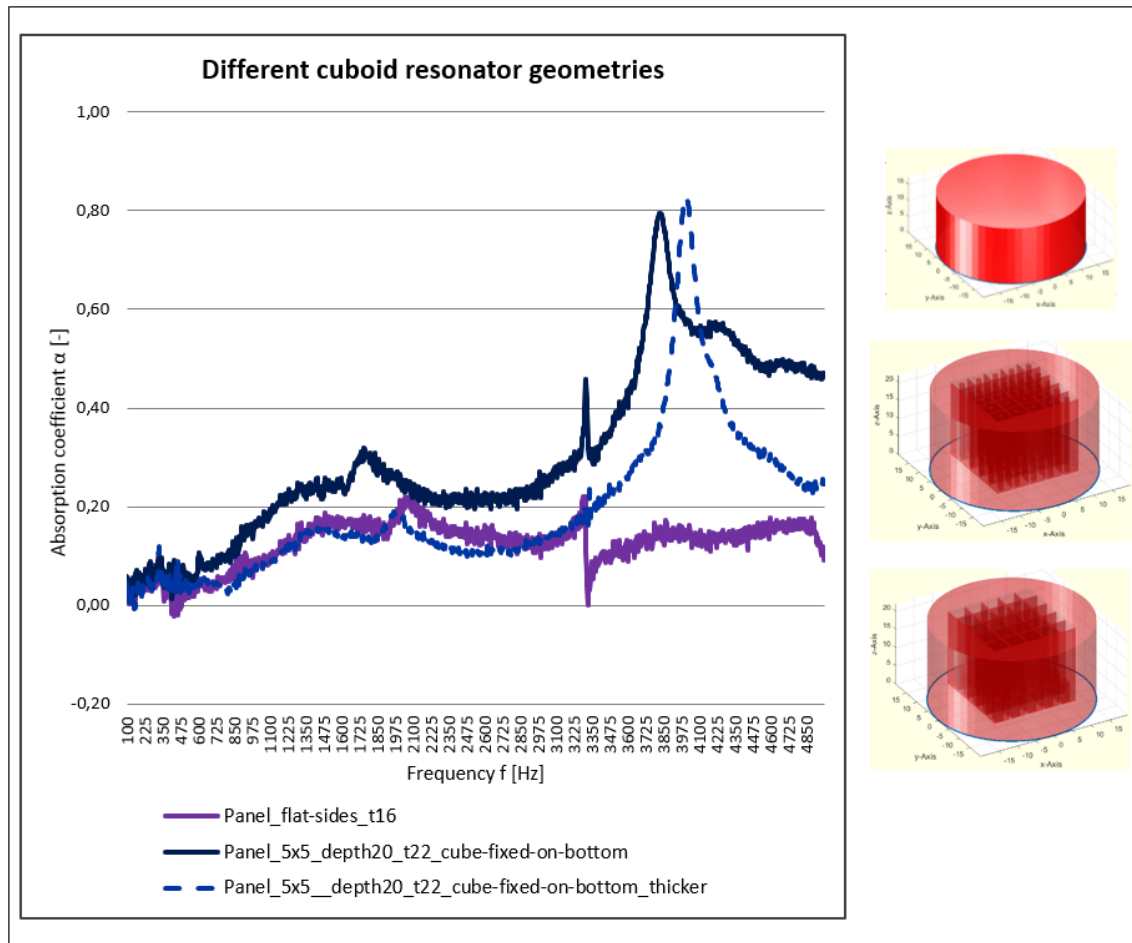


Figure 4.19: Different rectangular resonator designs

Resonator geometry

In addition to cuboid resonators, further geometric bodies are inserted into the voids and fixed to the bottom. Fig. 4.20 shows the measured data for cuboid resonators with dimensions $1.00 \times 1.00 \times 20.00$ mm and $2.00 \times 2.00 \times 5.00$ mm as well as for conical and hemispherical designs. Cones and hemispheres have a diameter of three millimeters and a height of four

millimeters or a diameter of three millimeters respectively and are each attached to the end of a $1.00 \times 1.00 \times 10.00$ mm long support structure that is fixed to the cavity floor.

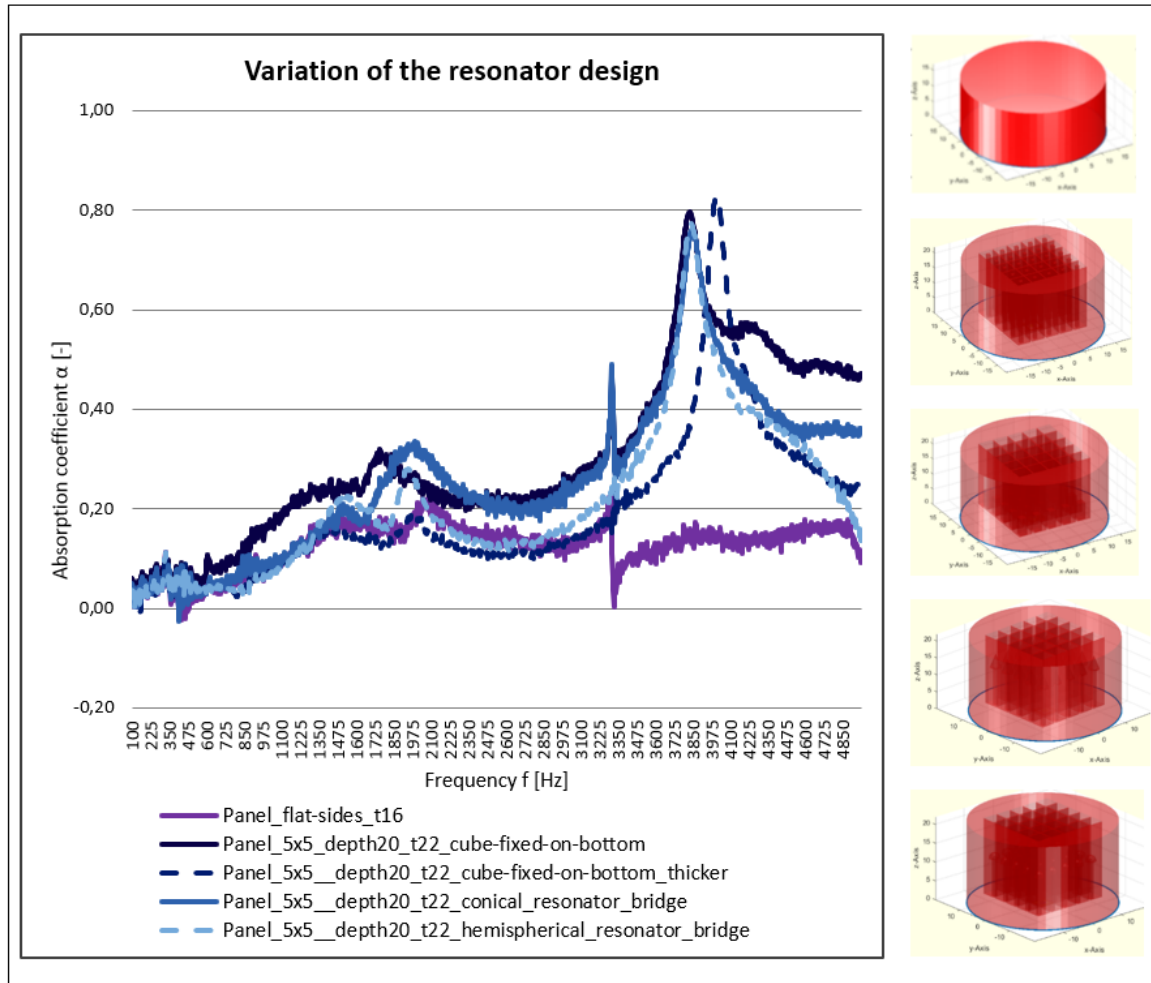


Figure 4.20: Variation of the resonator design

- **The maximum value of absorption**

Choosing a narrow cuboid, conical and hemispherical design, maximum absorption peaks of $\alpha = 0.79$ at 3820 Hz, $\alpha = 0.76$ at 3840 Hz and $\alpha = 0.78$ at 3840 Hz are measured, respectively. Looking at the further course of the curve, a sharp drop can be seen for the hemispherical resonator design. In contrast, if resonant structures of cuboid or conical shape are selected, the absorption coefficients assume almost constant values of $\alpha = 0.47$ or 0.35 . The curve of the resonators with wider dimensions is shifted to higher frequencies and reaches a maximum absorption coefficient of $\alpha = 0.83$ at 4000 Hz. Since the lengths of the prototypes with hemispherical, conical and cuboidal narrow resonators are almost identical, these designs have a similar resonant frequency. The obtained results support the assumption made above that the resonant frequency is increased by adding shorter and wider resonators.

- **The location and width of the peak**

In the lower frequency range, significantly lower absorption coefficients are measured. Especially for narrow cuboid, conical and hemispherical resonators, the gradient of the

curves is similar up to the maximum peak. Around the maximum peak, the curve of the panel with wider cuboid resonators has a much narrower frequency band than the curves of the other geometries.

Fixation point

Besides the connection of the resonators to the cavity floors, the effect of mounting them on the inner side surfaces of the voids on the sound absorption is studied (see Fig. 4.21).

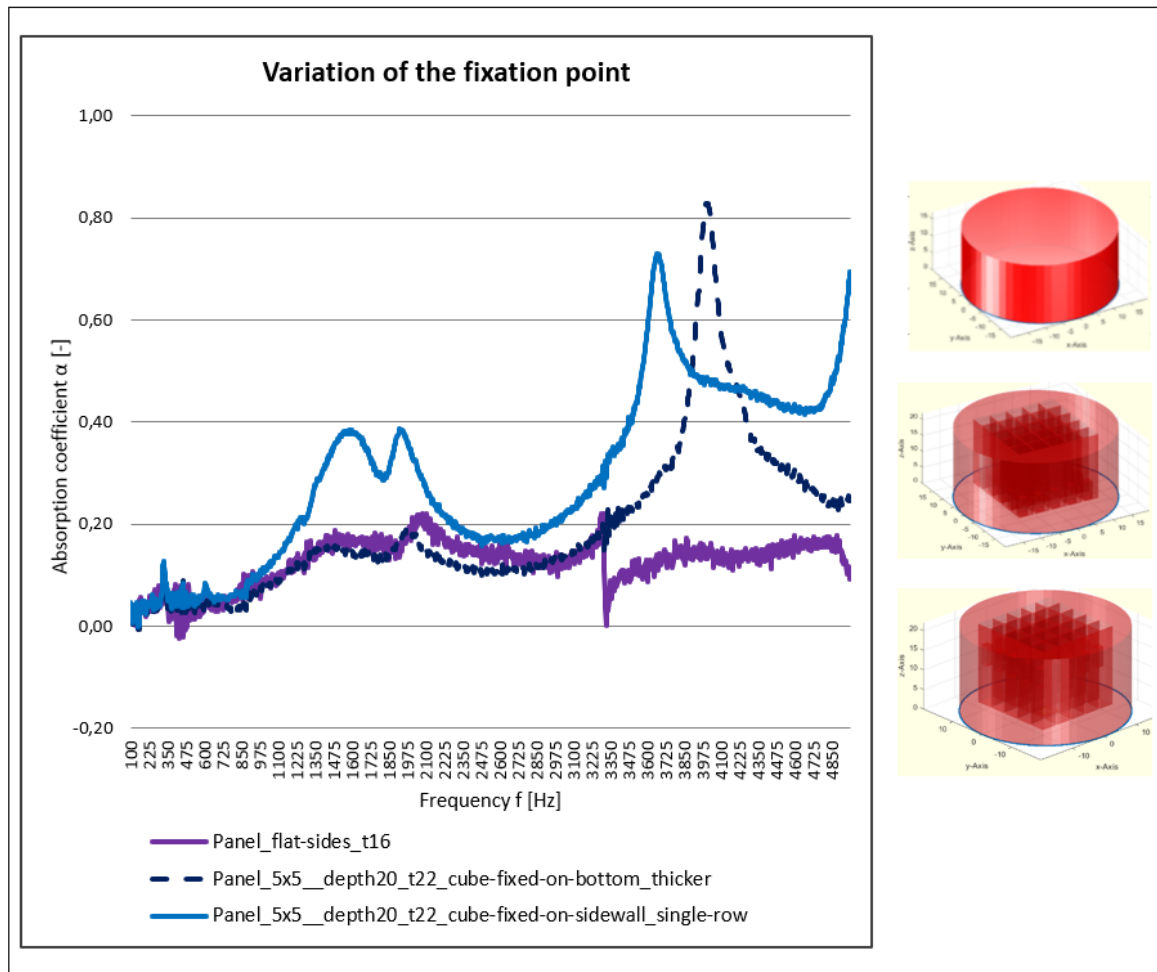


Figure 4.21: Variation of the fixation point

- **The maximum value of absorption**

The maximum absorption coefficient of $\alpha = 0.73$ is found at 3670 Hz for the prototype with side wall fixation and $\alpha = 0.83$ at 4000 Hz for the attachment on the bottom. Due to the great slope of the curve in the upper frequency range, the absorption coefficients determined with sidewall fixation increasingly exceed the measured values detected for floor connected resonant structures. This clearly shows that fixing a resonator of the same dimensions to the side wall instead of the floor significantly improves sound absorption.

- **The location and width of the peak**

As indicated by the graphs given in Fig. 4.21, attaching resonant bodies of the same geometry to the side wall instead of the bottom is accompanied by an increase in the absorption coefficients at almost all measured frequencies up to 5000 Hz. Especially in the lower frequencies between 1300 Hz and 2000 Hz the spacing between the two curves is up to 280 %. Only in the range from 3900 Hz to 4200 Hz the data points obtained for a fixation on the floor are higher than those obtained for a sidewall fixation.

Single-row and two-rowed resonators

Moreover, a prototype is designed whose cavities each contain two cuboids of the dimensions $2.00 \times 2.00 \times 2.50$ mm, which are attached to the inner sidewalls of the cavities at a distance of 2.50 mm from each other and at a distance of 12.00 mm from the cavity floor.

- **The maximum value of absorption**

The curve progressions of both designs tendentially show similarities, such as the occurrence of two peaks in the lower frequency range and the subsequent curve decrease. Moreover a renewed increase of the absorption coefficients to a maximum value with subsequent decrease in the higher frequency range is observed (see Fig. 4.22). However, both variants show distinctive differences in the height and location of the absorption coefficients. In the case of only one resonator in each cell, the absorption coefficients are higher than those achieved with double-row resonators. The two peaks are $\alpha = 0.39$ each at 1600 Hz and 1920 Hz in the case of one resonator. Inserting two resonators into the cells results in almost 60 % lower maximum values of $\alpha = 0.17$ at 1550 Hz and $\alpha = 0.21$ at 1980 Hz.

The difference between the two prototypes is also obvious by considering the measurement data for a higher frequency range. The highest absorption coefficients achieved with a single resonator are $\alpha = 0.73$ at 3670 Hz. In contrast, if two resonators are inserted, a peak of $\alpha = 0.74$ at 3575 Hz is detected. The heights of the maximum values therefore hardly differ from one another, but the distance between the curves increases significantly, especially after the peak values. Whereas for the prototype with a single-row resonator, absorption coefficients of at least $\alpha = 0.4$ are still measured, and from about 4800 Hz on, again increasing absorption coefficients are registered, the curve drops sharply when two resonant bodies are inserted into the cells.

As shown in Fig. 3.1b, the double-row resonators are regarded as a mass-spring system consisting of two identical masses m_1 and m_2 but two different spring stiffnesses D_1 and D_2 . Whereas the resonator with mass m_1 is influenced by the spring stiffness D_1 , the resonant body with mass m_2 is affected by the spring stiffnesses D_1 and D_2 . Thus, the resonant frequency is increased as can be seen in the curves shown in Fig. 4.22.

- **The location and width of the peak**

The frequency width around the two peaks in the low frequency range of the two prototypes hardly differs from each other. In contrast, the frequency band around the maximum absorption coefficient in the higher frequency range is significantly wider for the plate with single-row resonators than for a double-row resonator arrangement.

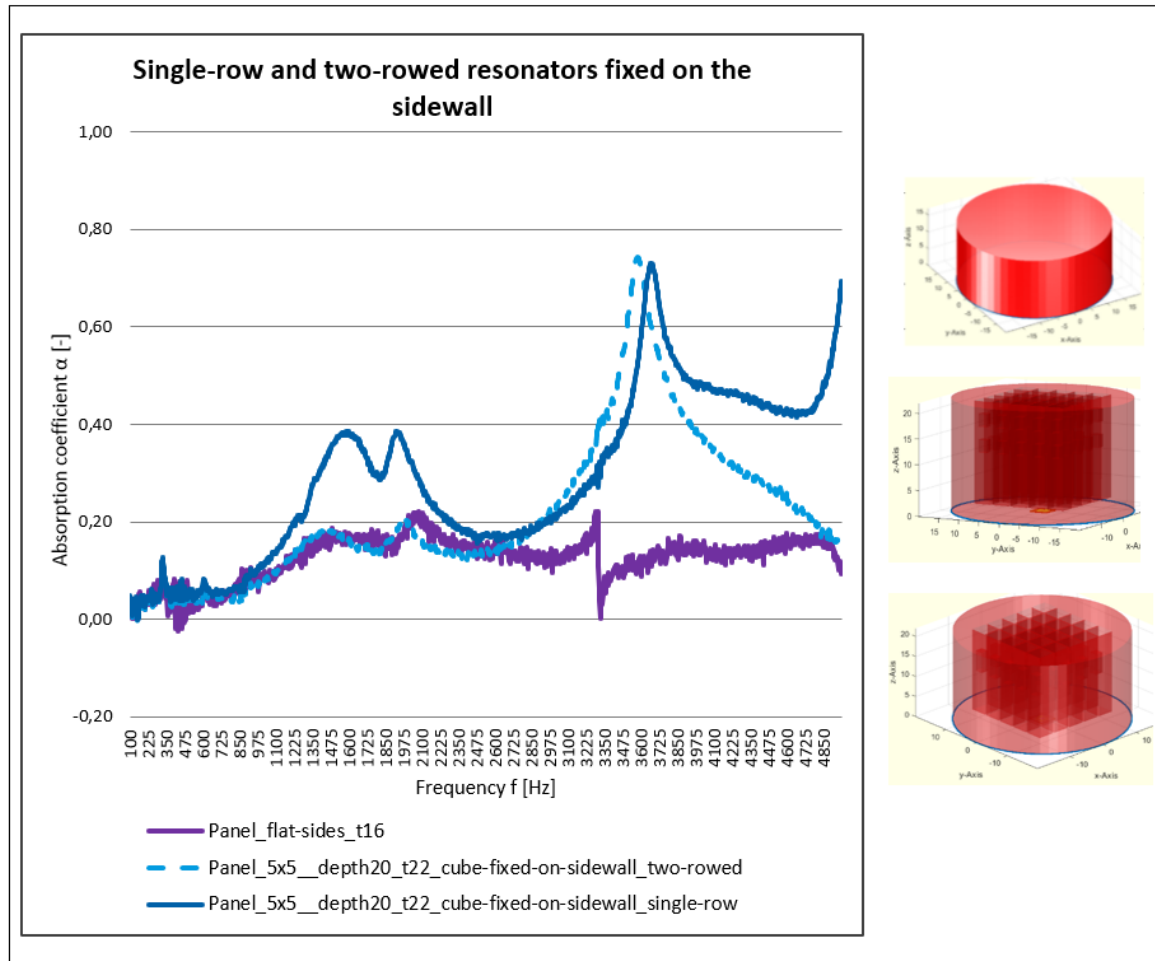


Figure 4.22: Single-row and two-rowed resonators fixed on the sidewall

Combination of different resonators

Furthermore, a prototype with cuboid cavities arranged in a 5×5 lattice structure including two different variants cuboid resonators is created. 13 resonators of the dimensions $1.00 \times 1.00 \times 20.00$ mm and 12 resonant structures of size $2.00 \times 2.00 \times 5.00$ mm are embedded in the voids and are alternately attached to the bottom or the inner side surfaces. Fig. 4.23 illustrates the measured sound absorption coefficients over the frequency range considered up to 5000 Hz for the panels with resonators of the dimensions $1.00 \times 1.00 \times 20.00$ mm or $2.00 \times 2.00 \times 5.00$ and of the prototype with checkerboard patterns, respectively.

The combination of the two resonator geometries causes the sound absorption to deteriorate, especially in the lower and upper frequency range. Depending on the geometry, the sound absorption is influenced in a specific frequency range. Instead of a single peak, the curve of the combined model shows two maximum values that could be assigned to the influences of the two different resonator geometries. Reducing the number of resonators of each geometry to 12 or 13 bodies each instead of 25 resonators of one design, the maximum peaks of the resulting demonstrator are slightly smaller than the maximum values of the individual models. As the curves in Fig. 4.23 visualize, similar amounts of sound are absorbed in each case and therefore only slightly lower peaks are achieved when half of the resonant structures of a design is inserted into the cavities.

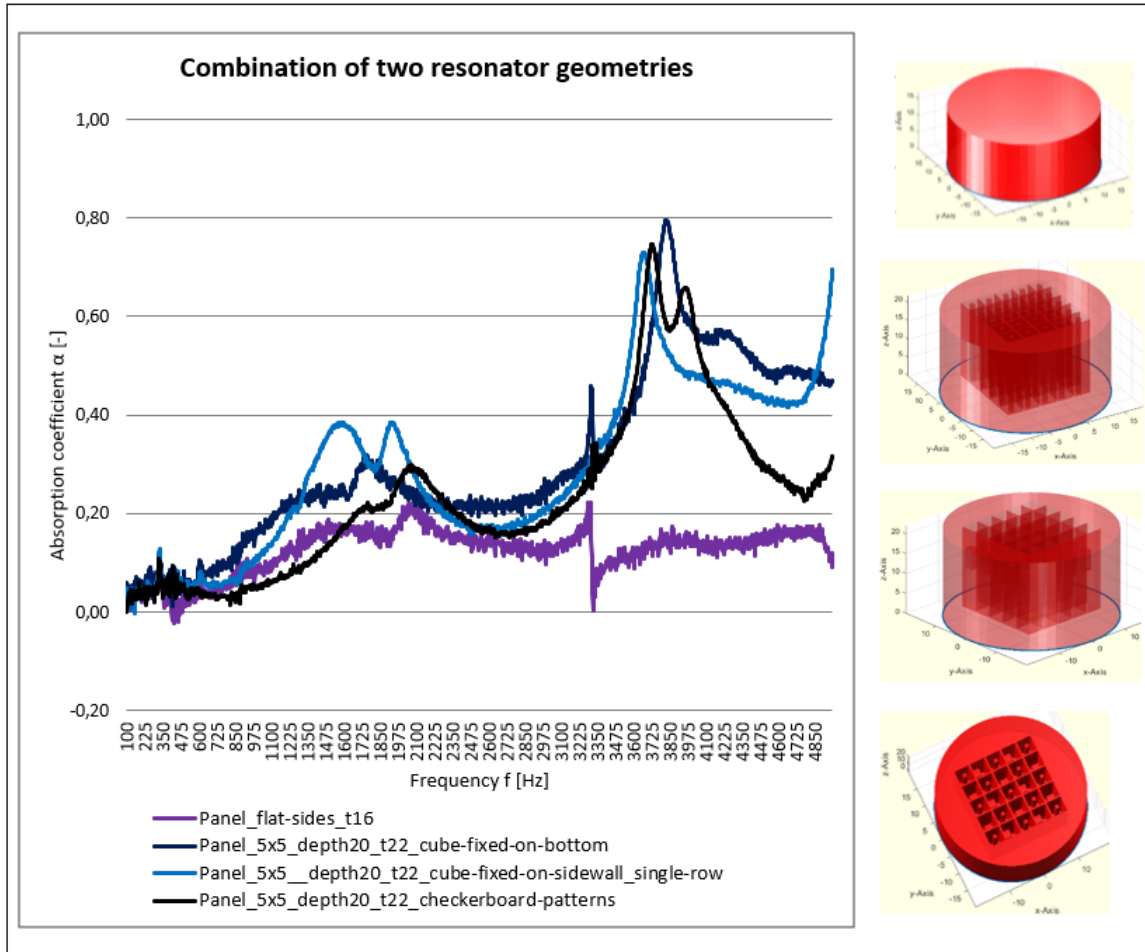


Figure 4.23: Combination of two resonator designs

4.2.5 Material

Besides varying voids and resonators, one investigates the effect of different materials on the sound insulation. Fig. 4.24 to 4.26 illustrate the difference between the materials "tough", with which one can build hard and durable objects and "casting", that is used to generate very smooth surfaces. The type of resin does not significantly influence the resonant frequencies if designs with cavities or with bottom fixed resonators are analysed. Since the slight shift of the maximum peak moves to lower as well as to higher frequencies, it may be assumed, that it is not caused by the material properties. A more conclusive explication for the curve progression might be inadequacies in construction flaws. In contrast, the maximum absorption coefficients of the panel with checkerbord patterns are lifted enormously when using casting material. Moreover, the curves for the prototypes clearly demonstrate, that sound absorption deteriorates in wide frequency ranges when the material casting is used. Due to unavailable information about the materials, a further analysis is not possible.

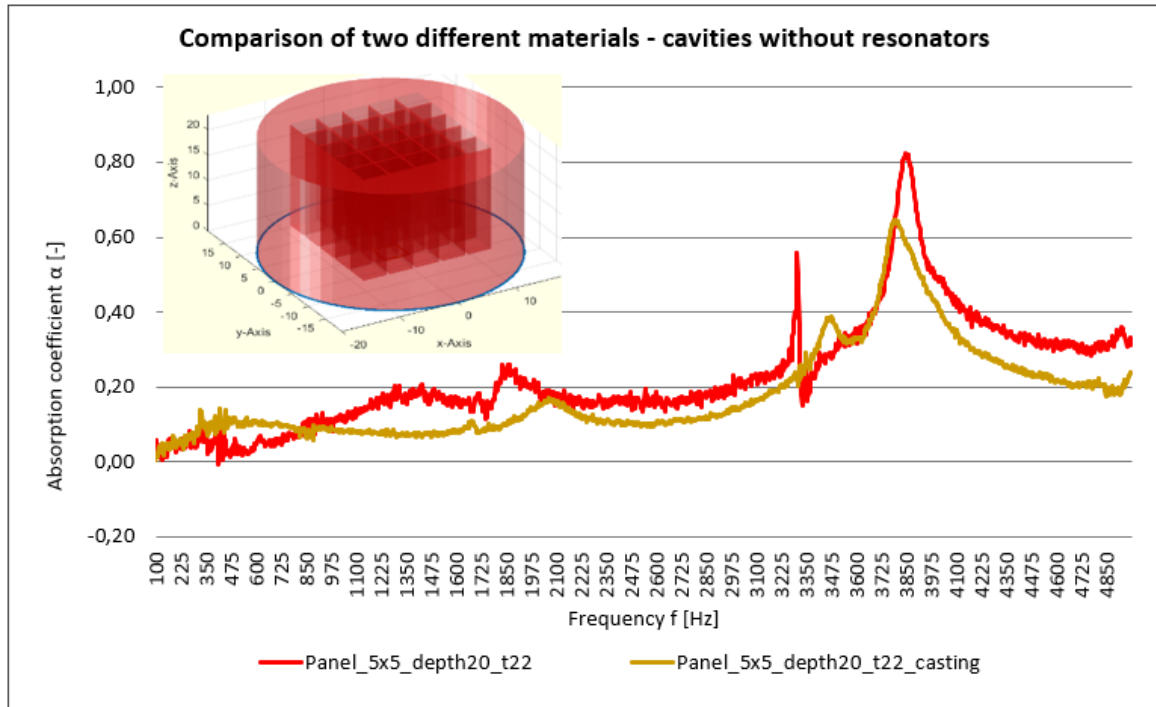


Figure 4.24: Comparison of prototypes of different materials

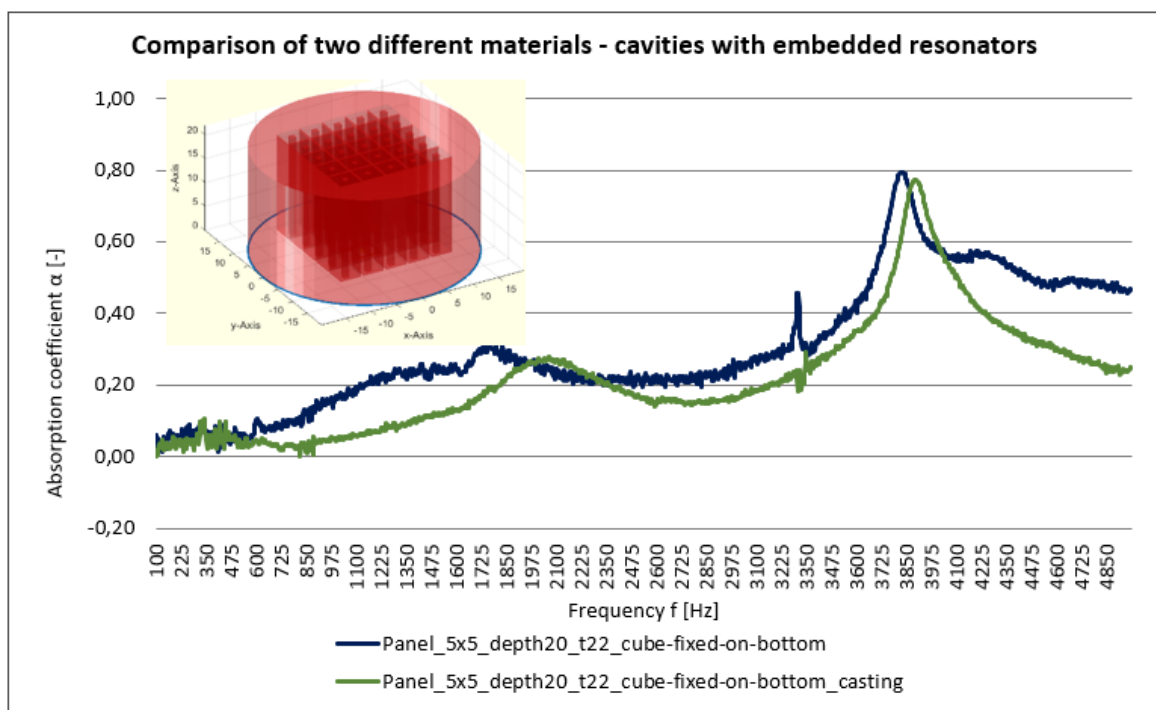


Figure 4.25: Comparison of prototypes of different materials

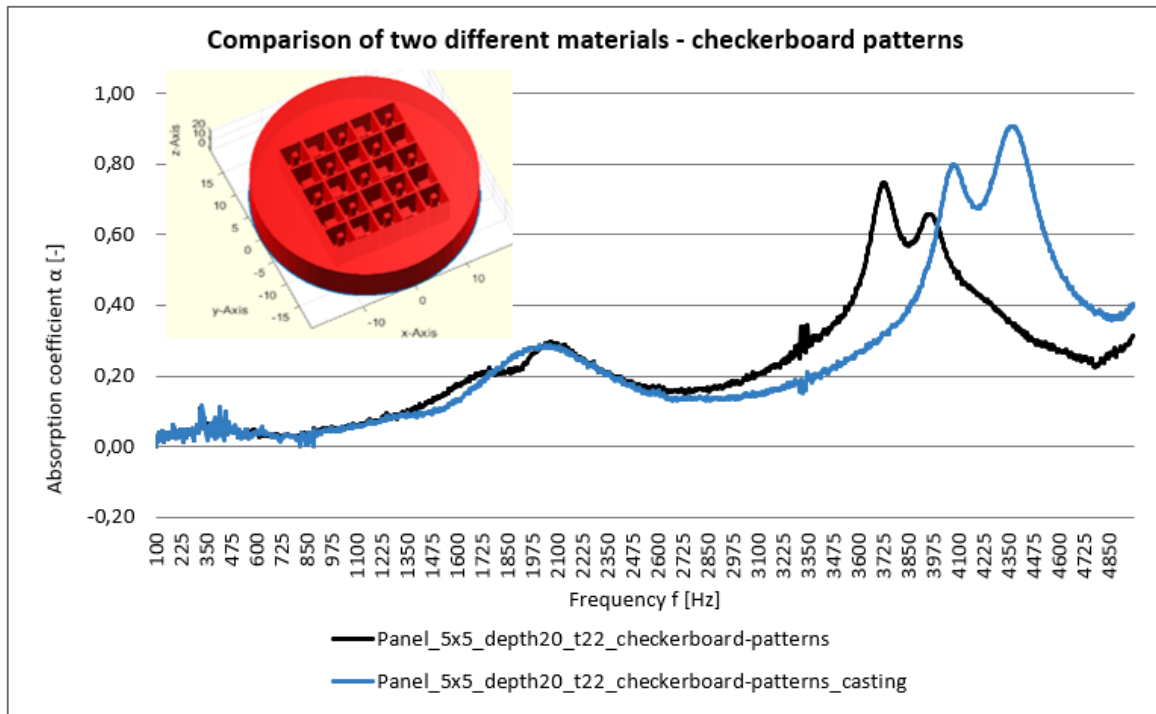


Figure 4.26: Comparison of prototypes of different materials

4.3 Optimal design of the panels

The results of the analysis of the measurement data regarding the influence of individual parameters on the sound-absorbing effect carried out in the above section form the basis for the optimisation of the panel design. The aim is to extend the frequency band and increase the maximum absorption coefficient without adversely affecting the weight of the prototypes. Investigated variations of the parameters were

- the addition of a bottom,
- the cavity size and number,
- the cavity depth and geometry,
- the addition of a resonant structure to a lattice host structure,
- the resonator design,
- the fixation point of the resonator and
- the material.

The main findings to be considered for optimizing the design of the panel are

- the shift of the natural frequency to higher frequencies with reduction of the cavity depth,
- the decrease of the absorption coefficients by removing the soil under the cavities,
- the shift of the natural frequency to higher frequencies with increasing matrix size and reducing cavity footprints,
- the widening of the band gap to higher frequencies with increasing matrix size and

- decreasing the base areas of cavities,
- the shift of the natural frequency to higher frequencies with reduction of the height and enlargement of the base area of the resonator geometry,
 - the improvement or deterioration of sound absorption by adding a resonator in cuboid or cylindrical cavities,
 - the improvement of sound absorption by adding resonators to the side walls of the voids,
 - the deterioration of the sound absorption by attaching two resonators to the side walls of the cavities,
 - the low influence of the use of another resin and
 - the occurrence of two natural frequencies by combining two different resonator geometries.

4.4 Limits of the measurement technology

Due to the small geometry of test specimens, the natural frequencies and ranges in which sound is absorbed are so high that they could not be detected by the impedance tube. It is therefore essential to increase the detection zone of the acoustic impedance tube to determine the sound-reducing properties of acoustic metamaterials. Thus, in order to comprehensively investigate the created panels, a measuring device with a frequency range, that allows the detection of all absorption coefficients of a panel is required.

5 Design and measurement of acoustic enclosures

After the experimental study of the panels by determining the absorption coefficients using an acoustic impedance tube, the following chapter presents prototypes, which qualitatively demonstrate the effectiveness of the acoustic metamaterial in terms of sound reduction. For this purpose, acoustic enclosures are designed and their sound pressure levels are determined experimentally.

5.1 The design of the acoustic enclosures

Whereas the influence of individual geometric parameters on sound absorption was investigated by measuring the absorption coefficients of the plates, this chapter presents a prototype that qualitatively demonstrates the effectiveness of the acoustic metamaterial. For this purpose, an acoustic enclosure open to one side is built. The prototype consists of five flat side walls with the dimensions $60.00 \times 60.00 \times 5.00$ mm (see Fig. 5.1b).

In addition to this basic design, two further variants are created, whereby the design of these acoustic enclosures is based on the measurement results of the panels. Improvements in sound absorption were achieved in particular for the *Panel_5 × 5_depth20_t22_cube – fixed – on – bottom* (see Fig. 5.1a). Thus the design of this panel is used to create an acoustic enclosure with cavities in the side walls and another prototype with additional resonators embedded in the voids. The thickness of the side surfaces of these two acoustic enclosures depends on two factors. To measure the sound pressure levels, the acoustic enclosures are placed over a small loudspeaker, whose outer dimensions define the inner dimensions of the acoustic enclosures. The outer dimensions of the prototype of 60.00 mm are limited by the size of the installation space of the 3D printer. This results in a wall thickness of 7.25 mm for the individual side surfaces.

The design of the unit cells of the acoustic enclosures is based on the unit cells of the *Panel_5 × 5_depth20_t22_cube – fixed – on – bottom*. 100 cavities with the dimensions $4.00 \times 4.00 \times 5.25$ mm are inserted into each of the five side surfaces in a 10×10 matrix. The resulting prototype is shown in Fig. 5.1c. In a further variant, resonators with the dimensions $1.00 \times 1.00 \times 5.25$ mm are attached to the bottom of the cavities. Thus three prototypes are created, whose sound pressure levels are determined experimentally.

5.2 Measurement setup for determining the sound pressure level L_p

To determine the influence of the acoustic enclosures on the acoustic wave propagation, one uses a test configuration similar to the setup developed by Claeys et al. (Claeys et al., 2016) The measurement setup basically consists of a loudspeaker and a sound level meter (see Fig. 5.2). The speaker from dodocool® is controlled via bluetooth with the app Frequency Sound Generator® from LuxDeLux® with a smartphone and is placed in a wooden box with the dimensions $100.00 \times 100.00 \times 65.00$ mm and noise insulating properties. The loudspeaker can generate signals up to 15000 Hz (Dodocool, n.d.), which pass through a round opening milled into the upper surface of the box. The sound is then detected by the sound level meter

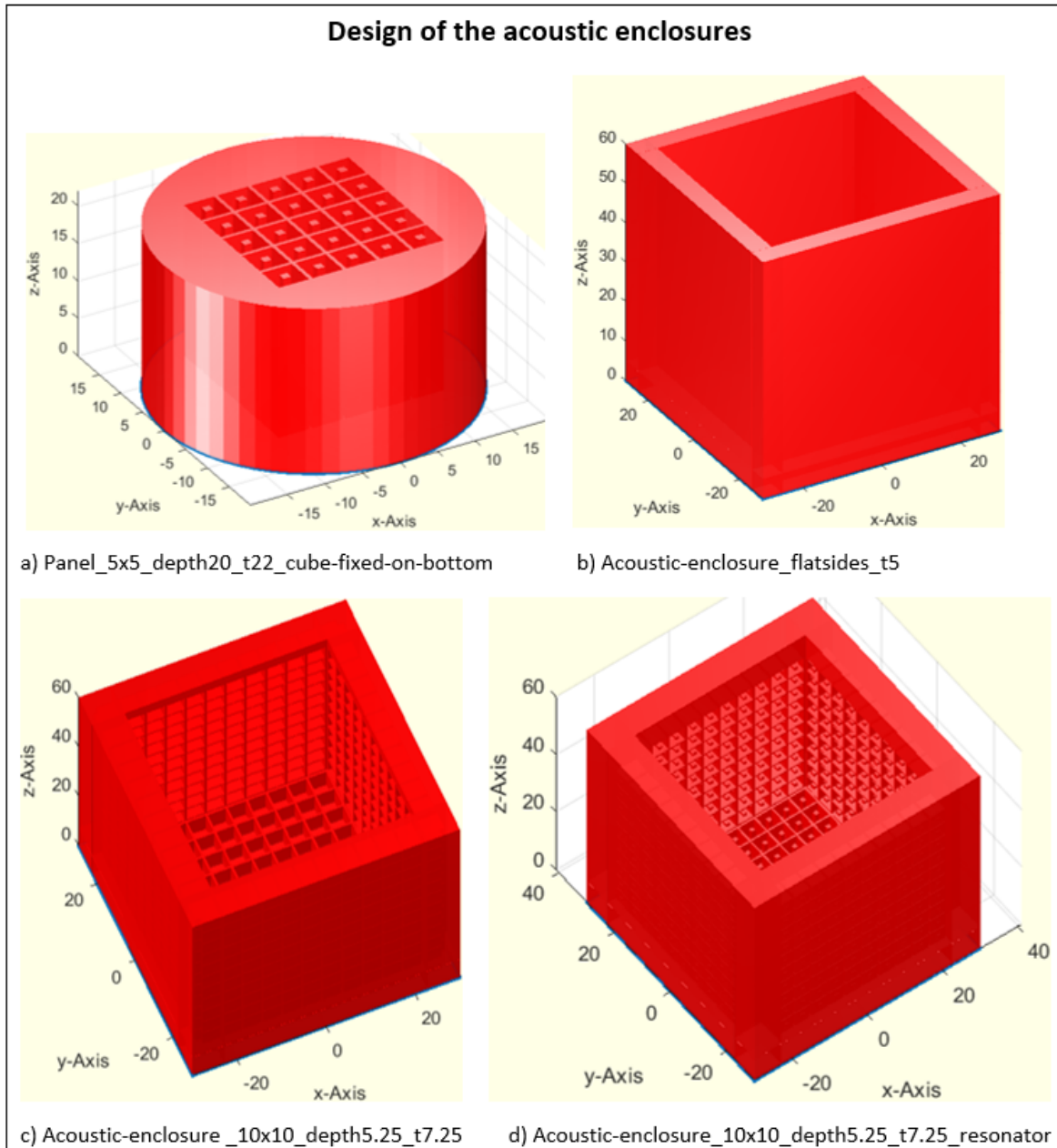


Figure 5.1: Development of acoustic enclosures

MK09[®] from Meterk[®], that is mounted in a distance of 50.00 mm in vertical direction and of 100 mm in horizontal direction of the upper center of the loudspeaker as shown in Fig. 5.2. In contrast to the acoustic impedance tube, the sound level meter can only measure sound pressure levels in the time domain. It is not possible to measure sound pressure levels in a frequency spectrum.

The data acquisition is conducted for ascending and descending order of frequencies in a range from 14000 Hz to 15000 Hz. The upper limit is set because the frequency range of the loudspeaker ends with 15000 Hz and the lower limit, in turn, is defined by the location of the theoretically calculated natural frequency of the cavities of 16334 Hz according to Eq. 4.2.

In a first step, no enclosure is put over the source and the sound pressure level $L_{p_without}$ is



Figure 5.2: Bluetooth speaker from dodocool®, sound level meter MK09® from Meterk® and loudspeaker box

(Dodocool, n.d.) (Meterk, n.d.)

determined for this situation. If no acoustic enclosure is placed above the loudspeaker, the measurement results are marked with the index "without". Then, one after the other, the acoustic enclosures are placed over the loudspeaker to measure the sound pressure levels for each demonstrator. The results determined for the prototypes are clearly described by the respective name of the model. To evaluate the effectiveness of the acoustic enclosures in noise insulation, one compares the measured sound pressure levels $L_{p_without}$ without and with enclosure. The effectiveness of the demonstrators in noise reduction is then derived from the ratio of the two sound pressure levels as follows

$$\text{Degree of noise reduction} = \frac{L_{p_without}}{L_{p_with}} . \quad (5.1)$$

5.3 Analysis of the measurement data

Based on three created variants, there are four situations in which the sound pressure levels are to be measured. These are sound pressure levels

1. without enclosure (see Fig. 5.3a),
2. with an acoustic enclosure with flat side surfaces (see Fig. 5.3b),
3. with an acoustic enclosure with cavities arranged in a 10×10 matrix (see Fig. 5.3c) and
4. with an acoustic enclosure with cavities with embedded resonant structures arranged in a 10×10 matrix (see Fig. 5.3d).

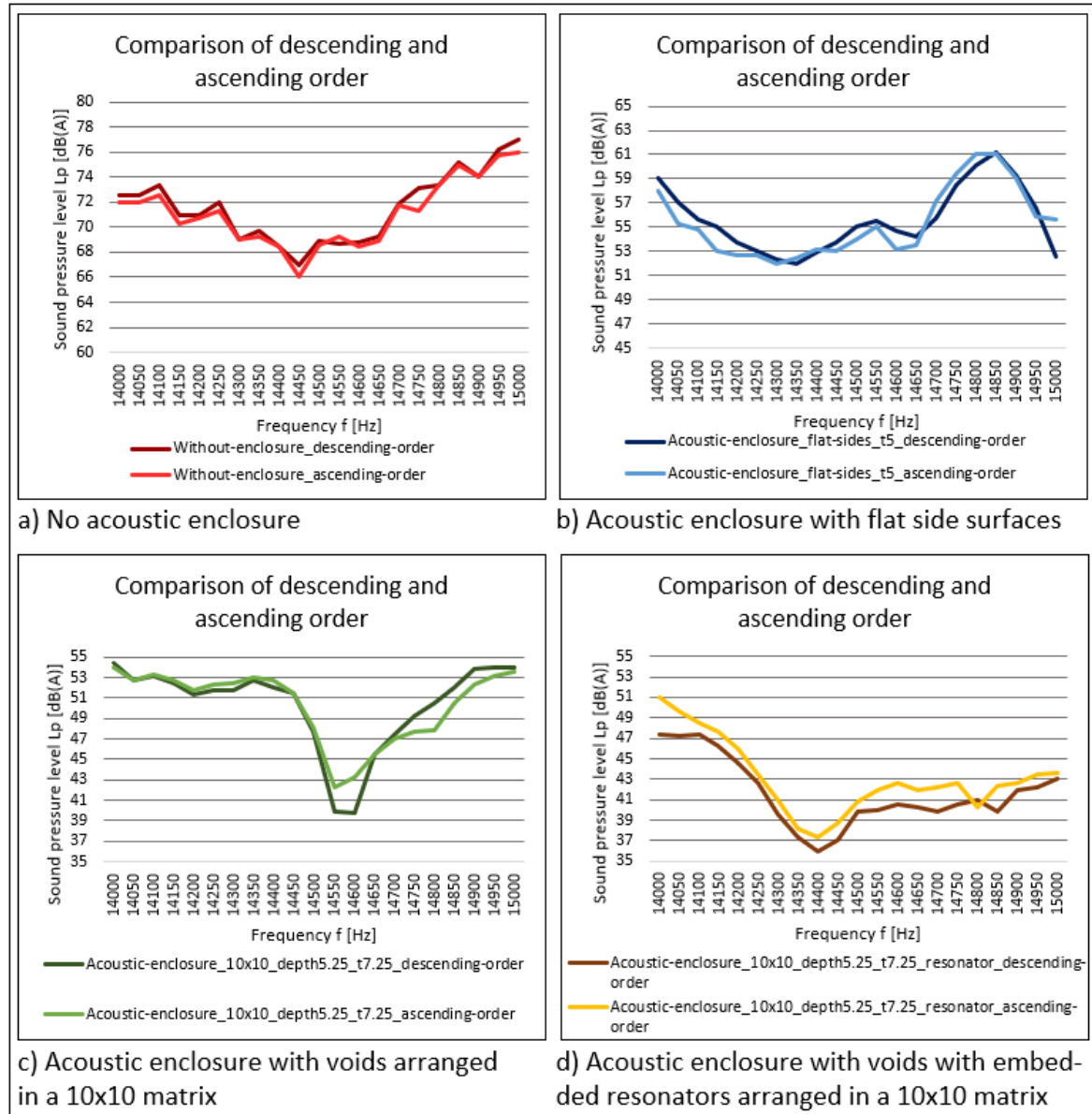


Figure 5.3: Comparison of measurement data for ascending and descending order

As the previous analysis of the measurement data in Chap. 4 show, the actual resonance frequencies are lowered by some hertz. Thus, one extends the considered range to 14000 Hz. Sound levels in the lower frequencies are filtered out since it was not possible to give conclusive explanations of the measured data, which were detected below the resonance frequencies as regards the panel designs. Due to the fact, that the theoretical natural frequency is significantly higher than the detectable range, it can be expected that the presented measurement data in Fig. 5.3 do not show the sound levels in the area around the resonance frequency and thus do not reflect the maximum potential of the acoustic enclosures in noise reduction.

The sound pressure levels determined for the situation in which no acoustic enclosure is placed over the sound source are significantly higher than the sound pressure level of ambient noise, which is about 30 dB to 40 dB. Thus, the accuracy of the measured data is proven and a distorting influence by background noise is excluded. (Bayerisches Landesamt für Umwelt, 2017)

To determine the reliability of the measurement technology to collect the same measured values, the sound pressure levels are collected in ascending and descending order. For this purpose, the measuring range from 14000 Hz to 15000 Hz is scanned in 21 steps with a distance of 50 Hz each. As demonstrated by the curves shown in Fig. 5.3, only small deviations between ascending and descending order occur. In the following, each measured value is approximated by the averages of the data of these two measurement series. In addition, the averaged values of the states with an acoustic enclosure are related to the averaged data, that are determined without enclosure. The consequent degree of noise reduction is illustrated in Fig. 5.4a.

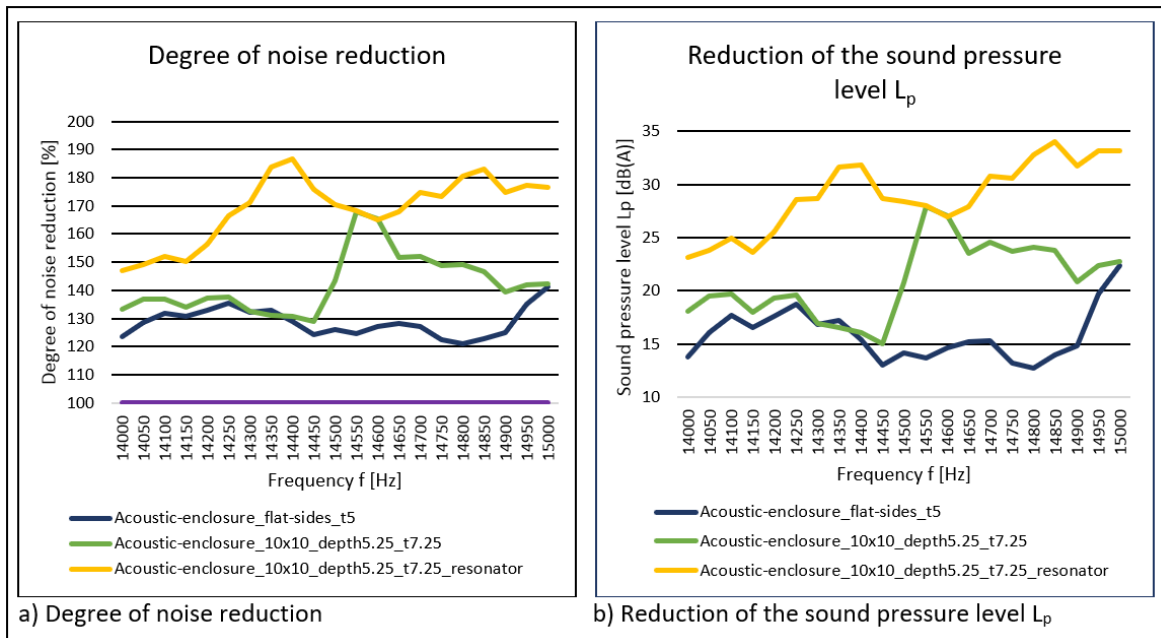


Figure 5.4: Comparison of acoustic enclosures

Compared to the state without enclosure (violet curve), the addition of an acoustic enclosure improves the noise reduction. It can be inferred from the curve positions, that acoustic enclosures with flat side surfaces increase the degree of enhancement by at least 20 % in the regarded frequency range (blue curve). Moreover, the prototype whose inner side surfaces are designed as hollow voids exalts this effect in wide frequency ranges. For this acoustic enclosure a degree of noise reduction between 29 % and 68 % is achieved (green curve). The lowest sound levels in all frequency ranges are determined for the prototype with added resonators (yellow curve), as can be seen by a degree of noise reduction between 46 % and 87 %.

Another illustration of the differences between the sound pressure levels determined without acoustic enclosure and the sound pressure levels of the three demonstrators is given in Fig. 5.4b. The use of an acoustic enclosure with smooth sides results in a reduction of the sound pressure levels by at least 12 dB (blue curve). According to Fig. 5.5, the sound power is thus reduced by a factor of 16 and the volume is more than halved. If the prototype with cavities arranged in a 10×10 matrix is used, the reduction of the sound pressure levels is between 15 dB and 28 dB. For the acoustic enclosure with additionally embedded resonant structures, sound pressure level reductions between 28 dB and 34 dB are measured. The volume is thus reduced by three to seven times and by seven to ten times of the original value respectively.

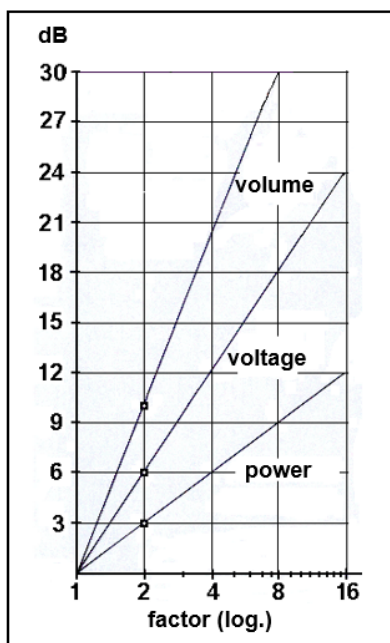


Figure 5.5: Correlation between sound pressure level and sound power
(Sengpielaudio, n.d.)

5.3.1 Limits of the measurement technology

The measurements have shown that the measuring range of the sound level meter is too small to detect the sound pressure levels in the relevant frequency ranges. As the geometries of the test specimens are very small, the frequency ranges in which sound absorption occurs are also very high. For more detailed investigations a measuring instrument with a wider detectable frequency range is required.

6 Summary and outlook

6.1 Summary of results

Due to the demand for quiet products from customers and legislation, the acoustic behavior of products is increasingly important in product development. The acoustic metamaterial concept has proven to be a suitable method to reduce the sound emission of products.

In the present work, various prototypes are created, which exhibit a periodic arrangement of unit cells in which resonators are inserted. Basically, the test specimens are designed as panels or acoustic enclosures. By varying design parameters, 21 variations of the panels and three variants of acoustic enclosures are built. To create the 3D models the Matlab toolbox SG-Library® is used, which was developed by the Chair of Micro Technology and Medical Device Technology led by Professor Lüth at the Technical University of Munich. The demonstrators are built with the 3D printer Prusa SL1®, which works according to the principle of stereolithography. Before the objects can be used, they are post-processed mechanically with the Curing and Washing Machine® and finished manually with sandpaper.

In the experimental determination of the acoustic properties of the created metamaterial structures, an acoustic impedance tube is used to measure the absorption coefficients of the panels. The sound pressure levels of the acoustic enclosures are measured with a sound level meter. After measuring physical quantities, the effectiveness of resonance based metamaterials is discussed. The focus is on the investigation of the sensitivity change of the prototypes to their sound absorption capacity by varying geometric parameters. Hypotheses for causes of the obtained measurement data can be formulated and based on the experimental results proposals for optimizing the panels can be carried out. Improvement objective criterions are the extension of the band gap, the increase in the absorption coefficient and the reduction of the sound pressure level respectively without deterioration of the mass of the prototypes.

6.2 Outlook

In the following, challenges are presented which have arisen in the course of the investigation of the prototypes. These tasks include aspects such as the variation of parameters during model generation without prior knowledge of the degree of influence of geometric variables on the absorption coefficient, secondly the building of a too small number of samples for a statistical evaluation and thirdly an inadequate measuring technique due to a too small measuring range. Since these challenges were not addressed within the framework of the task due to lack of time, lack of measurement technology, lack of budget or because it was not part of the scope of work, it is recommended to deal with these aspects in a subsequent work.

6.2.1 Statistical evaluation based on a representative sample size and composition

As a well-founded explanation of the absorption coefficients of the different panels was not possible on the basis of the available measurement data, only assumptions regarding possible

causes for the obtained curves were made. Whereas only one design of each model was available for experimental investigation, a design in quadruplicate was produced to investigate the reproducibility of the objects and the repeatability of the measurement data. As the number of measuring bodies was too small for statistical evaluation, it is recommended to manufacture and measure a representative quantity of demonstrators in order to be able to derive reliable conclusions about the sound-reducing effect.

In addition to the production of a representative number of specimens, the selection of the sample composition is of decisive importance in order to perform a parameter study. By means of simulation different models can be created quickly. Furthermore, absorption coefficients can be simulated and the simulation results can be used for comparison with experimental measurement results. When evaluating experimentally collected measurement data, limitations such as manufacturing inaccuracies and the limits of the measurement technology used, i.e. the detectable measurement range, make it difficult to formulate clear results. In fact, only assumptions could be made about the extent to which parameters influence sound absorption of the prototypes. Although, the presented hypotheses were derived from physical laws, the validity of the assumptions needs to be examined. For this purpose, the collected data can be compared with simulations of the models. If both results show a high degree of correlation, the correctness of the experimentally determined quantities and thus the hypotheses can be verified.

6.2.2 Analysis of the influence of the resonant structures on noise reduction

The measurement data determined for prototypes without resonant structures could only be described on the basis of hypotheses. Thus, it was all the more difficult to interpret the curves for test objects with inserted resonators. Fig. 6.1 illustrates the models of two prototypes, one of which contains cavities arranged in a matrix form and the other consists of a plate on which 25 resonators are mounted in a 5×5 grid in the x-y-plane.

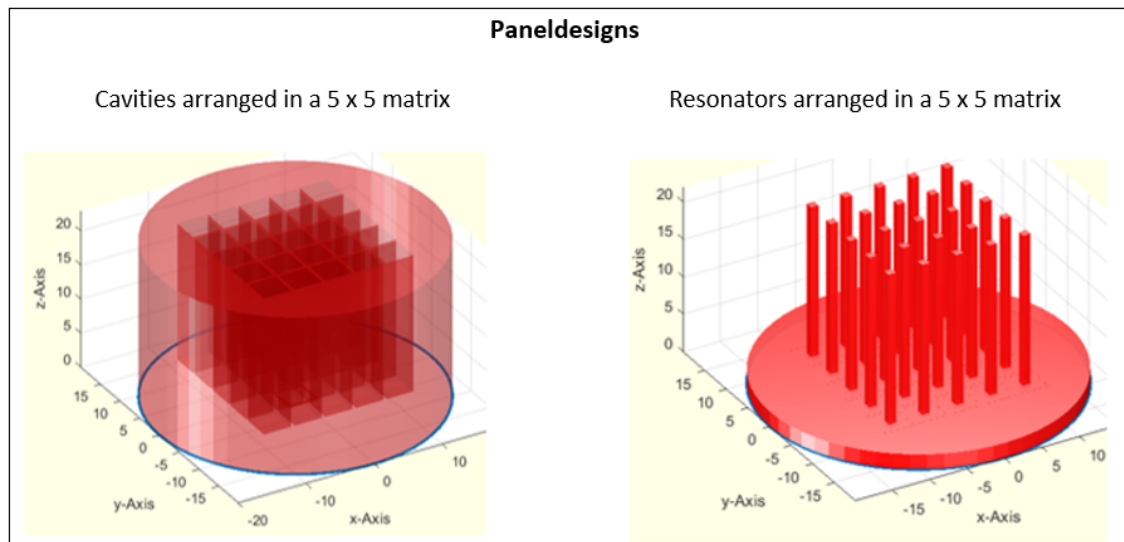


Figure 6.1: Analysis of the cavities and the resonators

The test specimen shown on the left and the combination of the two models presented in Fig. 6.1 is examined in the present work. However, no experimental investigation of the prototype

shown in the right image in Fig. 6.1 was carried out. Thus, it is recommended to measure separately prototypes with and without resonant bodies in the cells in order to determine the respective physical effects and their interactions.

6.2.3 Analysis of the influence of the material properties on sound absorption

Since the absorption coefficients could not be physically explained in wide frequency ranges, only assumptions about causes were given. One hypothesis in this respect was that the prototypes, regardless of their geometric design, absorb sound only due to their material properties. In order to verify this presumption, the prototypes could be made of a material that completely reflects sound due to its composition. If the same measurement data were obtained for prototypes made of the resin used in this case and of a totally reflecting material, this could serve as proof that sound absorption in the prototypes is not caused by the material properties but by their geometric shape.

7 References

- Acatech (Ed.). (2016). *Additive fertigung* (first edition ed., Vol. 64). Deutsche Akademie der Technikwissenschaften and Nationale Akademie der Wissenschaften Leopoldina and Union der deutschen Akademien der Wissenschaften.
- AED, A. E. D. (Ed.). (n.d.). *Bedienungsanleitung - bestimmung des schallabsorptionsgrades nach din en iso 10534-2.*
- AED, A. E. D. (2019). *Impedanzrohr acoustitube.* Retrieved from <https://www.akustikforschung.de/produkte/messgeräte/impedanzrohr-aed-1000-acoustitube/> (cited on 16.11.2019)
- Al-Zubi, M., Ayorinde, E., Witus, G., Dundar, M., Warriach, M., & Murty, Y. (2013). Vibro-acoustic characterization and optimization of periodic cellular material structures (pcms) for nvh applications. *Journal of Materials Science Research*, 2(4), 64.
- Amado-Mendes, P., Godinho, L., Dias, A. B., Amaral, P., & Pinho, N. (2018). A numerical study on the behavior of partition panels with micro-resonator-type metamaterials. *FIA 2018/TecniAcustica 2018.*
- Bayerisches Landesamt für Umwelt, L. (Ed.). (2017). *Laerm - hoeren, messen und bewerten.* Retrieved from https://www.lfu.bayern.de/buerger/doc/uw_34_laerm_messen_bewerten.pdf (cited on 04.03.2020)
- Bruenglinghaus, C. (2013). *Klangspiele - sound, nvh und akustik.* Retrieved from <https://www.springerprofessional.de/fahrzeugtechnik/klangspiele-sound-nvh-und-akustik/6561966> (cited on 11.03.2020)
- Brunnader, R. (2002). *Aufbau und programmierung der 2p messmethode im impedanzrohr für die messung akustischer materialparameter.* na.
- Chang, K.-J., Jung, J., Kim, H.-G., Choi, D. R., & Wang, S. (2018). *An application of acoustic metamaterial for reducing noise transfer through car body panels* (Tech. Rep.). SAE Technical Paper.
- Chen, H., Zeng, H., Ding, C., Luo, C., & Zhao, X. (2013). Double-negative acoustic metamaterial based on hollow steel tube meta-atom. *Journal of Applied Physics*, 113(10), 104902.
- Chen, S., Fan, Y., Fu, Q., Wu, H., Jin, Y., Zheng, J., & Zhang, F. (2018). A review of tunable acoustic metamaterials. *Applied Sciences*, 8(9), 1480.
- Claeys, C., Deckers, E., Pluymers, B., & Desmet, W. (2016). A lightweight vibro-acoustic metamaterial demonstrator: Numerical and experimental investigation. *Mechanical systems and signal processing*, 70, 853–880.
- Claeys, C., et al. (2018). Lightweight nvh solutions based on vibroacoustic metamaterials: example of a thermoformed panel. In *International workshop on metamaterials, date: 2018/06/06-2018/06/06, location: fraunhofer ibp stuttgart.*
- Claeys, C., Vergote, K., Sas, P., & Desmet, W. (2013). On the potential of tuned resonators to obtain low-frequency vibrational stop bands in periodic panels. *Journal of Sound and Vibration*, 332(6), 1418–1436.
- Craster, R. V., & Guenneau, S. (2012). *Acoustic metamaterials: Negative refraction, imaging, lensing and cloaking* (Vol. 166). Springer Science & Business Media.
- DEGA, D. G. f. A. e. (2006). *Akustische wellen und felder.* Retrieved from https://www.dega-akustik.de/fileadmin/dega-akustik.de/publikationen/DEGA_Empfehlung_101.pdf (cited on 16.12.2019)

- Deymier, P. A. (2013). *Acoustic metamaterials and phononic crystals* (Vol. 173). Springer Science & Business Media.
- DIN, E. (2001). 10534-2: Akustik-bestimmung des schallabsorptionsgrades und der impedanz in impedanzrohren-teil 2: Verfahren mit übertragungsfunktion (iso 10534-2: 1998). *Deutsche Fassung EN ISO, 10*, 534–2.
- Dodocool. (n.d.). *dodocool bluetooth lautsprecher*. Retrieved from [https://www.amazon.de/dodocool-Bluetooth-Lautsprecher-Freisprecheinrichtung-Shutter-Taste/dp/B01ITEG0YI/ref=asc_df_B01ITEG0YI/?tag=googshopde-21&linkCode=df0&hvadid=308837231229&hvpos=1o3&hvnetw=g&hvrand=16869718184048877085&hvpone=&hvptwo=&hvqmt=&hvdev=c&hvdvcndl=&hvlocint=&hvlocphy=9042518&hvtargid=pla-563057345519](https://www.amazon.de/dodocool-Bluetooth-Lautsprecher-Freisprecheinrichtung-Shutter-Taste/dp/B01ITEG0YI/ref=asc_df_B01ITEG0YI/?tag=googshopde-21&linkCode=df0&hvadid=308837231229&hvpos=1o3&hvnetw=g&hvrand=16869718184048877085&hvpone=&hvptwo=&hvqmt=&hvdev=c&hvdvcndl=&hvlocint=&hvlocphy=9042518&hvtargid=pla-563057345519&psc=1&th=1&psc=1&tag=&ref=&adgrpid=67008808772&hvpone=&hvptwo=&hvadid=308837231229&hvpos=1o3&hvnetw=g&hvrand=16869718184048877085&hvqmt=&hvdev=c&hvdvcndl=&hvlocint=&hvlocphy=9042518&hvtargid=pla-563057345519) (cited on 07.01.2020)
- Dong, H.-W., Zhao, S.-D., Wei, P., Cheng, L., Wang, Y.-S., & Zhang, C. (2019). Systematic design and realization of double-negative acoustic metamaterials by topology optimization. *Acta Materialia*, 172, 102–120.
- Guild, M., Rohde, C., Tothko, M., & Sieck, C. (2018). 3d printed acoustic metamaterial sound absorbers using functionally-graded sonic crystals. In *Proceedings of euronoise*.
- Gupfinger, H., Greisberger, H., Hasenhuettl, S., & Schweighofer, M. (n.d.). *wesentliche oekologische, soziale und oekonomische aspekte zur beurteilung von nachhaltigkeitsberichten*. Retrieved from <https://www.oegut.at/downloads/pdf/nh-berichterstattung-positionspapier.pdf> (cited on 11.03.2020)
- Gupta, A. (2014). A review on sonic crystal, its applications and numerical analysis techniques. *Acoustical Physics*, 60(2), 223–234.
- Haffke, D. (n.d.). *Laerm und laermSchutz - 5 grundlagen der laerminderung*. Retrieved from https://www.haufe.de/arbeitsschutz/arbeitsschutz-office/laerm-und-laermSchutz-5-grundlagen-der-laerminderung_idesk_PI957_HI731927.html (cited on 11.03.2020)
- Heinrich, S. M., & Dufour, I. (2015). Fundamental theory of resonant mems devices. *Resonant MEMS*, 26, 3–28.
- Hiebel, H. (2005). *Matlab-simulation unter berücksichtigung von mehrfachreflexionen*. Retrieved from https://www2.spsc.tugraz.at/www-archive/downloads/PA_Hiebel-Kundtsches_Rohr_mit_Mehrfachreflexion.pdf (cited on 16.01.2019)
- Hussmann, H. (n.d.). *Ton und klang*. Retrieved from http://www.medien.ifi.lmu.de/fileadmin/mimuc/dm_ws05/vorlesung/dm5a_2FpS.pdf (cited on 20.02.2020)
- International, A. (2019). (Tech. Rep.). Author.
- Just3DP (Ed.). (2016). *Fdm vs. sla*. Retrieved from <https://www.just3dp.com/blog/post/fdm-vs-sla/> (cited on 16.12.2019)
- Kimura, M., Kunio, J., Schuhmacher, A., & Ryu, Y. (2014). A new high-frequency impedance tube for measuring sound absorption coefficient and sound transmission loss. In *Inter-noise* (Vol. 312, p. 2014).
- Klages, G., & Stuart, H. (2010). Schwingungs-und wellenlehre, akustik. *Kurzes Lehrbuch der Physik*, 67–86.
- Kunio, J., Yoo, T., Jou, K., Bolton, J., & Enok, J. (2009). A comparison of two and four microphone standing wave tube procedures for estimating the normal incidence ab-

- sorption coefficient. In *38th international congress and exposition on noise control engineering* (pp. 1057–1065).
- Langfeldt, F. (2018). *Membrane-type acoustic metamaterials for aircraft noise shields* (Unpublished doctoral dissertation). Technische Universitaet Hamburg.
- Liu, Z., Zhang, X., Mao, Y., Zhu, Y., Yang, Z., Chan, C. T., & Sheng, P. (2000). Locally resonant sonic materials. *Science*, 289(5485), 1734–1736.
- Loefken, J. O. (2017a). *Metamaterial fuer ultraschall*. Retrieved from https://www.wissenschaft-aktuell.de/artikel/Metamaterial_fuer_Ultraschall_1771015590326.html (cited on 08.09.2019)
- Loefken, J. O. (2017b). *Origami gegen verkehrsraerm*. Retrieved from <https://www.weltderphysik.de/gebiet/technik/news/2017/origami-gegen-verkehrsraerm/> (cited on 21.03.2020)
- Lueth, T. (2019). *Sg-lib-matlab-toolbox*. Retrieved from <https://de.mathworks.com/matlabcentral/fileexchange/71951-sg-lib-matlab-toolbox> (cited on 06.12.2019)
- Lueth, T., Irlinger, F., et al. (2013). Berechnete erzeugung von dreidimensionalen oberflächenmodellen im stl-format aus der beschreibung planarer mechanismen für die generative fertigung durch selektives lasersintern. In *Kolloquium getriebetechnik: 10. kolloquium getriebetechnik* (pp. 267–284).
- McAlpine, K. (2019). *Researchers develop acoustic metamaterial that cancels sound*. Retrieved from <https://phys.org/news/2019-03-acoustic-metamaterial-cancels.html> (cited on 21.03.2020)
- Meterk. (n.d.). *Schallpegelmesser meterk*. Retrieved from https://www.amazon.de/Meterk-Schallpegelmesser-Schallpegel-LCD-Bildschrim-Hinterbeleuchtung/dp/B075591G4Q/ref=sr_1_5?__mk_de_DE=%C3%85M%C3%85%C5%BD%C3%95%C3%91&keywords=mk+09+sound+level+meter&qid=1581082646&s=ce-de&sr=1-5-catcorr (cited on 07.01.2020)
- Peters, S. (2018). Additive fertigung – der weg zur individuellen produktion. , 91.
- PrusaResearch (Ed.). (2019). *3d printing handbook*. Retrieved from https://cdn.prusa3d.com/downloads/manual/prusa3d_manual_s11_de_1_3.pdf#_ga=2.101673353.94666655.1582646140-822901726.1573646378 (cited on 01.12.2019)
- Richter, S., & Wischmann, S. (2016). Additive fertigungsmethoden–entwicklungsstand, marktperspektiven für den industriellen einsatz und ikt-spezifische herausforderungen bei forschung und entwicklung. Berlin, www.vdivde-it.de/publikationen/studien/additive-fertigungsmethoden/at_download/pdf (7.6. 2016).
- Ruettinger, R. (n.d.). *Din-normenausschuss werkstofftechnologie (nwt)*. Retrieved from <https://www.din.de/de/mitwirken/normenausschuesse/nwt/aktuelles/revision-der-grundlagennorm-din-en-iso-astm-52900-additive-fertigung-grundlagen-terminologie--277374> (cited on 07.12.2020)
- Ruiz, H., Claeyns, C., Deckers, E., & Desmet, W. (2016). Numerical and experimental study of the effect of microslits on the normal absorption of structural metamaterials. *Mechanical Systems and Signal Processing*, 70, 904–918.
- Sengpielaudio (Ed.). (n.d.). *Tontechnik-rechner-sengpielaudio*. Retrieved from <http://www.sengpielaudio.com/Rechner-pegelaenderung.htm> (cited on 04.03.2020)
- Shive, J. N., & Weber, R. L. (1993). Interferenz und interferometrie. In *Ähnlichkeiten in der physik* (pp. 101–114). Springer.

- Spektrum. (2011). *Tarnkappen fuer schall entwickelt.* Retrieved from <https://www.spektrum.de/news/tarnkappe-fuer-schallwellen-entwickelt/1115823> (cited on 05.08.2019)
- Spurk, N., Joseph und Aksel. (2010). *Strömungslehre: Einführung in die theorie der strömungen.* Springer-Verlag.
- Stuart, H. (1966). Schwingungs-und wellenlehre, akustik. In *Kurzes lehrbuch der physik* (pp. 63–82). Springer.
- Tretyakov, S., Urbas, A., & Zheludev, N. (2017). *The century of metamaterials.* Retrieved from https://eprints.soton.ac.uk/410976/1/The_century_of_metamaterials_NZ.pdf (cited on 29.08.2019)
- Van Belle, L., Claeys, C., Deckers, E., Pluymers, B., & Desmet, W. (2016). Enhanced lightweight nvh solutions based on vibro-acoustic metamaterials. In *Earpaforum 2016, date: 2016/10/19-2016/10/19.*
- Wang, X., Chen, Y., Zhou, G., Chen, T., & Ma, F. (2019). Synergetic coupling large-scale plate-type acoustic metamaterial panel for broadband sound insulation. *Journal of Sound and Vibration, 459*, 114867.
- Wanja, B. (2017). Aufbau und test eines lambda-viertel-resonators für das scanning positron microscope interface.
- Zhang, S. (2010). *Acoustic metamaterial design and applications* (Unpublished doctoral dissertation). University of Illinois at Urbana-Champaign.

8 List of Figures

Figure 1.1	Organization of the thesis	5
Figure 2.1	Analogy between acoustic and electromagnetic variables	7
Figure 2.2	Structure to influence the propagation of acoustic waves by Francisco Mesegue.....	7
Figure 2.3	Arrangement of scatterers in acoustic metamaterials	8
Figure 2.4	Acoustic metamaterial based on resonant structures	9
Figure 2.5	Acoustic metamaterial based on resonant structures and with interference-based stop bands.....	10
Figure 2.6	Demonstrators of acoustic metamaterials based on interference stop bands..	10
Figure 2.7	Demonstrators of acoustic metamaterials based on resonance stop bands....	11
Figure 2.8	Demonstrator of acoustic metamaterials combining interference and resonance stop bands	12
Figure 2.9	Applications of acoustic metamaterials	14
Figure 2.10	Partial steps of additive manufacturing	15
Figure 2.11	Classification of AM technologies according to materials und joining principle.....	17
Figure 2.12	Application types of additive manufacturing	18
Figure 2.13	Stereolithography	21
Figure 2.14	Power balance for sound waves at a barrier.....	22
Figure 2.15	Acoustic impedance tube with two microphones	24
Figure 2.16	Sound transmission tube with four microphones.....	26
Figure 2.17	Set-up for measuring the absorption and reflection coefficient.....	28
Figure 2.18	Set-up for measuring the sound transmsission loss.....	29
Figure 2.19	Set-up for sub-wavelenght imaging.....	30
Figure 2.20	Set-up for measuring the insertion loss	31
Figure 3.1	Hand-drawn sketch of an acoustic metamaterial	32
Figure 3.2	Mass-spring system of resonant structures	33

Figure 3.3	Designs of the panels - variated parameters.....	34
Figure 3.4	Panel designs - variation of cavity depth and geometry, grid size and number	35
Figure 3.5	Designs of the acoustic enclosures - variated parameters	36
Figure 3.6	Designs of the acoustic enclosures.....	37
Figure 3.7	Panel designs - variation of cavity depth and geometry, grid size and number	38
Figure 3.8	Panel designs - variation of the resonator design and fixation point	40
Figure 3.9	Resonant structures.....	41
Figure 3.10	3D printer Prusa SL1®	43
Figure 3.11	Curing and Washing Machine®	44
Figure 3.12	Manufacturing defects due to incorrect pressure settings	44
Figure 3.13	Prusa Slicer - Loading an object	45
Figure 3.14	Prusa Slicer - Moving an object.....	45
Figure 3.15	Prusa Slicer - Tilting an object	46
Figure 3.16	Resintank	47
Figure 3.17	Post-processing an object	48
Figure 3.18	Manufacturing inaccuracies due to resin residues in cavities	49
Figure 4.1	Structure of the AED 1000 - AcoustiTube Type 1®	51
Figure 4.2	Determination of the absorption coefficient α with the AED 1000 - Acousti-Tube Type 1®	52
Figure 4.3	Absorption coefficient α of a panel with flat sides and a thickness of 16.00 mm	54
Figure 4.4	Comparison of the reference measurements	55
Figure 4.5	Absorption coefficients α of all demonstrators	56
Figure 4.6	Comparison of panels with bottom, without bottom and with lattice edges ..	57
Figure 4.7	Variation of bottom thickness.....	59
Figure 4.8	Variation of grid size and number	60
Figure 4.9	Boundary layer in a pipe.....	61
Figure 4.10	Absorption coefficient α of <i>Panel_13 × 13_depth20_t22</i>	62
Figure 4.11	Reproduction of the same design	63

Figure 4.12 Variation of cavity depth.....	64
Figure 4.13 Variation of cavity geometry	65
Figure 4.14 Constructive and destructive interference.....	66
Figure 4.15 Variation of grid size and number of cylindrical cavities.....	67
Figure 4.16 Cuboid cavity with and without rectangular resonator	68
Figure 4.17 Influence of the cuboid resonator on the absorption coefficient α	69
Figure 4.18 Cylindrical cavity with and without rectangular resonator.....	70
Figure 4.19 Different rectangular resonator designs	71
Figure 4.20 Variation of the resonator design	72
Figure 4.21 Variation of the fixation point.....	73
Figure 4.22 Single-row and two-rowed resonators fixed on the sidewall	75
Figure 4.23 Combination of two resonator designs.....	76
Figure 4.24 Comparison of prototypes of different materials	77
Figure 4.25 Comparison of prototypes of different materials	77
Figure 4.26 Comparison of prototypes of different materials	78
Figure 5.1 Development of acoustic enclosures.....	81
Figure 5.2 Bluetooth speaker from dodocool [®] , sound level meter MK09 [®] from Meterk [®] and loudspeaker box	82
Figure 5.3 Comparison of measurement data for ascending and descending order.....	83
Figure 5.4 Comparison of acoustic enclosures	84
Figure 5.5 Correlation between sound pressure level and sound power	85
Figure 6.1 Analysis of the cavities and the resonators	87

Contents

1 SG codes of all models	2
1.1 Software - Download links	2
1.2 SG codes of the panel designs.....	2
1.3 SG codes of the acoustic enclosures	8
2 Absorption coefficients α of the panel designs over the frequency f	10

1 SG codes of all models

1.1 Software - Download links

- Link to download the Solid Geometry Library Toolbox®
<https://de.mathworks.com/matlabcentral/fileexchange/71951-sg-lib-matlab-toolbox>
- Link to download the PrusaSlicer®
<https://www.prusa3d.de/treiber/>

1.2 SG codes of the panel designs

Name: *Panel_flat – sides_t16*

SG code: SGofCPLcommand('c 39.9,h 16,write *Panel_flat – sides_t16*')

Definition: Create a circle with a diameter of 39.90 mm and extrude it up to a height of 16.00 mm. Save the model as *Panel_flat – sides_t16*.

Name: *Panel_4 × 4_depth20_t30*

SG code: SGofCPLcommand('c 39.90,h 30,enter,b 6,h 20,dups 4 4 1 1,move -10.5 -10.5 10,-,write *Panel_4 × 4_depth20_t30*')

Definition: Create a circle with a diameter of 39.90 mm and extrude it up to a height of 30.00 mm. Form 16 cavities arranged in a 4×4 matrix in the plain of a height of 10.00 mm above the bottom. Each cavity has an edge length of 6.00 mm and a depth of 20.00 mm and has the same distance of 1.00 mm to one another. The positioning of the cavities depends on the location of the lowest and leftmost cavity, which is moved -10.50 mm in x-direction and -10.50 mm in y-direction to create a central alignment of the matrix. Save the model as *Panel_4 × 4_depth20_t30*.

Name: *Panel_4 × 4_depth20_t22*

SG code: SGofCPLcommand('c 39.9,h 22,enter,b 6,h 20,dups 4 4 1 0.5,move -9.75 -9.75 2,-,write *Panel_4 × 4_depth20_t22*')

Definition: Create a circle with a diameter of 39.90 mm and extrude it up to a height of 22.00 mm. Form 16 cavities arranged in a 4×4 matrix in the plain of a height of 2.00 mm above the bottom. Each cavity has an edge length of 6.00 mm and a depth of 20.00 mm and has the same distance of 0.50 mm to one another. The positioning of the cavities depends on the location of the lowest and leftmost cavity, which is moved -9.75 mm in x-direction and -9.75 mm in y-direction to create a central alignment of the matrix. Save the model as *Panel_4 × 4_depth20_t22*.

Name: *Panel_5 × 5_depth20_t22*

SG code: SGofCPLcommand('c 39.9,h 22,enter,b 4,h 20,dups 5 5 1 0.5,move -9 -9 2,-,write *Panel_5 × 5_depth20_t22*')

Definition: Create a circle with a diameter of 39.90 mm and extrude it up to a height of 22.00 mm. Form 25 cavities arranged in a 5×5 matrix in the plain of a height of 2.00 mm above the bottom. Each cavity has an edge length of 4.00 mm and a depth of 20.00 mm and has the same distance of 0.50 mm to one another. The positioning of the cavities depends on the location of the lowest and leftmost cavity, which is moved -9.00 mm in x-direction and -9.00 mm in y-direction to create a central alignment of the matrix. Save the model as *Panel_5 × 5_depth20_t22*.

Name: *Panel_5 × 5_depth5_t17.7*

SG code: SGofCPLcommand('c 39.9,h 17.7,enter,b 4,h 5,dups 5 5 1 0.5,move -9 -9 12.7,-,write *Panel_5 × 5_depth5_t17.7*')

Definition: Create a circle with a diameter of 39.90 mm and extrude it up to a height of 17.70 mm. Form 25 cavities arranged in a 5×5 matrix in the plain of a height of 12.70 mm above the bottom. Each cavity has an edge length of 4.00 mm and a depth of 5.00 mm and has the same distance of 0.50 mm to one another. The positioning of the cavities depends on the location of the lowest and leftmost cavity, which is moved -9.00 mm in x-direction and -9.00 mm in y-direction to create a central alignment of the matrix. Save the model as *Panel_5 × 5_depth5_t17.7*.

Name: *Panel_5 × 5_depth10_t19.2*

SG code: SGofCPLcommand('c 39.9,h 19.2,enter,b 4,h 10,dups 5 5 1 0.5,move -9 -9 9.2,-,write *Panel_5 × 5_depth10_t19.2*')

Definition: Create a circle with a diameter of 39.90 mm and extrude it up to a height of 19.20 mm. Form 25 cavities arranged in a 5×5 matrix in the plain of a height of 9.20 mm above the bottom. Each cavity has an edge length of 4.00 mm and a depth of 10.00 mm and has the same distance of 0.50 mm to one another. The positioning of the cavities depends on the location of the lowest and leftmost cavity, which is moved -9.00 mm in x-direction and -9.00 mm in y-direction to create a central alignment of the matrix. Save the model as *Panel_5 × 5_depth10_t19.2*.

Name: *Panel_5 × 5_t24_without – bottom*

SG code: SGofCPLcommand('c 39.9,h 24,enter,b 4,h 24,dups 5 5 1 0.5,move -9 -9,-,write *Panel_5 × 5_t24_without – bottom*')

Definition: Create a circle with a diameter of 39.90 mm and extrude it up to a height of 24.00 mm. Form 25 cavities arranged in a 5×5 matrix. Each cavity has an edge length of 4.00 mm and a depth of 24.00 mm and has the same distance of 0.50 mm to one another. The positioning of the cavities depends on the location of the lowest and leftmost cavity, which is moved -9.00 mm in x-direction and -9.00 mm in y-direction to create a central alignment of the matrix. Save the model as *Panel_5 × 5_t24_without – bottom*.

Name: *Panel_5 × 5_deptht20_t22_lattice – edges*

SG code: SGofCPLcommand('c 39.9,h 24,enter,b 22,h 24,move 0 0,-,enter,b 0.5,h 24,dups 4 4 1 4,move -7 -7,save A,enter,load A,rotx 90,move 0 12 12,cat,enter,load A,roty 90,move -12 0 12,cat,cat,write *Panel_5 × 5_deptht20_t22_lattice – edges*')

Definition: Create a circle with a diameter of 39.90 mm and extrude it up to a height of 24.00 mm. Form a rectangular cavity with edge lengths of 22.00 mm and a height of 24.00 mm. Create 48 bars of the dimensions $0.50 \times 0.50 \times 24.00$ mm and arrange them in a three-dimensional matrix. A total of 16 bars are installed in each spatial direction, of which four bars each are positioned in four rows in a distance of 4.00 mm. The positioning of the bars depends on the location of the lowest and leftmost bars in the respective plane, which is moved -7.00 mm in x-direction and -7.00 mm in y-direction for the x-y-level. Save this geometry and rotate it twice by an angle of 90 degree. Move each generated geometry 12.00 mm in the y-direction or -12.00 mm in the x-direction to create a central alignment of the matrix. Save the model as *Panel_5 × 5_deptht20_t22_lattice – edges*.

Name: *Panel_8 × 8_depth20_t22*

SG code: SGofCPLcommand('c 39.9,h 22,enter,b 2.5,h 20,dups 8 8 1 0.5,move -10.5 -10.5 2,-,write *Panel_8 × 8_depth20_t22*')

Definition: Create a circle with a diameter of 39.90 mm and extrude it up to a height of 22.00 mm. Form 64 cavities arranged in a 8×8 matrix in the plain of a height of 2.00 mm above the bottom. Each cavity has an edge length of 2.50 mm and a depth of 20.00 mm and has the same distance of 0.50 mm to one another. The positioning of the cavities depends on the location of the lowest and leftmost cavity, which is moved -10.50 mm in x-direction and -10.50 mm in y-direction to create a central alignment of the matrix. Save the model as *Panel_8 × 8_depth20_t22*.

Name: *Panel_13 × 13_depth20_t22*

SG code: SGofCPLcommand('c 39.9,h 22,enter,b 1.5,h 20,dups 13 13 1 0.5,move -12 -12 2,-,write *Panel_13 × 13_depth20_t22*')

Definition: Create a circle with a diameter of 39.90 mm and extrude it up to a height of 22.00 mm. Form 169 cavities arranged in a 13×13 matrix in the plain of a height of 2.00 mm above the bottom. Each cavity has an edge length of 1.50 mm and a depth of 20.00 mm and has the same distance of 0.50 mm to one another. The positioning of the cavities depends on the location of the lowest and leftmost cavity, which is moved -12.00 mm in x-direction and -12.00 mm in y-direction to create a central alignment of the matrix. Save the model as *Panel_13 × 13_depth20_t22*.

Name: *Panel_5 × 5_depth20_t22_cube – fixed – on – bottom*

SG code: SGofCPLcommand('c 39.9,h 22,enter,b 4,h 20,dups 5 5 1 0.5,move -9 -9 2,-,enter,b 1,h 20,dups 5 5 1 3.5,move -9 -9 2,cat,write *Panel_5 × 5_depth20_t22_cube – fixed – on – bottom*')

Definition: Create a circle with a diameter of 39.90 mm and extrude it up to a height of 22.00 mm. Form 25 cavities arranged in a 5×5 matrix in the plain of a height of 2.00 mm above the bottom. Each cavity has an edge length of 4.00 mm and a depth of 20.00 mm and has the same distance of 0.50 mm to one another. The positioning of the cavities depends on the location of the lowest and leftmost cavity, which is moved -9.00 mm in x-direction and -9.00 mm

in y-direction to create a central alignment of the matrix. Form 25 rectangular blocks with a length of 1.00 mm, a width of 1.00 mm and a height of 20.00 mm. Arrange these blocks in a 5×5 matrix in the plain of a height of 2.00 mm above the bottom in an equal distance of 3.50 mm to one another. The positioning of the resonant blocks also depends on the location of the lowest and leftmost resonator, which is moved -9.00 mm in x-direction and -9.00 mm in y-direction. Save the model as *Panel_5 × 5_depth20_t22_cube – fixed – on – bottom*.

Name: *Panel_5 × 5_depth20_t22_cube – fixed – on – bottom_thicker*

SG code: SGofCPLCommand('c 39.9,h 22,enter,b 4,h 20,dups 5 5 1 0.5,move -9 -9 2,-,enter,b 2,h 5,dups 5 5 1 2.5,move -9 -9 2,cat,write *Panel_5 × 5_depth20_t22_cube – fixed – on – bottom_thicker*')

Definition: Create a circle with a diameter of 39.90 mm and extrude it up to a height of 22.00 mm. Form 25 cavities arranged in a 5×5 matrix in the plain of a height of 2.00 mm above the bottom. Each cavity has an edge length of 4.00 mm and a depth of 20.00 mm and has the same distance of 0.50 mm to one another. The positioning of the cavities depends on the location of the lowest and leftmost cavity, which is moved -9.00 mm in x-direction and -9.00 mm in y-direction to create a central alignment of the matrix. Form 25 rectangular blocks with a length of 2.00 mm, a width of 2.00 mm and a height of 5.00 mm. Arrange these blocks in a 5×5 matrix in the plain of a height of 2.00 mm above the bottom in an equal distance of 2.50 mm to one another. The positioning of the resonant blocks also depends on the location of the lowest and leftmost resonator, which is moved -9.00 mm in x-direction and -9.00 mm in y-direction. Save the model as *Panel_5 × 5_depth20_t22_cube – fixed – on – bottom_thicker*.

Name: *Panel_5 × 5_depth20_t22_cube – fixed – on – sidewall_two – rowed*

SG code: SGofCPLCommand('c 39.9,h 22,enter,b 4,h 20,dups 5 5 1 0.5,move -9 -9 2,-,enter,b 2,h 2.5,dups 5 5 2 2.5,move -10 -9 12,cat,write *Panel_5 × 5_depth20_t22_cube – fixed – on – sidewall_two – rowed*')

Definition: Create a circle with a diameter of 39.90 mm and extrude it up to a height of 22.00 mm. Form 25 cavities arranged in a 5×5 matrix in the plain of a height of 2.00 mm above the bottom. Each cavity has an edge length of 4.00 mm and a depth of 20.00 mm and has the same distance of 0.50 mm to one another. The positioning of the cavities depends on the location of the lowest and leftmost cavity, which is moved -9.00 mm in x-direction and -9.00 mm in y-direction to create a central alignment of the matrix. Form 50 rectangular blocks with a length of 2.00 mm, a width of 2.00 mm and a height of 2.50 mm. Arrange these blocks in a 5×5 matrix in the plain of a height of 12.00 mm and 17.00 mm above the bottom in an equal distance of 2.50 mm to one another. The positioning of the resonant blocks also depends on the location of the lowest and leftmost resonator, which is moved -10.00 mm in x-direction and -9.00 mm in y-direction. Save the model as *Panel_5 × 5_depth20_t22_cube – fixed – on – sidewall_two – rowed*.

Name: *Panel_5 × 5_depth20_t22_cube – fixed – on – sidewall_single – row*

SG code: SGofCPLCommand('c 39.9,h 22,enter,b 4,h 20,dups 5 5 1 0.5,move -9 -9 2,-,enter,b 2,h 5,dups 5 5 1 2.5,move -10 -9 12,cat,write *Panel_5 × 5_depth20_t22_cube – fixed – on – sidewall_single – row*')

Definition: Create a circle with a diameter of 39.90 mm and extrude it up to a height of 22.00 mm. Form 25 cavities arranged in a 5×5 matrix in the plain of a height of 2.00 mm above the

bottom. Each cavity has an edge length of 4.00 mm and a depth of 20.00 mm and has the same distance of 0.50 mm to one another. The positioning of the cavities depends on the location of the lowest and leftmost cavity, which is moved -9.00 mm in x-direction and -9.00 mm in y-direction to create a central alignment of the matrix. Form 25 rectangular blocks with a length of 2.00 mm, a width of 2.00 mm and a height of 5.00 mm. Arrange these blocks in a 5×5 matrix in the plain of a height of 12.00 mm above the bottom in an equal distance of 2.50 mm to one another. The positioning of the resonant blocks also depends on the location of the lowest and leftmost resonator, which is moved -10.00 mm in x-direction and -9.00 mm in y-direction. Save the model as *Panel_5 × 5_depth20_t22_cube – fixed – on – sidewall_single – row*.

Name: *Panel_5 × 5_depth20_t22_conical_resonator_bridge*

SG code: SGofCPLCommand('c 39.9,h 22,enter,b 4,h 20,dups 5 5 1 0.5,move -9 -9 2,-,enter,b 3 4 -3,enter,b 3 4,move -3,-,r 360,move 0 0 13,enter,b 1,h 10,+,move -9 -9 2,dups 5 5 1 1.5,cat,write *Panel_5 × 5_depth20_t22_conical_resonator_bridge*')

Definition: Create a circle with a diameter of 39.90 mm and extrude it up to a height of 22.00 mm. Form 25 cavities arranged in a 5×5 matrix in the plain of a height of 2.00 mm above the bottom. Each cavity has an edge length of 4.00 mm and a depth of 20.00 mm and has the same distance of 0.50 mm to one another. The positioning of the cavities depends on the location of the lowest and leftmost cavity, which is moved -9.00 mm in x-direction and -9.00 mm in y-direction to create a central alignment of the matrix. Form 25 cones with a diameter of 3.00 mm and a height of 4.00 mm. Arrange these blocks in a 5×5 matrix in the plain of a height of 12.00 mm above the bottom in an equal distance of 1.50 mm to one another. Form 25 rectangular blocks (bridges) with a length of 1.00 mm, a width of 1.00 mm and a height of 10.00 mm. Arrange these blocks in a 5×5 matrix in the plain of a height of 2.00 mm above the bottom in an equal distance of 2.50 mm to one another. The positioning of the resonant blocks and the bridges also depends on the location of the lowest and leftmost resonator, which is moved -9.00 mm in x-direction and -9.00 mm in y-direction. Save the model as *Panel_5 × 5_depth20_t22_conical_resonator_bridge*.

Name: *Panel_5 × 5_depth20_t22_hemispherical_resonator_bridge*

SG code: SGofCPLCommand('c 39.9,h 22,enter,b 4,h 20,dups 5 5 1 0.5,move -9 -9 2,-,enter,sph 3,enter,b 3,h 3,move 0 0 -3,-,move 0 0 10,enter,b 1,h 10,+,move -9 -9 2,dups 5 5 1 1.5,cat,write *Panel_5 × 5_depth20_t22_hemispherical_resonator_bridge*')

Definition: Create a circle with a diameter of 39.90 mm and extrude it up to a height of 22.00 mm. Form 25 cavities arranged in a 5×5 matrix in the plain of a height of 2.00 mm above the bottom. Each cavity has an edge length of 4.00 mm and a depth of 20.00 mm and has the same distance of 0.50 mm to one another. The positioning of the cavities depends on the location of the lowest and leftmost cavity, which is moved -9.00 mm in x-direction and -9.00 mm in y-direction to create a central alignment of the matrix. Form 25 hemispheres with a diameter of 3.00 mm. Arrange these blocks in a 5×5 matrix in the plain of a height of 12.00 mm above the bottom in an equal distance of 1.50 mm to one another. Form 25 rectangular blocks (bridges) with a length of 1.00 mm, a width of 1.00 mm and a height of 10.00 mm. Arrange these blocks in a 5×5 matrix in the plain of a height of 2.00 mm above the bottom in an equal distance of 2.50 mm to one another. The positioning of the resonant blocks and the bridges also depends on the location of the lowest and leftmost resonator, which is moved -9.00 mm in x-direction and -9.00 mm in y-direction. Save the model as *Panel_5 × 5_depth20_t22_hemispherical_resonator_bridge*.

Name: *Panel_4 × 4_depth20_t22_cylindrical – grid*

SG code: SGofCPLCommand('c 39.9,h 22,enter,c 6,h 20,dups 4 4 1 0.5,move -9.75 -9.75 2,-,cat,write *Panel_4 × 4_depth20_t22_cylindrical – grid*')

Definition: Create a circle with a diameter of 39.90 mm and extrude it up to a height of 22.00 mm. Form 16 cavities arranged in a 4×4 matrix in the plain of a height of 2.00 mm above the bottom. Each cavity has a diameter of 6.00 mm and a depth of 20.00 mm and has the same distance of 0.50 mm to one another. The positioning of the cavities depends on the location of the lowest and leftmost cavity, which is moved -9.75 mm in x-direction and -9.75 mm in y-direction to create a central alignment of the matrix. Save the model as *Panel_4 × 4_depth20_t22_cylindrical – grid*.

Name: *Panel_5 × 5_depth20_t22_cylindrical – grid*

SG code: SGofCPLCommand('c 39.9,h 22,enter,c 4,h 20,dups 5 5 1 0.5,move -9 -9 2,-,cat,write *Panel_5 × 5_depth20_t22_cylindrical – grid*')

Definition: Create a circle with a diameter of 39.90 mm and extrude it up to a height of 22.00 mm. Form 25 cavities arranged in a 5×5 matrix in the plain of a height of 2.00 mm above the bottom. Each cavity has a diameter of 4.00 mm and a depth of 20.00 mm and has the same distance of 0.50 mm to one another. The positioning of the cavities depends on the location of the lowest and leftmost cavity, which is moved -9.00 mm in x-direction and -9.00 mm in y-direction to create a central alignment of the matrix. Save the model as *Panel_5 × 5_depth20_t22_cylindrical – grid*.

Name: *Panel_8 × 8_depth20_t22_cylindrical – grid*

SG code: SGofCPLCommand('c 39.9,h 22,enter,c 2.5,h 20,dups 8 8 1 0.5,move -10 -10 2,-,cat,write *Panel_8 × 8_depth20_t22_cylindrical – grid*')

Definition: Create a circle with a diameter of 39.90 mm and extrude it up to a height of 22.00 mm. Form 64 cavities arranged in a 8×8 matrix in the plain of a height of 2.00 mm above the bottom. Each cavity has a diameter of 2.50 mm and a depth of 20.00 mm and has the same distance of 0.50 mm to one another. The positioning of the cavities depends on the location of the lowest and leftmost cavity, which is moved -10.00 mm in x-direction and -10.00 mm in y-direction to create a central alignment of the matrix. Save the model as *Panel_8 × 8_depth20_t22_cylindrical – grid*.

Name: *Panel_5 × 5_depth20_t22_cylindrical – grid_cube – fixed – on – bottom*

SG code: SGofCPLCommand('c 39.9,h 22,enter,c 4,h 20,dups 5 5 1 0.5,move -9 -9 2,-,enter,b 1,h 20.5,dups 5 5 1 3.5,move -9 -9 1.5,cat,write *Panel_5 × 5_depth20_t22_cylindrical – grid_cube – fixed – on – bottom*')

Definition: Create a circle with a diameter of 39.90 mm and extrude it up to a height of 22.00 mm. Form 25 cavities arranged in a 5×5 matrix in the plain of a height of 2.00 mm above the bottom. Each cavity has a diameter of 4.00 mm and a depth of 20.00 mm and has the same distance of 0.50 mm to one another. The positioning of the cavities depends on the location of the lowest and leftmost cavity, which is moved -9.00 mm in x-direction and -9.00 mm in z-direction to create a central alignment of the matrix. Form 25 rectangular blocks with a length of 1.00 mm, a width of 1.00 mm and a height of 20.00 mm. Arrange these blocks in a 5×5 matrix in the plain of a height of 2.00 mm above the bottom in an equal distance of 3.50 mm to one another. The positioning of the resonant blocks also depends on the location of the lowest

and leftmost resonator, which is moved -9.00 mm in x-direction and -9.00 mm in y-direction. Save the model as *Panel_5 × 5_depth20_t22_cylindrical – grid_cube – fixed – on – bottom*.

Name: *Panel_5 × 5_depth20_t22_checkerboard – patterns*

SG code: SGofCPLcommand('c 39.9,h 22,enter,b 4,h 20,dups 5 5 1 0.5,move -9 -9 2,-,enter,b 2,h 5,dups 3 2 1 7,move -9 -5.5 12,enter,b 2,h 5,dups 2 3 1 7,move -5.5 -9 12,enter,b 1,h 20.5,dups 3 3 1 8,move -9 -9 1.5,enter,b 1,h 20.5,dups 2 2 1 8,move -4.5 -4.5 1.5,cat,cat,cat,cat,write *Panel_5 × 5_depth20_t22_checkerboard – patterns*')

Definition: Create a circle with a diameter of 39.90 mm and extrude it up to a height of 22.00 mm. Form 25 cavities arranged in a 5×5 matrix in the plain of a height of 2.00 mm above the bottom. Each cavity has an edge length of 4.00 mm and a depth of 20.00 mm and has the same distance of 0.50 mm to one another. The positioning of the cavities depends on the location of the lowest and leftmost cavity, which is moved -9.00 mm in x-direction and -9.00 mm in y-direction to create a central alignment of the matrix. Form 13 rectangular blocks with a length of 1.00 mm, a width of 1.00 mm and a height of 20.00 mm and twelve rectangular blocks with a length of 2.00 mm, a width of 2.00 mm and a height of 5.00 mm. Insert these blocks alternately into the cavities of the 5×5 matrix in the plain of a height of 2.00 mm or 12 mm above the bottom in an equal distance of 8.00 mm or 7.00 mm to one another. The positioning of the resonant blocks also depends on the location of the lowest and leftmost resonator. Depending on the respective structure the bodies are moved -9.00 mm in x-direction and -5.50 mm in y-direction or -5.50 mm in x-direction and -9.00 mm in y-direction or -9.00 mm in x-direction and -9.00 mm in y-direction and -4.50 mm in x-direction and -4.50 mm in y-direction. Save the model as *Panel_5 × 5_depth20_t22_checkerboard – patterns*.

1.3 SG codes of the acoustic enclosures

Name: *Acoustic – enclosure_flatsides_t5*

SG code: SGofCPLcommand('b 60,h 5,dup,rotx 90,move 0 30,dupr 4,move 0 0 30,cat,write *Acoustic – enclosure_flatsides_t5*')

Definition: Create a square plate with edge lengths of 60.00×60.00 mm and extrude it up to a height of five mm. Create five of these plates and rotate each plate by 90° and move the plates by 30.00 mm in x-, y- and z-direction respectively, so that a cube open to one side is created. Save the model as *Acoustic – enclosure_flatsides_t5*.

Name: *Acoustic – enclosure_10 × 10_depth5.25_t7.25*

SG code: SGofCPLcommand('b 60,h 7.25,enter,b 4,h 5.25,dups 10 10 1 0.5,move -20.25 -20.25 2,-,dup,rotx 90,move 0 30,dupr 4,move 0 0 30,cat,write *Acoustic – enclosure_10 × 10_depth5.25_t7.25*')

Definition: Create a square plate with edge lengths of 60.00×60.00 mm and extrude it up to a height of 7.25 mm. Form 100 cavities arranged in a 10×10 matrix in the plain of a height of 2.00 mm above the bottom. Each cavity has an edge length of 4.00 mm and a depth of 5.25 mm and has the same distance of 0.50 mm to one another. The positioning of the cavities depends on the location of the lowest and leftmost cavity, which is moved -20.25 mm in x-direction and -20.25 mm in y-direction to create a central alignment of the matrix. Create five of these plates and rotate each plate by 90° and move the plates by 30.00 mm in

x-, y- and z-direction respectively, so that a cube open to one side is created. Save the model as *Acoustic – enclosure_10 × 10_depth5.25_t7.25*.

Name: *Acoustic – enclosure_10 × 10_depth5.25_t7.25_resonator*

SG code: SGofCPLcommand('b 60,h 7.25,enter,b 4,h 5.25,dups 10 10 1 0.5,move -20.25 -20.25 2,-,enter,b 1,dupc 10 10 3.5,h 5.5,move -20.25 -20.25 2,cat,dup,rotx 90,move 0 30,dupr 4,move 0 0 30,cat,write *Acoustic – enclosure_10 × 10_depth5.25_t7.25_resonator*')

Definition: Create a square plate with edge lengths of 60.00 × 60.00 mm and extrude it up to a height of 7.25 mm. Form 100 cavities arranged in a 10 × 10 matrix in the plain of a height of 2.00 mm above the bottom. Each cavity has an edge length of 4.00 mm and a depth of 5.25 mm and has the same distance of 0.50 mm to one another. The positioning of the cavities depends on the location of the lowest and leftmost cavity, which is moved -24.75 mm in x-direction and -24.75 mm in y-direction to create a central alignment of the matrix. Form 100 rectangular blocks with a length of 1.00 mm, a width of 1.00 mm and a height of 5.25 mm. Arrange these blocks in a 10 × 10 matrix in the plain of a height of 2.00 mm above the bottom in an equal distance of 3.50 mm to one another. The positioning of the resonant blocks also depends on the location of the lowest and leftmost resonator, which is moved -20.25 mm in x-direction and -20.25 mm in y-direction. Rotate each plate by 90° and move the plates by 30.00 mm in x-, y- and z-direction respectively, so that a cube open to one side is created. Save the model as *Acoustic – enclosure_10 × 10_depth5.25_t7.25_resonator*.

2 Absorption coefficients α of the panel designs over the frequency f

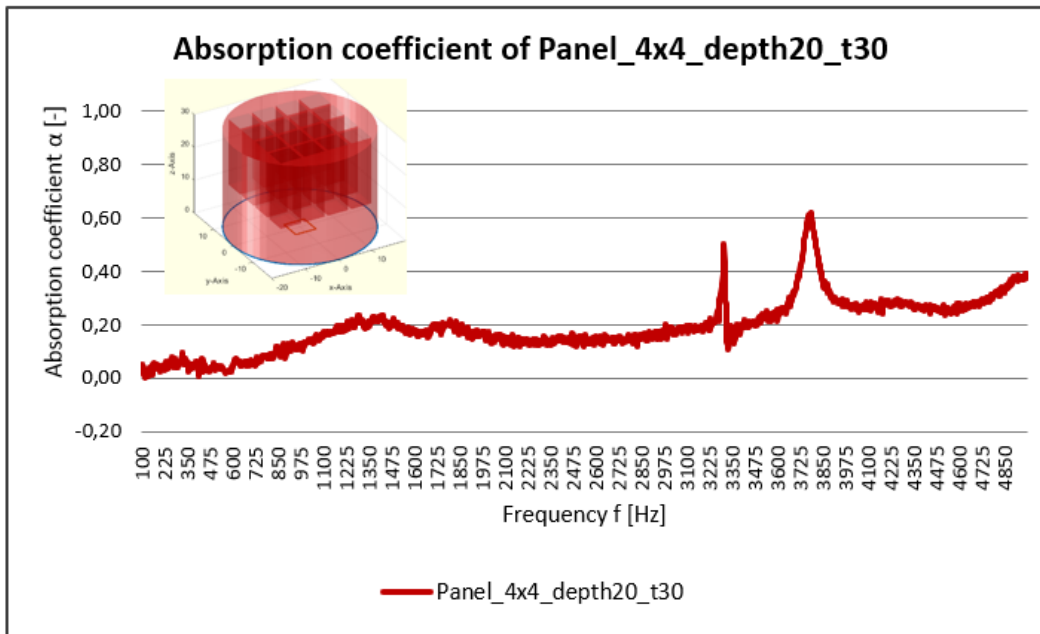


Figure 2.1: Absorption coefficient α of Panel_4 × 4_depth20_t30

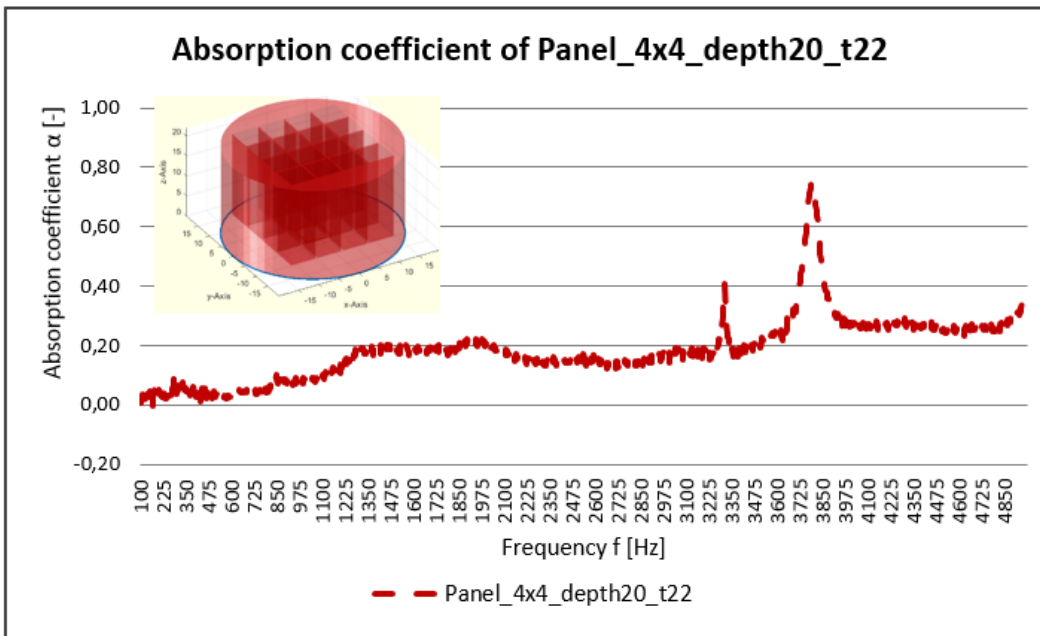
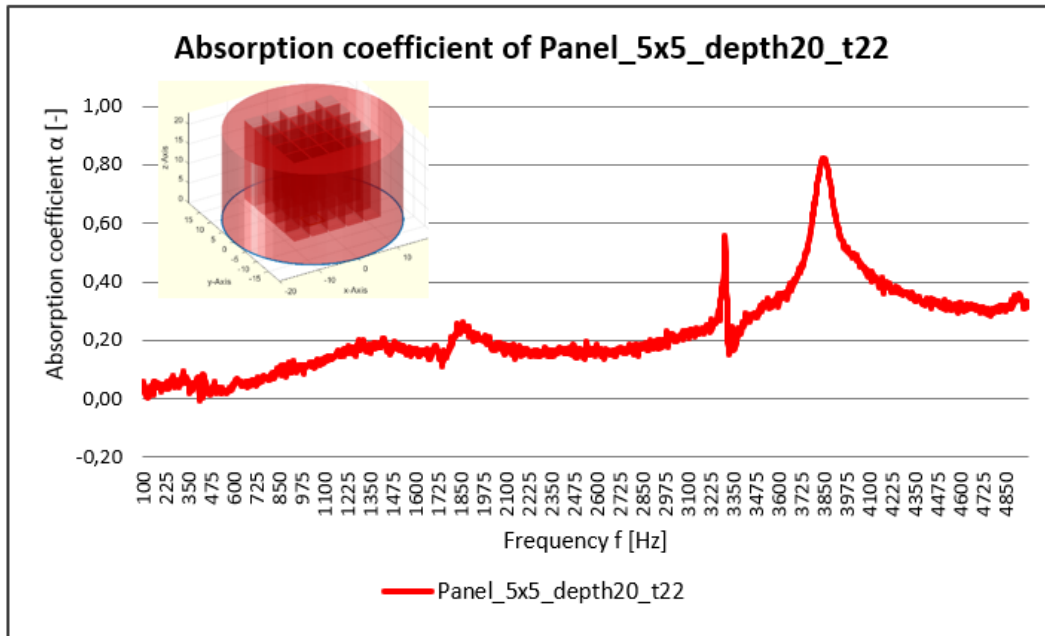
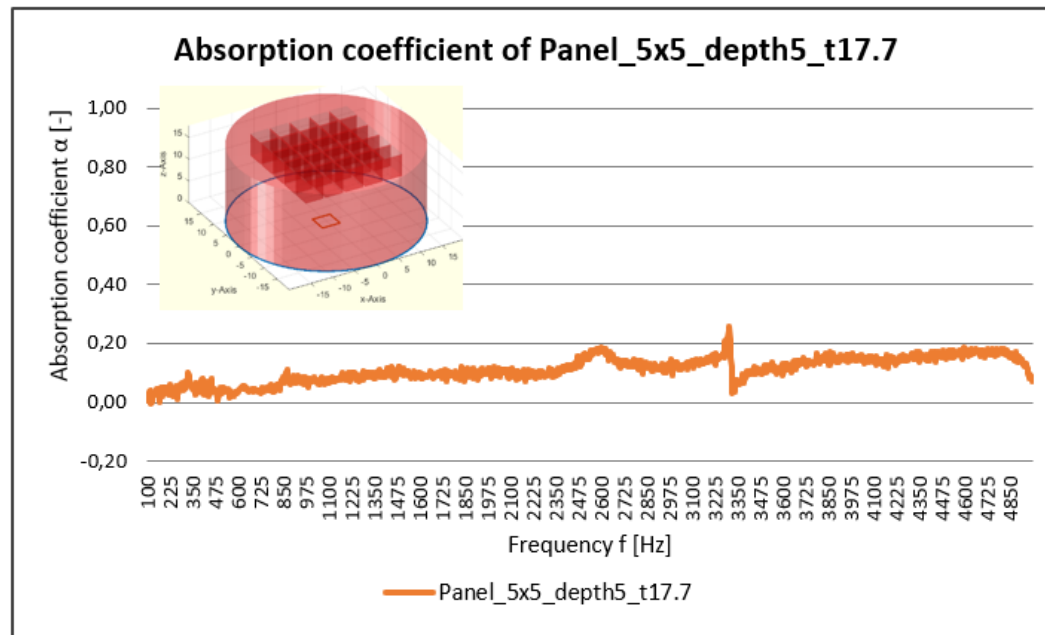


Figure 2.2: Absorption coefficient α of Panel_4 × 4_depth20_t22

Figure 2.3: Absorption coefficient α of Panel_5 × 5_depth20_t22Figure 2.4: Absorption coefficient α of Panel_5 × 5_depth5_t17.7

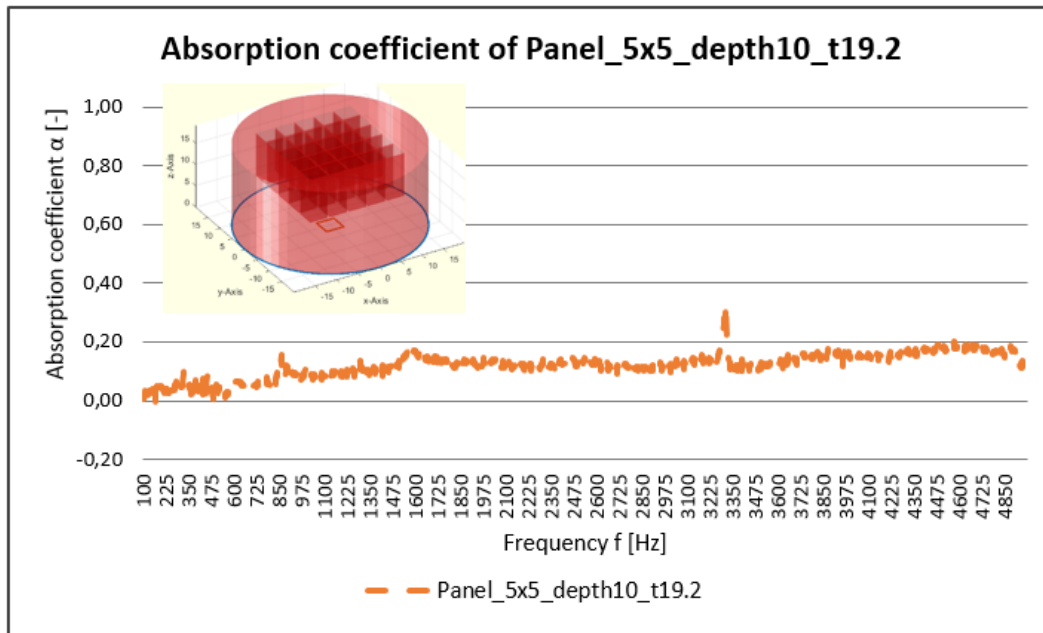


Figure 2.5: Absorption coefficient α of Panel_5 × 5_depth10_t19.2

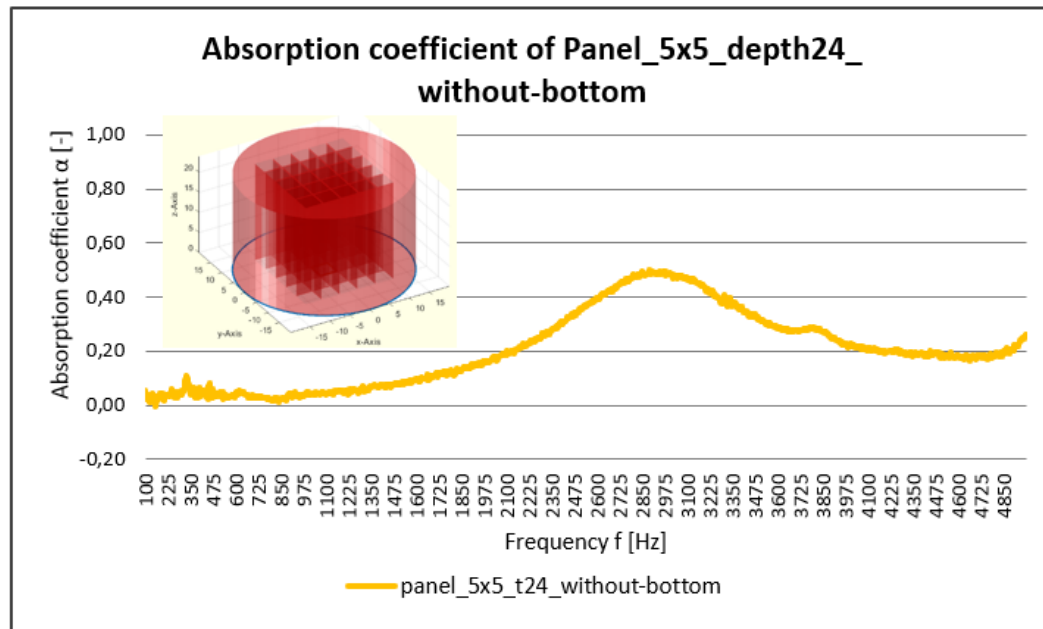


Figure 2.6: Absorption coefficient α of Panel_5 × 5_t24_without – bottom

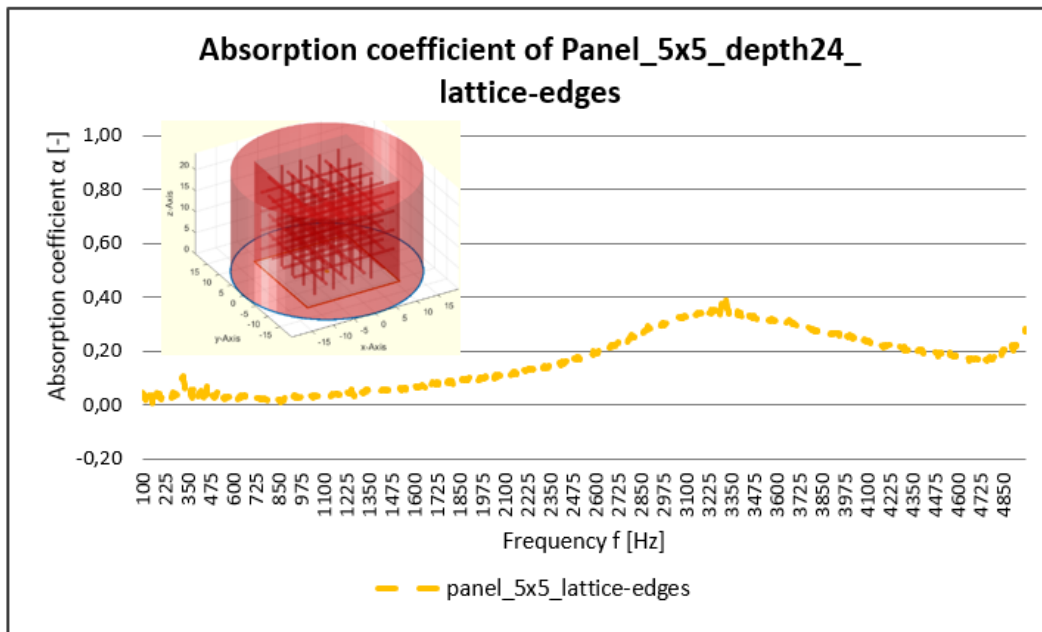


Figure 2.7: Absorption coefficient α of Panel_5 × 5_deptht20_t22_lattice – edges

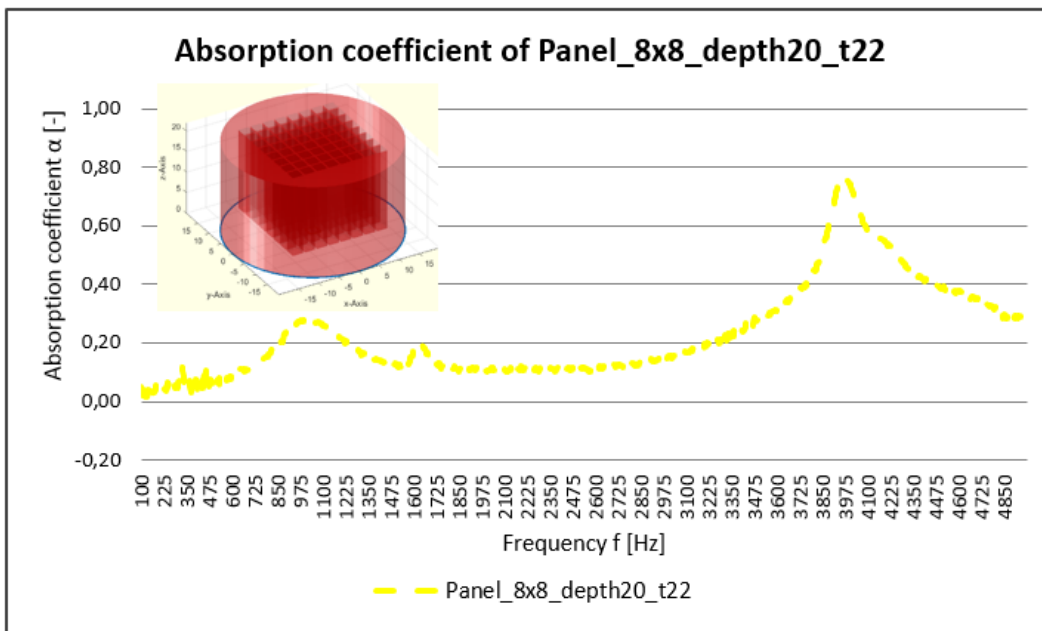


Figure 2.8: Absorption coefficient α of Panel_8 × 8_depth20_t22

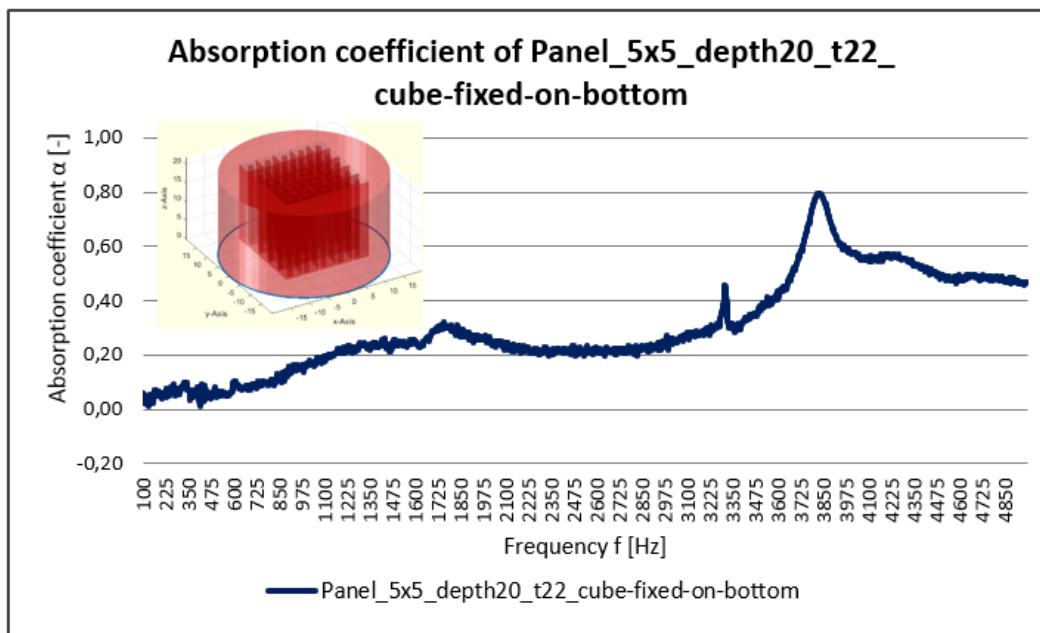


Figure 2.9: Absorption coefficient α of
Panels₅ × 5_depth20_t22_cube – fixed – on – bottom

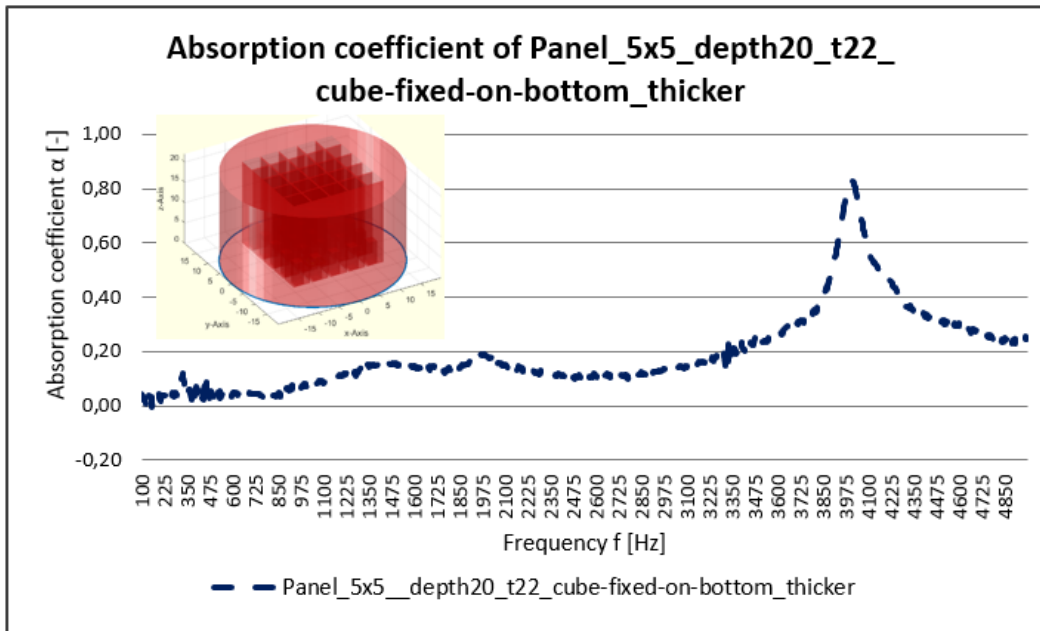


Figure 2.10: Absorption coefficient α of
Panel_5 × 5_depth20_t22_cube – fixed – on – bottom_thicker

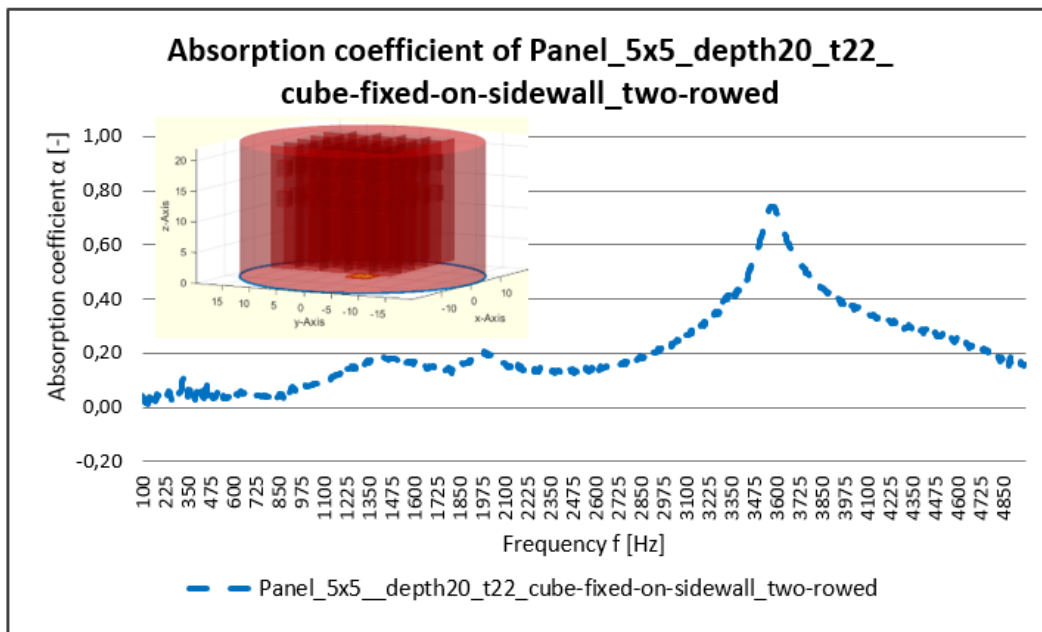


Figure 2.11: Absorption coefficient α of
Panel_5 × 5_depth20_t22_cube – fixed – on – sidewall _two – rowed

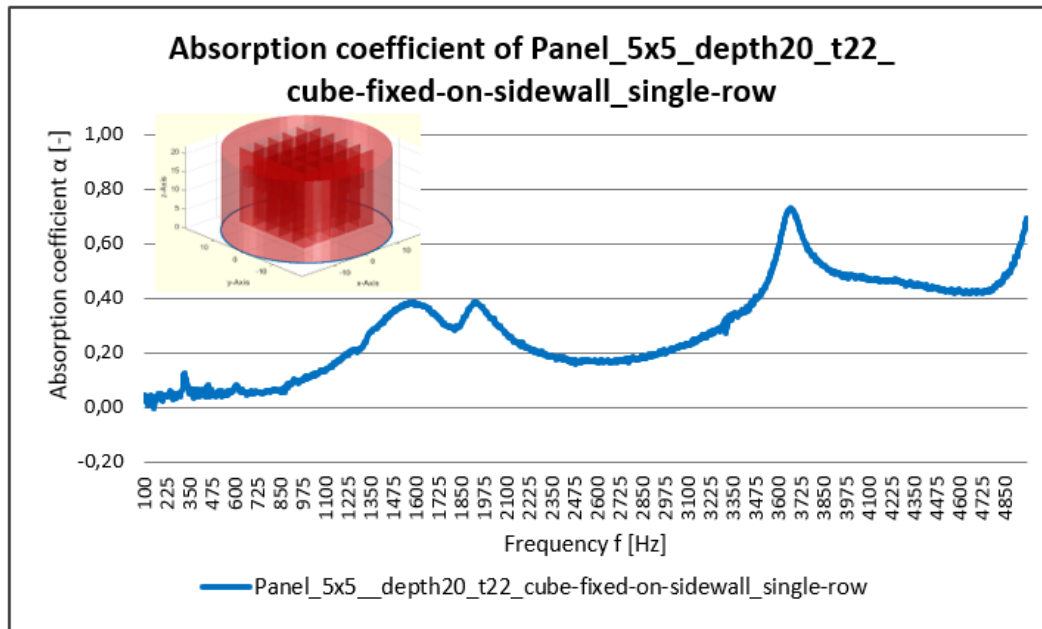


Figure 2.12: Absorption coefficient α of
Panel_5 × 5_depth20_t22_cube – fixed – on – sidewall _single – row

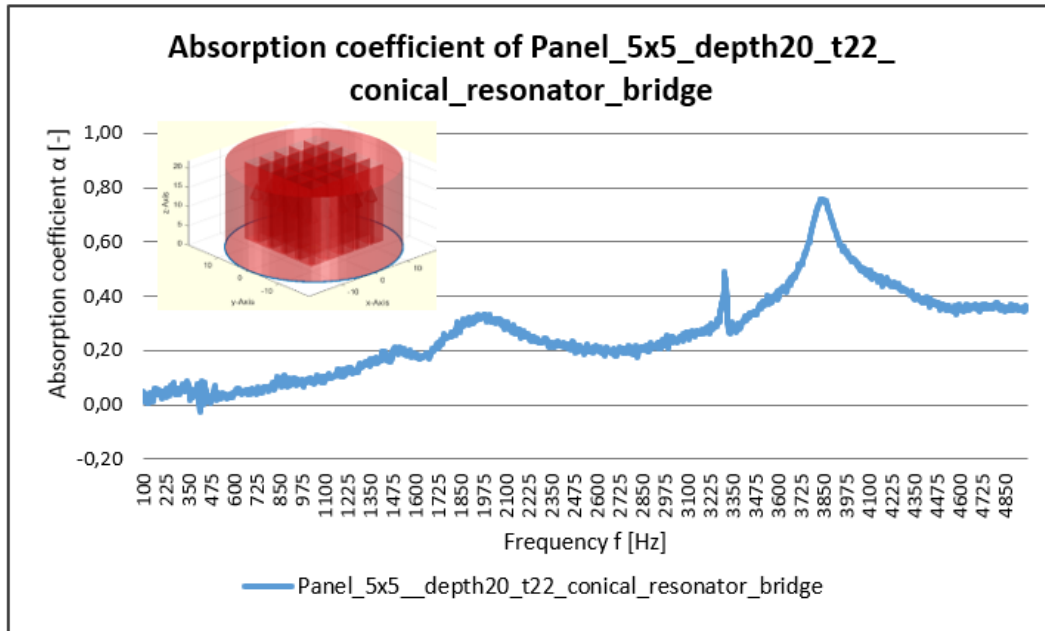


Figure 2.13: Absorption coefficient α of
Panel_5 × 5_depth20_t22_conical_resonator_bridge

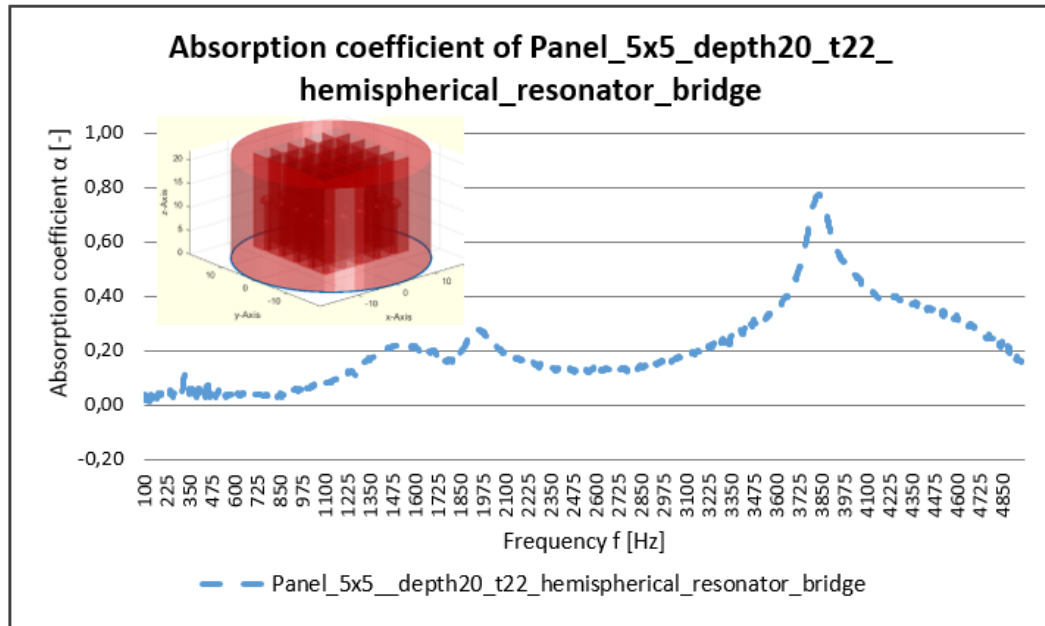


Figure 2.14: Absorption coefficient α of
Panel_5 × 5_depth20_t22_hemispherical_resonator_bridge

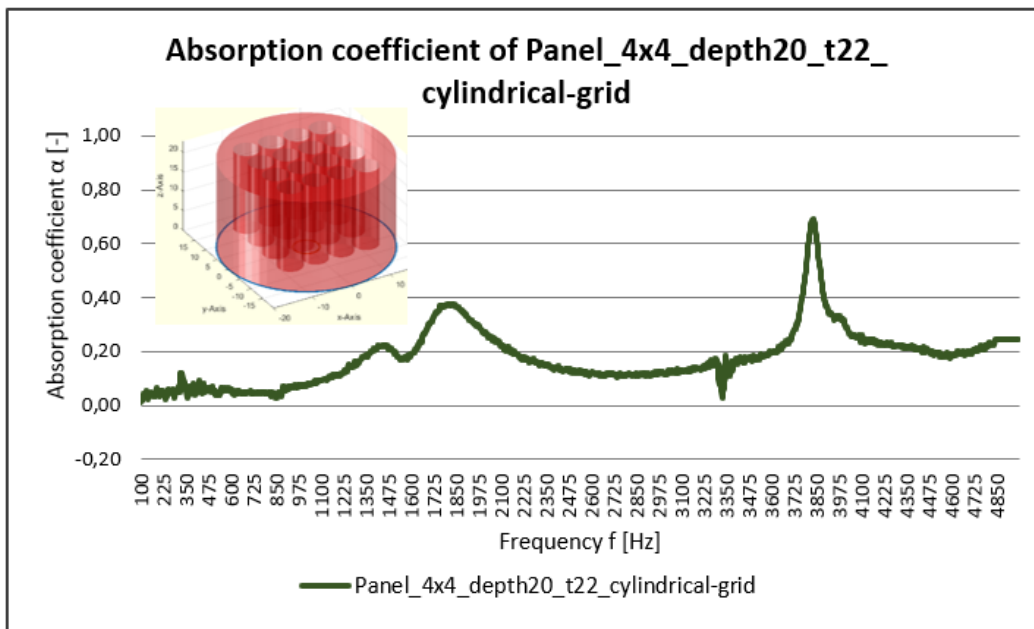


Figure 2.15: Absorption coefficient α of Panel_4 × 4_depth20_t22_cylindrical – grid

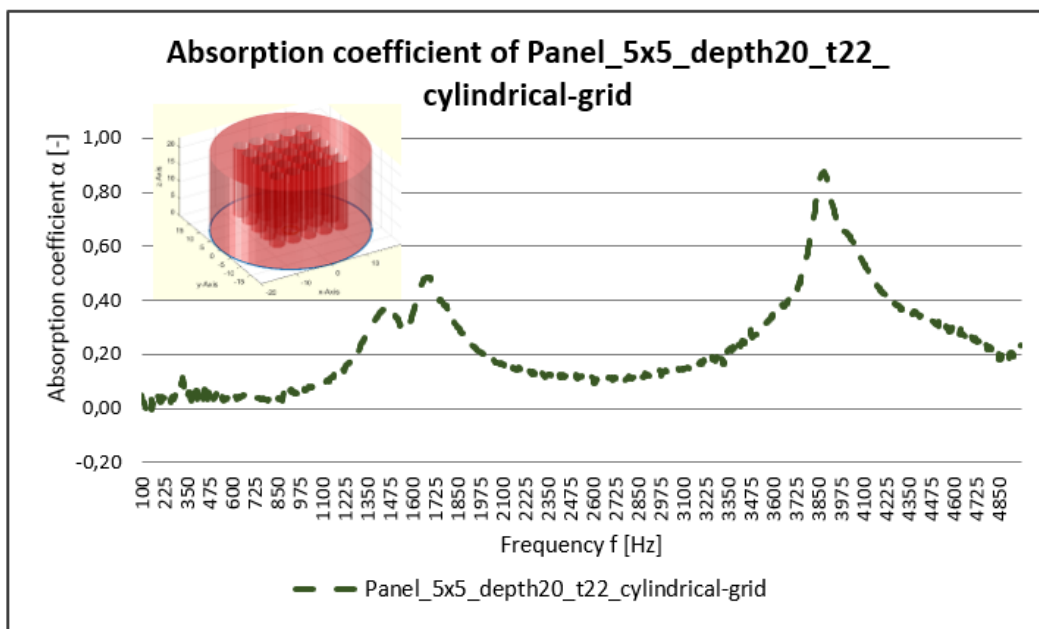


Figure 2.16: Absorption coefficient α of Panel_5 × 5_depth20_t22_cylindrical – grid

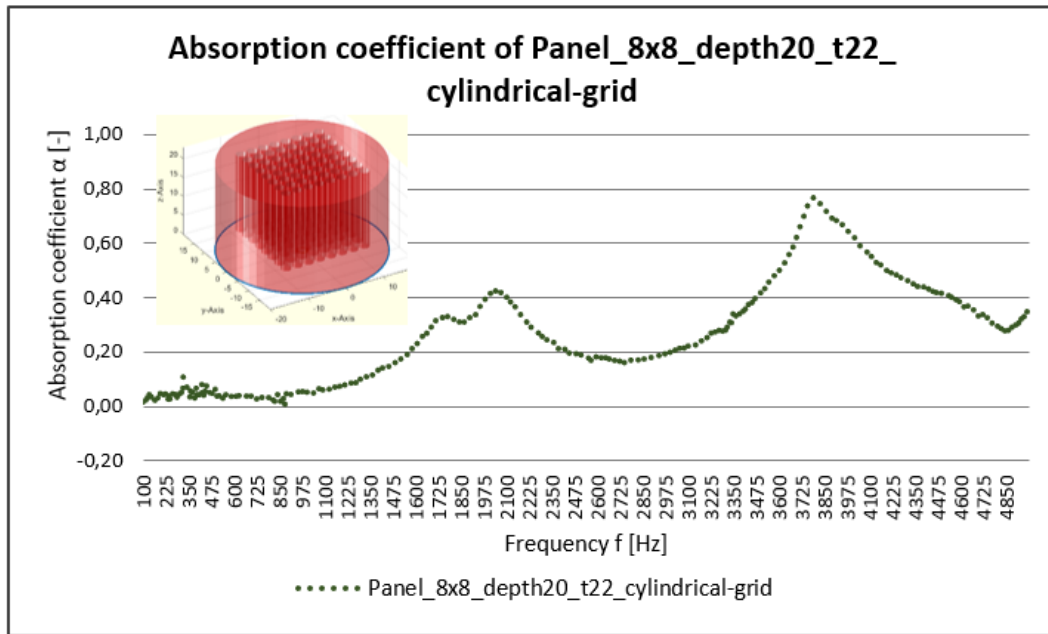


Figure 2.17: Absorption coefficient α of Panel_8 × 8_depth20_t22_cylindrical – grid

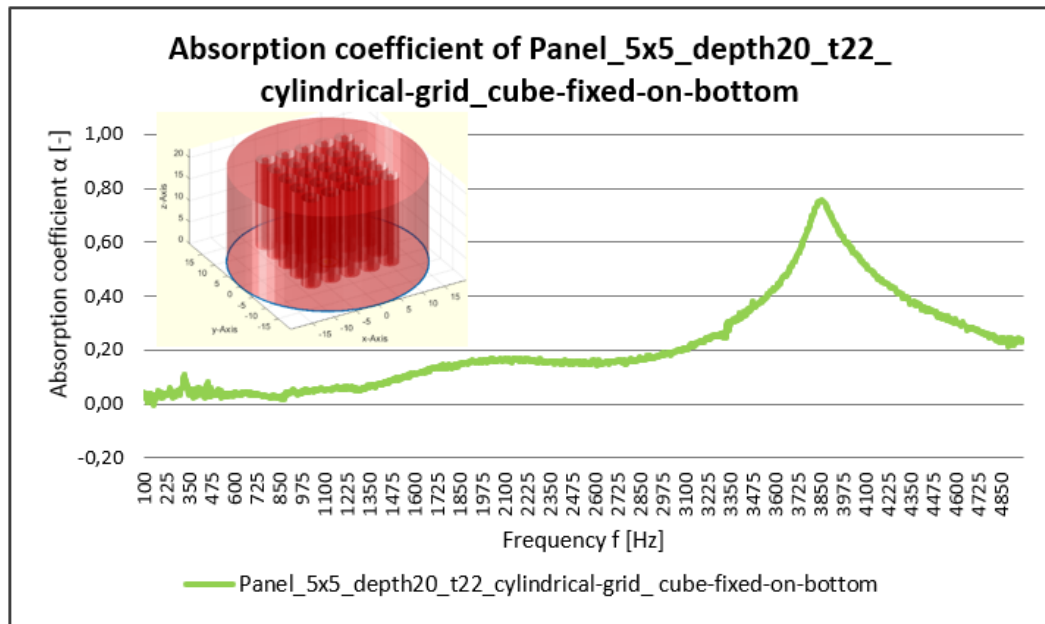


Figure 2.18: Absorption coefficient α of Panel_5 × 5_depth20_t22_cylindrical – grid_cube – fixed – on – bottom

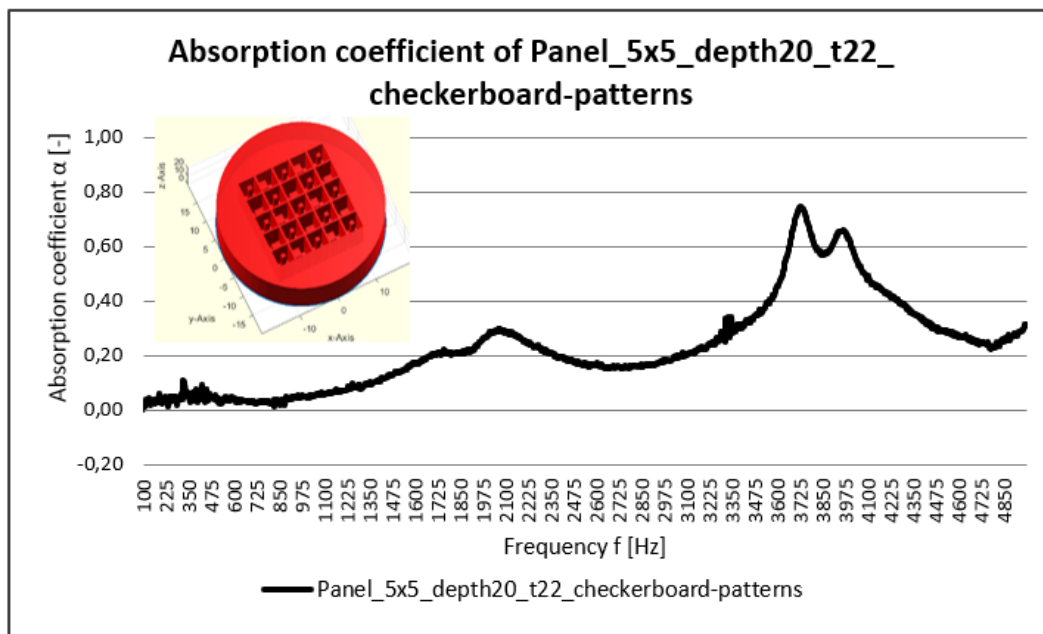


Figure 2.19: Absorption coefficient α of
Panel_5 × 5_depth20_t22_checkerboard – patterns

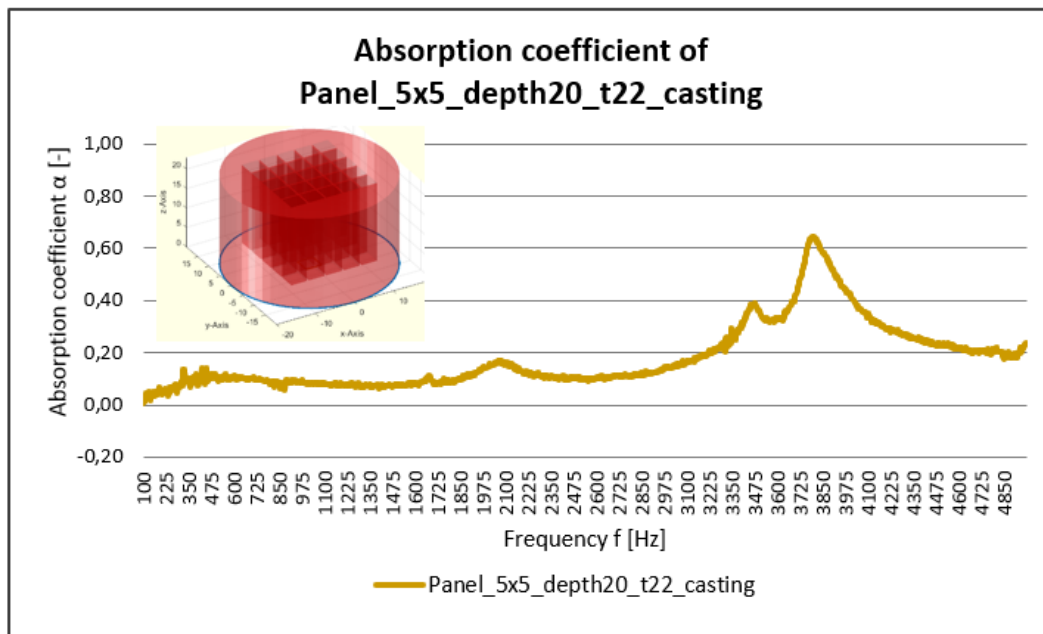


Figure 2.20: Absorption coefficient α of Panel_5 × 5_depth20_t22_casting

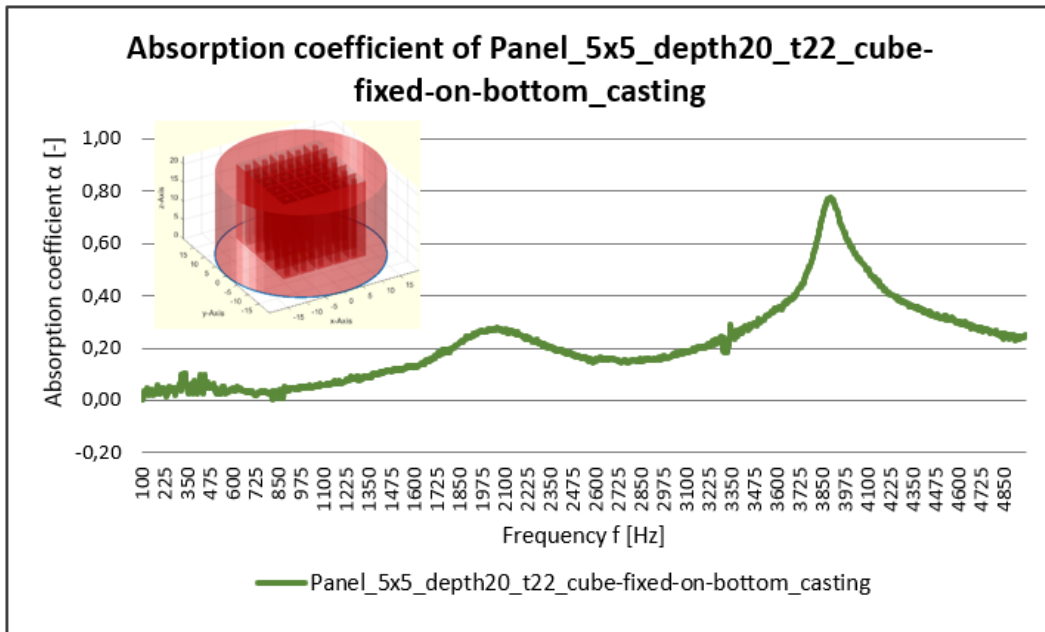


Figure 2.21: Absorption coefficient α of
Panel_5 × 5_depth20_t22_cube – fixed – on – bottom_casting

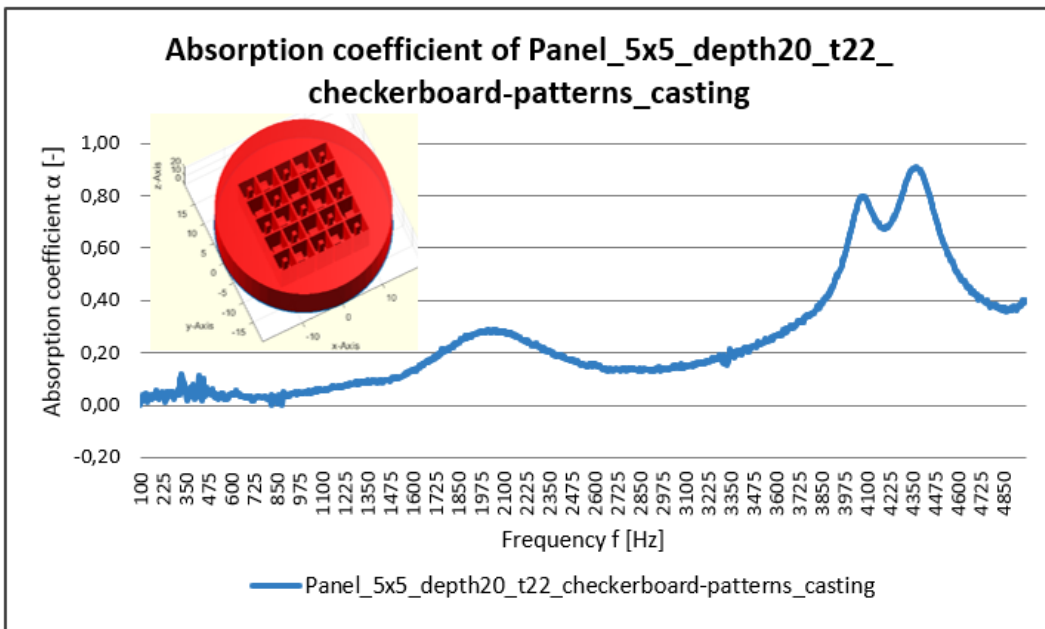


Figure 2.22: Absorption coefficient α of
Panel_5 × 5_depth20_t22_checkerboard – patterns_casting